Prussian blue analogue materials for energy storage applications



Samuel Wheeler

The Queen's College

University of Oxford

A thesis submitted for the degree of

Doctor of Philosophy

Trinity 2020

This thesis is dedicated to
my parents, Hazel and Robert Wheeler,
for their unwavering love and support.

Acknowledgements

I feel very grateful to have the opportunity to pursue a DPhil and would like to acknowledge those who have supported me throughout.

Professor Mauro Pasta, thank you for your mentorship and supervision. You have given me tremendous opportunities to work on interesting scientific problems and instilled great confidence in me.

Dr Matteo Salamone, your help establishing the lab was hugely valuable.

Isaac Capone, Jack Fawdon, Kevin Hurlbutt, Albert Xiao, thank you for being such great colleagues and friends, it has been a pleasure to work alongside you.

I would like to thank my friends and housemates, KC, Vangelis, Sofia, Maarten, Caroline, James, Alex, and Lukas, for making my time is Oxford so enjoyable.

To my parents, Hazel and Robert, you gave me a wonderful childhood and a life full of opportunity.

Finally, to my girlfriend, Anna, thank you for always being there for me and I look forward to our future together.

Abstract

Sodium- and potassium-ion batteries are promising complementary technologies to lithium-ion, providing a low-cost, sustainable alternative that do not contain scarce or expensive elements. Prussian blue analogues (PBAs), an open-framework structure family of materials, are some of the best performing sodium- and potassium-ion cathode materials, exhibiting excellent rate capability and cyclability. The wide composition space and structural complexity of PBAs enables fine control of structure and electrochemical properties. In this thesis, PBA compositions suitable for use as anode materials and solid electrolytes in sodium-ion batteries are investigated.

Manganese hexacyanochromate is first examined as a model composition to study the electrochemical behaviour of transition-metal hexacyanochromates at low potential. Operating in a high-voltage aqueous sodium-ion electrolyte, manganese hexacyanochromate exhibits electrochemical activity at $-0.86\,\mathrm{V}$ vs. SHE, one of the lowest reported reduction potentials. Ex situ analysis demonstrates that charge storage is from reversible sodium insertion and chromium redox. However, the specific capacity offered is too low for practical applications. To improve this the vacancy content of the material must be minimised and both transition metals must be electrochemically active. Low-vacancy chromium(III) hexacyanochromate(III) is identified as a target composition.

Previously, low-vacancy chromium(III) hexacyanochromate(III) has been

of great scientific interest in the field of molecular magnetism due to its high predicted magnetic ordering temperature. However, preparing it has proved to be a challenging synthetic chemistry problem. In this thesis a novel synthesis method for preparing zero-vacancy chromium(III) hexacyanochromate(III) is developed and presented. It entails first synthesising rubidium chromium(II) hexacyanochromate(II) in a nonaqueous solvent, which is subsequently oxidised in water. The electrochemical and magnetic properties of zero-vacancy chromium(III) hexacyanochromate(III) are characterised.

The success of the chromium hexacyanochromate synthetic procedure was on account of understanding and controlling the thermodynamics of the precipitation reaction; a reaction in which a range of possible composition is available due to two competing charge neutrality mechanisms. A holistic model for determining the charge neutrality mechanism employed during PBA synthesis, based on basic thermodynamic and kinetic principles, is detailed. The model successfully rationalises experimental results and provides a basis to develop new synthetic procedures.

Finally, sodium zinc hexacyanoferrate is investigated as a potential solid electrolyte material. The impact of densifying pressure and level of hydration on the crystal structure and ionic conductivity is examined. Additionally, its electronic conductivity and electrochemical stability window, two critical properties, are studied.

Contents

Publication list **v**

1 Introduction **1**

1.1 A brief history of Prussian blue analogues 1

1.2 Bonding and structure of Prussian blue analogues 2

1.2.1 The cyanide ligand 5

1.2.2 Impact of the composition on structure 7

1.3 Electrochemical properties of Prussian blue analogues 9

1.3.1 How a battery works 12

1.3.2 Li-ion versus Na- and K-ion Batteries 16

1.3.3 Prussian blue analogues as electrode materials 16

1.4 Magnetic properties of Prussian blue analogues 22

1.4.1 Types of magnetism 24

1.4.2 Measurement of magnetic properties 25

1.4.3 Interaction between spin centres 28

1.4.4 Mean field and ligand field models 29

1.4.5 Comparison to experimental data 30

1.4.6 Vanadium(II) hexacyanochromate(III) 30

1.4.7 Current state of PBA magnetism research 31

1.5 Synthesis of Prussian blue analogues 32

1.6 Thesis objectives 35

2 Methods **38**

2.1 Synthesis 38

2.2 Physiochemical characterisation 40

2.2.1 Powder X-ray diffraction 40

2.2.1.1 Rievteld refinement 41
2.2.2 Scanning electron microscopy 43
2.2.3 Fourier-transform infrared spectroscopy 44
2.2.4 Simultaneous thermal analysis 47
2.2.5 Inductively coupled plasma - optical emission spectroscopy . . 48
2.2.6 Dynamic light scattering 49
2.3 Electrochemical characterisation 49
2.3.1 Three-electrode flooded cell 50
2.3.2 Solid-state impedance cell 51
2.3.3 Electrode preparation 52
2.3.4 Voltammetry 54
2.3.5 Galvanostatic cycling 55
2.3.6 Electrochemical impedance spectroscopy 56
2.4 Other techniques 61
2.4.1 Superconducting quantum interference device 61

3 Structural and electrochemical properties of manganese hexacyanochromate 63

3.1 Abstract 63
3.2 Introduction 64
3.3 Experimental methods 65
3.4 Results and discussion 68
3.4.1 Physiochemical characterisation of as-synthesised manganese hexacyanochromate 68
3.4.2 Characterisation of water and thermal stability 73
3.4.3 Electrochemical characterisation of manganese hexacyanochromate 76
3.5 Conclusions 82

4 Synthesis of zero-vacancy chromium(III) hexacyanochromate(III) 86

4.1 Abstract . . . 86

4.2 Introduction . . . 87

4.3 Experimental methods . . . 91

4.4 Results and discussion . . . 92

4.4.1 Preparation and characterisation of alkali metal chromium(II) hexacyanochromate(II) compounds . . . 92

4.4.2 Preparation and characterisation of chromium(III) hexacyanochromate(III) . . . 96

4.4.3 Magnetic properties . . . 100

4.4.4 Electrochemical characterisation . . . 102

4.4.5 Thermodynamic considerations . . . 105

4.4.6 Alternative synthesis routes . . . 106

4.5 Conclusions . . . 107

5 Holistic model for determining the charge neutrality mechanism during the synthesis of Prussian blue analogues 109

5.1 Abstract . . . 110

5.2 Introduction . . . 110

5.3 Defining the problem . . . 112

5.3.1 Treatment of water . . . 113

5.4 Kinetic considerations . . . 113

5.4.1 P site lability . . . 114

5.5 Thermodynamic considerations . . . 115

5.5.1 Separation of the reaction . . . 115

5.5.2 Determining desolvation energy . . . 116

5.5.3 Determining lattice enthaply . . . 117

5.6 Application of the model . . . 119

5.6.1 Alkali cation effect in mixed valence materials 119
5.6.2 Alkali cation effect in reduced materials 120
5.6.3 P site transition metal chelating agent 121
5.6.4 Rubidium chromium(II) hexacyanochromate(II) synthesis: effect of solvent and alkali cation 123
5.6.5 Prussian blue charge-transfer type synthesis 125
5.7 Conclusions 125

6 Sodium zinc hexacyanoferrate as a solid electrolyte material 127
6.1 Abstract 127
6.2 Introduction 128
6.3 Experimental methods 131
6.4 Results and discussion 132
6.4.1 Physiochemical characterisation 132
6.4.2 Measurement of ionic conductivity 135
6.4.3 Optimisation of ionic conductivity 139
6.4.3.1 Effect of applied pressure 139
6.4.3.2 Effect of dehydration temperature 140
6.4.3.3 Activation energy 143
6.4.4 Electronic conductivity 145
6.4.5 Electrochemical stability 146
6.5 Conclusions 149

7 Conclusions and future work 151
7.1 Conclusions 151
7.2 Suggested future work 153

References 155

Publication list

1. Wheeler, S.; Hurlbutt, K.; Pasta, M. A New Solid-State Sodium-Metal Battery. *Chem* **2018**, *4* (4), 666-668.
2. Hurlbutt, K.; Wheeler, S.†; Capone, I.; Pasta, M. Prussian Blue Analogs as Battery Materials. *Joule* **2018**, *2* (10), 1950-1960.
3. Wheeler, S.; Capone, I.; Day, S.; Tang, C.; Pasta, M. Low-Potential Prussian Blue Analogues for Sodium-Ion Batteries: Manganese Hexacyanochromate. *Chem. Mater.* **2019**, *31* (7), 2619-2626.
4. Cattermull, J.; Wheeler, S.; Hurlbutt, K.; Pasta, M.; Goodwin, A. Filling Vacancies in a Prussian Blue Analogue Using Mechanochemical Post-Synthetic Modification. *Chem. Commun.* **2020**, *56*, 7873-7876.
5. Fiore, M.; Wheeler, S.†; Hurlbutt, K.; Capone, I.; Fawdon, J.; Ruffo, R.; Pasta, M. Paving the Way toward Highly Efficient, High-Energy Potassium-Ion Batteries with Ionic-Liquid Electrolytes. *Chem. Mater.* **2020**. (Just Accepted) https://doi.org/10.1021/acs.chemmater.0c01347.
6. Dhir, S.; Wheeler, S.†; Capone, I.; Pasta, M. Outlook on K-Ion Batteries. *Chem* **2020**. (Just Accepted) https://doi.org/10.1016/j.chempr.2020.08.012.

†Joint first author

Chapter 1

Introduction

1.1 A brief history of Prussian blue analogues 1

1.2 Bonding and structure of Prussian blue analogues 2

1.2.1 The cyanide ligand 5

1.2.2 Impact of the composition on structure 7

1.3 Electrochemical properties of Prussian blue analogues 9

1.3.1 How a battery works 12

1.3.2 Li-ion versus Na- and K-ion Batteries 16

1.3.3 Prussian blue analogues as electrode materials 16

1.4 Magnetic properties of Prussian blue analogues 22

1.4.1 Types of magnetism 24

1.4.2 Measurement of magnetic properties 25

1.4.3 Interaction between spin centres 28

1.4.4 Mean field and ligand field models 29

1.4.5 Comparison to experimental data 30

1.4.6 Vanadium(II) hexacyanochromate(III) 30

1.4.7 Current state of PBA magnetism research 31

1.5 Synthesis of Prussian blue analogues 32

1.6 Thesis objectives 35

1.1 A brief history of Prussian blue analogues

Prussian blue was first synthesised, serendipitously, at the turn of the 18th century in the laboratory of Dippel.[1] At this time pigments were commonly made from animal

matter and were expensive. In Dippels laboratory another chemist named Johann Jacob Diesbach was attempting to extract a red pigment called Florentine Lake by boiling dried insects with alum ($KAl(SO_4)_2$), iron(III) sulphate ($Fe_2(SO_4)_3$) and potash (K_2CO_3). As he had run out he used some of Dippel's potash. This potash was contaminated with hexacyanoferrate and on mixing with iron sulphate a blue precipitate was formed, Prussian blue.

The synthesis of Prussian blue was first formally reported by John Woodward in 1724.[1] It became the first synthetic pigment, providing a cheap alternative to others at the time. It was in widespread use during the 18th and 19th centuries, featuring in works such as Van Gogh's Starry Night and The Great Wave of Kanagawa by the Japanese artist Hokusai.[2,3]

Investigations into Prussian blue analogues (PBAs) were first documented by Brown.[4] PBAs were produced by replacing the iron salt with a salt of a different transition metal. Ever since, chemists have developed new and improved synthesis methods and set about defining the composition, stoichiometry, and structure of Prussian blue and its analogues.

1.2 Bonding and structure of Prussian blue analogues

Keggin and Miles first proposed a structure for Prussian blue in the 1930s based on X-ray diffraction data.[5] This structure consisted of a face-centered cubic (*fcc*) arrangement of transition metals bridged by cyanide ligands. In this model structure extra transition metals were placed on interstitial sites to provide charge neutrality. It took until the 1970s before the revised and broadly accepted model was reported by Ludi *et al.* based on X-ray diffraction data of single crystal particles of Prussian blue.[6] Shortly after Bernal *et al.* reported the same model of the structure of PBAs

based on X-ray and neutron diffraction data of manganese hexacyanocobaltate and cadmium hexacyanocobaltate.[7] In this revised model the structure contains hexacyanometallate vacancies which provide charge neutrality, instead of transition metals on interstitial sites. Neutron diffraction experiments identified water in multiple bonding environments; coordinated to exposed transition metals in hexacyanoferrate vacancies, hydrogen bonded to coordinated water molecules, uncoordinated in interstitial sites and at the centre of hexacyanometallate vacancies.[7,8] Due to the random distribution of hexacyanometallate vacancies the space group for PBAs is typically *Fm3m*, rather than the more primitive *Pm3m*. By this point there was significant structural characterisation work on analogues of Prussian blue in which one or both of the iron species were replaced by Cr, Mn, or Co.[9,10]

It is now recognised that Prussian blue, iron(III) hexacyanoferrate(II) synthesised from Fe^{3+} and $[Fe(CN)_6]^{4-}$, is identical to the material known as Turnbulls blue, synthesised from Fe^{2+} and $[Fe(CN)_6]^{3-}$, which had been an open question.[11,12] The sensitivity of Prussian blue to synthesis conditions gives insight into the complexity of Prussian blue analogues as a whole. Different compositions are synthesised depending if potassium is present; so called 'soluble' Prussian blue which has the formula $KFe[Fe(CN)_6]$ if it is and 'insoluble' Prussian blue which has the formula $Fe[Fe(CN)_6]_{0.75}$ if it isn't.

The definitive model structure for Prussian blue analogues is shown in Figure 1.1, and the general formula is given by $A_xP^j[R^k(CN)_6]_{1-y} \cdot wH_2O$. Where A are alkali cations, P and R are transition metals with octahedral carbon and nitrogen bonding environments respectively, y is the hexacyanometallate vacancy content, and w is the water content. j and k are the oxidation state of the P and R transition metals respectively. The transition metals are in an FCC arrangement bridged by the cyanide ligands forming a cubic structure. Within the 'subcubes' are interstitial sites that are interconnected in three dimensions by ion conduction pathways. Hexacyanometallate

vacancies can be present on up to 1/3, or more, of sites. There are two types of water in the structure; 'coordinated' water bonded to the P site within vacancies, and 'zeolitic' water in interstitial sites. Wyckoff positions for sites P, R, A, C, and N are 4a, 4b, 8c, 24e, and 24e, respectively.

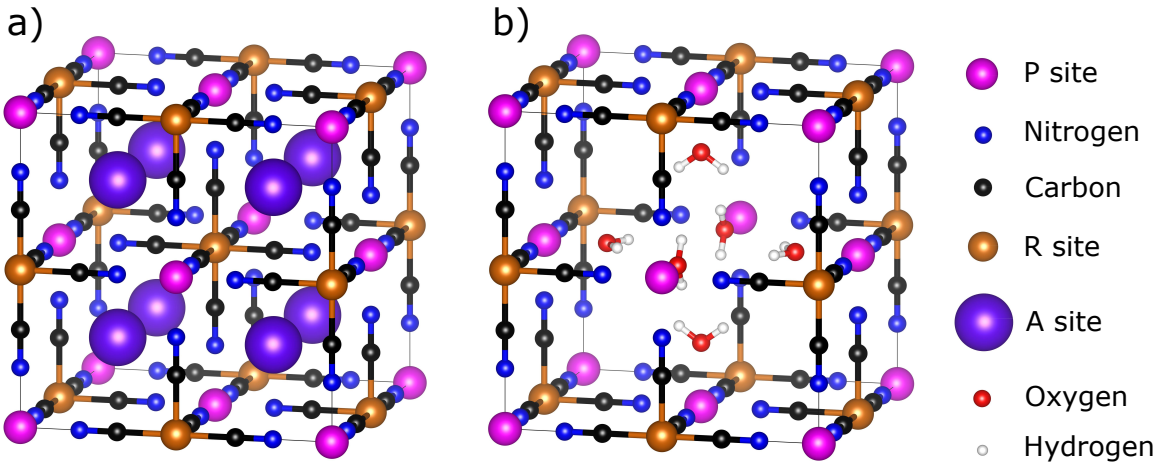


Figure 1.1: A schematic of the Prussian blue analogue crystal structure. a) The crystal structure with zero vacancies and all the interstitial sites occupied. b) The crystal structure containing a hexacyanometallate vacancy and coordinated water molecules bonded to P site transition metals. Other noncoordinated forms of water are omitted for clarity.

Charge neutrality in the system defines a relationship between the transition metal oxidation states, vacancy content, and alkali cation content. Both vacancies and inserting alkali cations are positive defects, therefore, for a given oxidation state they compete to provide charge neutrality.

A large number of species can substitute into the PBA structure on the A, P and R sites. A site species include alkali metals from Li^+ to Cs^+,[13–18] divalent cations such as Mg^{2+},[19] and molecular cations such as NH_4^+.[20,21] The large size of the interstitial sites within the PBA open framework structure enable the structure to accommodate such large species. Most of the 3d transition metals can accommodate the P site and 3d metals with up to six 3d electrons can accommodate the R site. The P and R site transition metals can take multiple oxidation states, increasing the complexity of the

materials system.

1.2.1 The cyanide ligand

Understanding the chemistry of the cyanide ligand is essential to understand the bonding and structure of PBAs. Cyanide is an ambidentate ligand with a negative charge that can act as both a σ donor and π acceptor.[22–25] It is isoelectric to CO and NO^+. Cyanide acting as a monodentate ligand appears to always have carbon as the donor atom.[22] This is because the highest energy lone pair is mostly localised on the carbon and the electronegativity of carbon is lower than that of nitrogen. Due to its anionic nature cyanide is a stronger σ donor than CO and can form strong M-CN σ bonds. Because of this cyanide can stabilise metals in high oxidation states, such as $Mn^{IV}(CN)_6^{2-}$ and $Pt^{IV}(CN)_6^{2-}$.

First row transition metals form octahedral complexes with cyanide ligands. The effect octahedral coordination has on the energy levels of d orbitals are shown in Figure 1.2. d_{xy}, d_{xz} and d_{yz} orbitals reduce in energy whilst $d_{x^2-y^2}$ and d_{z^2} orbitals increase in energy. The crystal field splitting energy, Δ_0, depends on the nature of the ligand but is high for the cyanide ligand.

Evidence of π backbonding comes from the series of $M^{III}(CN)_6^{3-}$ (M from Cr to Co) in which the M-C bond length decreases from 2.08 Å to 1.89 Å.[23] In octahedral complexes the d_{xy}, d_{xz} and d_{yz} orbitals are orientated to overlap with π antibonding orbitals of the ligand. π back-bonding avoids accumulation of significant negative charge on the metal atom, increasing the strength of the metal-carbon bond and weakening of the carbon-nitrogen bond. This effect is the basis of the interaction between the metal atom and the frequency of the cyanide stretch, often used to indirectly used to study the nature of the metal species.[23,25] Cyanide acting as a π acceptor reportedly enables it to stabilise metal atoms in low oxidation states such as $Mn^{I}(CN)_6^{5-}$ and $Cr^{0}(CN)_6^{6-}$, although characterisation of low oxidation state

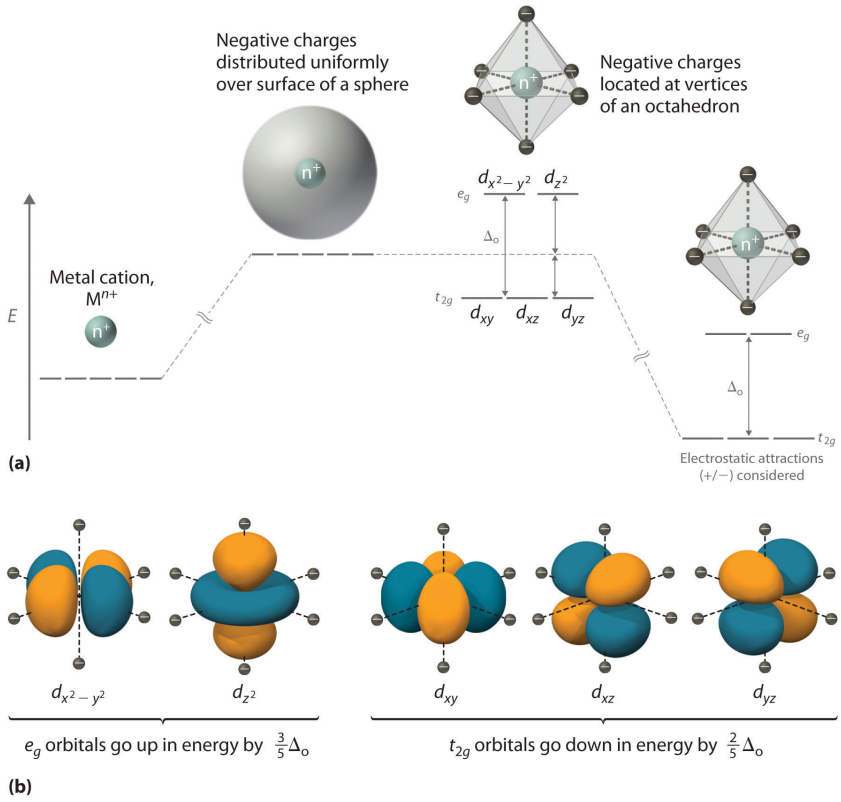


Figure 1.2: Bonding in octahedral transition metal complexes. a) The energy and b) shape of the d orbitals. Reproduced from ref[26].

transition metal cyanide complexes is limited.[24]

Cyanide bonded through the carbon is at the strong-field end of the spectrochemical series, has a large crystal field splitting energy, Δ_0, and exclusively produces low-spin complexes. Octahedral cyanide complexes of transition metals with more than six 3d electrons are unstable. The electronic configuration of first row transition metals are shown in Figure 1.3.

In PBAs cyanides acts as a linear bridging ligand between the P and R site transition metals. The nature of the bonding between the nitrogen end of the cyanide ligand, as compared to the carbon end, and the transition metals are significantly different. This means in the PBA structure P-site transition metals are in significantly different bonding environments compared to the R-site transition metals. There is limited donation of charge from the cyanide ligand to the P-site transition metal and

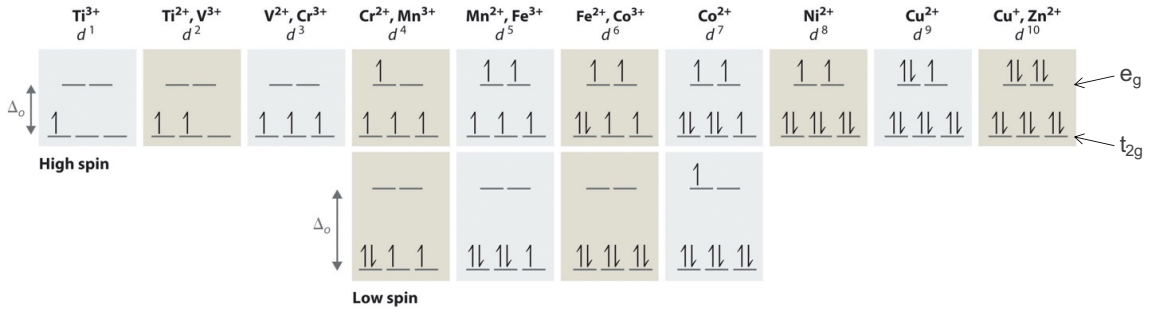


Figure 1.3: The electronic configuration of first row transition metals in high and low spin states. Adapted from ref[26].

the bond is primarily ionic in nature.[22,23,27] The P site transition metal can exhibit weak influence over the bonding within the complex by its polarising power, its ionic potential. The higher the ionic potential of the P-site transition metal, the weaker the σ bond between the R-site transition metal and the bridging cyanide ligands which is accompanied by an increase in π backbonding.[28,29] The cyanide ion bonded through the nitrogen end acts as a weak-field ligand, has a small crystal field splitting energy and, therefore, P-site transition metals are typically in a high-spin state.

Bonding within the $R(CN)_6$ complex is strong and is why the complex is often chemically highly stable and acts as a single chemical unit. PBAs are typically synthesised from the complex and vacancies are present on the entire complex site.

1.2.2 Impact of the composition on structure

The composition of a PBA governs its structure and properties; for the alkali cations their ionic radius, for the transition metals their radius, charge, and electronic structure are all important.

Small alkali cations, such as Na^+, are unstable in the centre of the interstitial site, 8c position, and at sufficiently high contents move in a coordinated manner from the centre of the intersitial site along the [1 1 1] towards the corner inducing a cubic to rhombohedral phase transition.[30,31] The angles deviate from 90° by approximately 3°.

Ordering of alkali cation species can also induce changes in symmetry.

The most significant distortion due the electronic structure of the transition metals is a cooperative strong Jahn-Teller distortion. If one of the transition metals has unequally occupied e_g orbitals, as in the cases of Mn^{3+} and Cu^{2+}, they undergo a strong Jahn-Teller distortion, see Figure 1.3.[16,32,33] Most often this manifests as an extension of the axial bonds and a contraction of the equatorial bonds around the transition metal, although the reverse is also possible. This distortion breaks the symmetry around the transition metal, decreasing the energy of the occupied e_g orbital, which decreases the energy of the species as a whole. Interestingly, if the vacancy content is low there is long range ordering of the Jahn-Teller distorted species and distortion of the crystal structure from cubic to tetragonal, as seen in $K_2Mn[Fe(CN)_6]$ and $Cu[Pt(CN)_6]$.[33] However, if the vacancy content is high the local structural distortion can be accommodated by the vacancies and the crystal structure remains cubic, as seen in $Cu[Co(CN)_6]_{2/3}$ or $Mn[Fe(CN)_6]_{0.83}$.[32,33] A transition metal with unqeually occupied t_{2g} orbitals which undergoes a weak Jahn-Teller distortion typically does not lead to a noticeable distortion away from cubic symmetry.

Clearly, the metal species present in the PBA structure impact much more than the structure itself. The combination of wide composition space (number and combinations of metal species in the structure) and structural complexity (two metals in different bonding and ligand field environments, presence of hexacyanometallate vacancies, and interstitial sites hosting monovalent cations, divalent cations, molecular ions such as ammonium, neutral molecules such as water or gas molecules such as H_2) leads to an intriguing diversity of properties.

Magnetic, electronic and optical properties are determined by the electronic configuration of, and interaction between, the transition metal species. The large interconnected interstitial sites enables gas storage and storing ions for batteries or Cs^+ sequestration.[13,34,35] Transverse vibrational mode of the cyanide ligands allow for zero

and negative thermal expansions.[36,37] Of particular interest is how multiple inputs can change various properties, for example electrochemical reduction/oxidation can change the materials magnetic moment or colour.[38] Possible input stimuli include temperature, humidity,[39] light irradiance,[40] mechanical stress, gas environment,[41] and oxidation state.

Of interest for the work in this thesis are the electrochemical properties and magnetic properties of PBAs. They will be described below in more detail.

1.3 Electrochemical properties of Prussian blue analogues

Research into the electrochemical behaviour of Prussian blue and its analogues began with seminal work from Neff *et al.* in the late 1970s and throughout the 1980s.[42–46] They showed that electrodeposited Prussian blue films could be electrochemically reduced and oxidised, transitioning from Prussian blue to Everitts salt (Prussian white) and Berlin green, respectively.[43] Potassium insertion/extraction provided charge neutrality. There was a concurrent change in colour with electrochemical reduction/oxidation and the immediate application found was in electrochromic devices. The electrochemical reaction was also extremely fast with colour changes from transparent to blue in less than 100 ms.[45]

Subsequent work identified that the electrolyte pH significantly affected the long term cycling stability of the Prussian blue films, due to pH dependent solubility of Prussian blue.[47] It was found that in an optimised electrolyte (pH of 2 - 3 from strong acid alone) the films were stable for lifetimes in excess of 100,000 cycles, Figure 1.4. The observed changes in the voltammogram with cycling is likely due to cracks forming in the electrode film which decreases the average solid state diffusion length and, therefore, increases the maximum current.

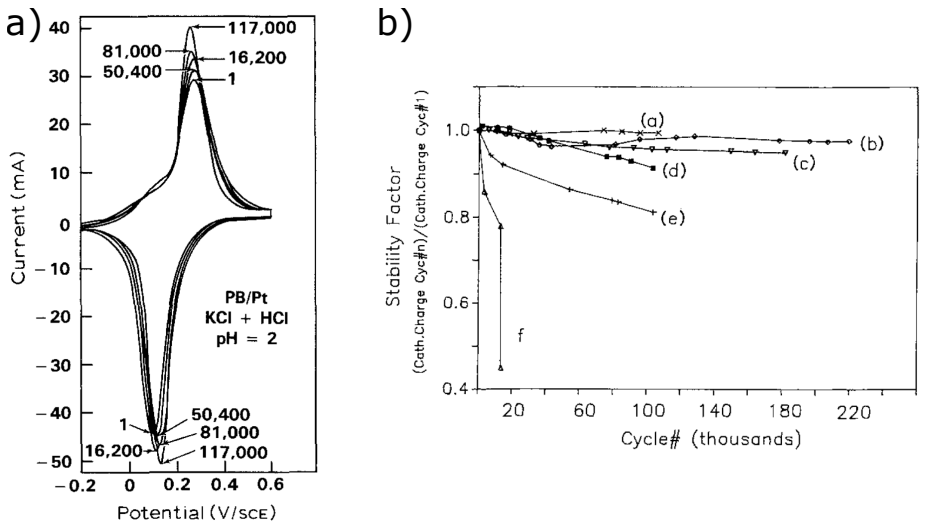


Figure 1.4: Electrochemical properties of electrodeposited Prussian blue, $Fe_4[Fe(CN)_6]_3$, films. a) Cyclic voltammograms after a given number of cycles at 1 Hz. b) The cycling stability in a range of electrolytes, the greatest stability was in a 0.9 M KCl, 0.02 M HCl solution. Reprinted from ref[47] with permission from Springer Nature.

In 1995, Scholz and Dostal comprehensively reported the electrochemical activity and reduction potentials for a wide range of Prussian blue analogues including electrochemically active R-site transition metals Fe, Mn, and Cr, formed into PBAs with a range of inactive P-site cations including Fe, Mn, Cr, Co, Ni, Cu, Ag, Al, In, Pb.[28] Potassium was primarily used as the insertion ion. In these materials only the R-site species were electrochemically active, however, the reduction potentials of the materials were found to be dependent on the R-site species, the P-site species and the alkali cation (A) species. Figure 1.5 shows the change in reduction potential and lattice parameter with composition.

The reduction potential of the PBA materials were found to be most correlated with the reduction potential of the parent aqueous complex, $R(CN)_{6\,(aq)}^{n/n-1}$. The reduction potential of the aqueous complex of $Fe(CN)_6^{3-/4-}$ is 0.35 V, $Mn(CN)_6^{3-/4-}$ is −0.24 V, $Mn(CN)_6^{4-/5-}$ is −1.050 V and $Cr(CN)_6^{3-/4-}$ is −1.140 V, all versus SHE. Note that the reduction potential of the complex is not necessarily related to the reduction potential of the R site species due to changes in the electronic configuration induced by the

strong field cyanide ligands. For example, the reduction potential of $Co^{III/II}$ is 1.82 V vs. standard hydrogen electrode (SHE) whereas $Co(CN)_6^{3-}$ is stable against reduction to −0.83 V vs. SHE at which a single cyanide ligand leaves the complex, forming pentacyanocobaltate(III).[48] PBAs have reduction potentials between 300 and 800 mV higher than their corresponding parent complex. For example, $Ni^{II}[Fe^{III/II}(CN)_6]$ has a reduction potential of 0.857 V vs. SHE, 502 mV higher than the reduction potential of $Fe(CN)_6^{3-/4-}$. Scholz and Dostal postulated that the ionic potential of the P site species impacts the reduction potential of the hexacyanometallate complex when in the PBA structure, $P^j[R^{III/II}(CN)_6]$ (Figure 1.6). The larger the ionic potential (charge/radius) the larger the polarising effect, the weaker the σ bond between the R and C atom, which is accompanied by and increase in π backbonding. This decreases the absolute energy of the t_{2g} orbitals, thus affecting the reduction potential of the material. They managed to plot the ionic potential of the P site in transition metal hexacyanoferrates against reduction potential and get a reasonable fit, even including the proton which represents the bonding environment of the complex as an ion in aqueous solution.[28]

They also highlighted how the A-site species influences the reduction potential for a number of PBA compositions, primarily due to the free energy of hydration of the alkali cations.[28] More recent works have also demonstrated this relationship.[17,49] Na^+, K^+ and Rb^+ as the insertion ion follow the expected trend that the larger the cation, the lower the free energy of hydration and the higher the reduction potential. Li^+, on the other hand, does not follow this trend for certain compositions which can be attributed to the cation being partially hydrated within the structure and occupying off-centre positions, something also subsequently determined for Na^+ too although to a lesser extent. The electrochemical system with Cs^+ as the insertion ion does not follow this general trend which is likely because its large size prevents facile migration through the PBA structure. The trend between hydration energy and

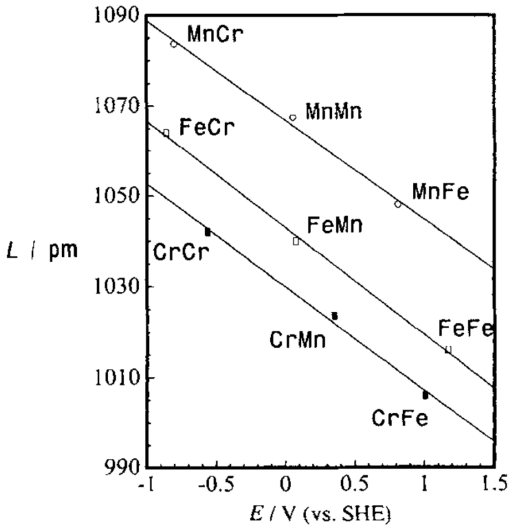


Figure 1.5: The reduction potential, E, and lattice parameter, L, for a number of PBA compositions. Experiments were conducted in an aqueous potassium ion electrolyte, no further details on the electrolyte composition or pH were given. Notation is PR, for example MnCr is manganese hexacyanochromate. Reprinted with permission from ref[28]. Copyright © 1995 by VCH Verlagsgesellschaft mbH, Germany.

reduction potential is also observed for divalent and trivalent insertion ions.[50]

1.3.1 How a battery works

A brief description of how a battery functions is required to understand what is required of battery materials. Batteries have three major components; the positive electrode (cathode), the negative electrode (anode) and the electrolyte.[51] The electrolyte provides an ionically conducting but electronically insulating connection between the electrodes, and is a salt of the alkali cation in a solvent. The battery is charged by simultaneously oxidising the cathode and reducing the anode, with charge neutrality provided by migration of alkali cations from the cathode to the anode and an electric current passing through the external circuit. On discharge this process is reversed. Conventional lithium-ion batteries have lithium as the alkali cation, a layered metal oxide (LMO) cathode, and a graphite anode which store lithium ions through an intercalation mechanism, Figure 1.7. Intercalation is the reversible insertion of a molecule or ion

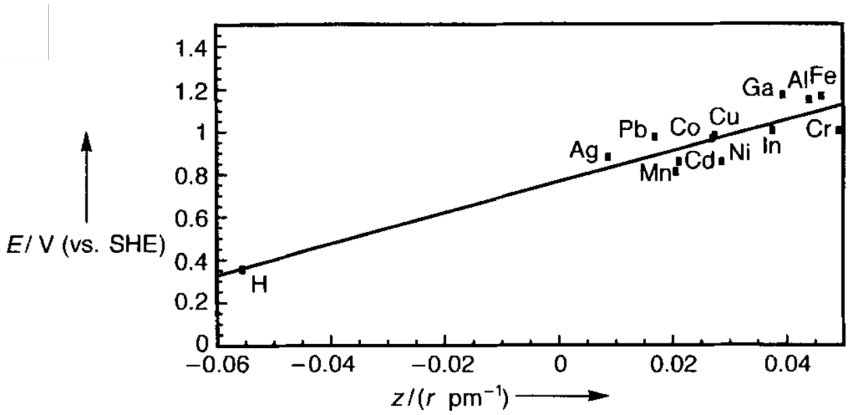


Figure 1.6: The reduction potential, E, of transition metal hexacyanoferrates plotted against the ionic potential of the P site transition metal, or proton which approximates the bonding environment of the complex in water. Experiments were conducted in an aqueous potassium ion electrolyte, no further details on the electrolyte composition or pH were given. Reprinted with permission from ref[28]. Copyright © 1995 by VCH Verlagsgesellschaft mbH, Germany.

into a layered structure. In the case of lithium intercalation into graphite, lithium remains a charged ion and is inserted between the sheets of carbon atoms. During this process the van der Waals gap between carbon sheets increase. Layered metal oxide materials also store lithium ions through an intercalation mechanism. Other active materials, such as lithium ion phosphate, store lithium ions through a topotactic insertion reaction.

The voltage, E, of a battery is related to the Gibbs energy, ΔG, of reaction by the following equation.

$$E = -\frac{\Delta G}{zF} \tag{1.1}$$

Where z if the number of electrons transferred in the reaction an F is the Faraday constant. A more convenient method is to define the voltage of the anode and cathode against a suitable reference, such as the standard hydrogen electrode (SHE) or Li^+/Li, and then define the cell voltage, E_{cell}, as the difference between the anode and cathode voltages.

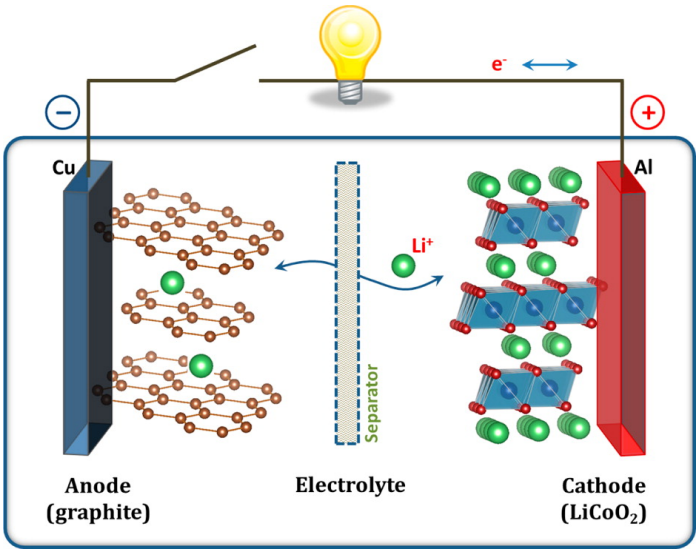


Figure 1.7: A schematic of a conventional lithium-ion battery. Reprinted (adapted) with permission from ref[52]. Copyright © 2013 American Chemical Society.

$$E_{cell} = E_{cathode} - E_{anode} \tag{1.2}$$

This method allows easier comparison between electrode materials and inputs from each electrode. The energy and power density (energy stored per unit mass and volume) of the battery is improved by increasing the $E_{cathode}$ and decreasing the E_{anode}. For the case of a conventional lithium ion battery the graphite anode has a reduction potential of 0.1 V vs. Li^+/Li and a lithium cobalt oxide cathode has a reduction potential of around 4.0 V vs. Li^+/Li.

The specific energy of a battery is given by the product of the cell voltage and specific capacity (charge stored per unit mass). Another relevant metric is the volumetric specific capacity which is the charge stored per unit volume. In basic research the specific capacity of only the active materials are considered, and the mass and volume from other components are ignored. To optimise energy density we therefore want to increase the cell voltage, as seen previously, and increase the specific capacities of the electrode materials.

Reduction potential and specific capacity are therefore important metrics for

analysing battery active materials. When determining the battery performance on the stack level, inactive components such as electrolyte, binder and current collector also have to be considered. Programs such as BATPAC have been developed to help calculate stack level performance in a comprehensive, reliable, and repeatable manner.[53]

Cost is also an important consideration when designing and developing battery materials. The cost of conventional lithium-ion batteries have undergone a remarkable decrease in cost over the past decade driven primarily by optimisation of manufacturing procedures, economies of scale, and only in part by improvement in battery chemistry. Current cost estimates have raw materials at approximately 50% and the other 50% from processing and manufacturing. Without a step change in the battery chemistry it is unlikely the cost savings will continue into the future.

Other important battery performance metrics are power (rate) capability, cycle life, energy efficiency, and calendar life among others. The vast number of performance metrics, of which cannot all be optimised simultaneously, result in batteries being designed for specific applications. For example, in cell phones graphite|lithium cobalt oxide (LCO) is commonly used as it has very high energy density and the high cost is not as important. Alternatively, for electric buses lithium iron phosphate (LFP)|lithium titanite (LTO) is used as it can charge very quickly, has a very long cycle life, and the relatively low energy density is not as important. An emerging application is stationary grid energy storage which is essential for integrating intermittent and unreliable renewable energy sources into the electric grid. Batteries for this application need to be very low cost and have long lifetimes, whilst high energy density is only secondary concern.

1.3.2 Li-ion versus Na- and K-ion Batteries

Lithium-ion batteries have enabled the portable electronic revolution and power the electronic devices we all use today. However, as mentioned previously, the decrease in cost of lithium-ion batteries are expected to plateau. In addition, lithium-ion batteries use lithium and often cobalt which are of relatively low abundance and geographically restricted leading to high raw material costs. The demand for batteries is exponentially increasing driven by use in electric vehicles and in grid-scale energy storage which is increasing the pressure on the already limited supply of raw materials.[54,55]

Sodium- and potassium-ion batteries are seen as complementary technologies to lithium-ion batteries.[56–59] They operate in an analogous matter, can utilise existing lithium-ion manufacturing infrastructure, and are based on earth-abundant less expensive elements such as Fe, Mn, O, Na, and K. The primary cost savings arise from the use of sodium or potassium instead lithium, the use of an aluminium anode current collector instead of copper (Li alloys with Al and so cannot be used), and cobalt-free cathodes. However, due to the higher ionic radius of sodium and potassium compared to lithium, 1.02 Å and 1.38 Å versus 0.76 Å, analogous lithium-ion electrode materials are not suitable.

This motivates a search for electrode materials for sodium- and potassium-ion batteries that function as well or better than current lithium-ion electrode materials.

1.3.3 Prussian blue analogues as electrode materials

Prussian blue analogues exhibit properties that make them attractive battery materials; reversible alkali cation insertion and transition metal redox within their highly stable framework structure, fast ion-insertion kinetics, a wide composition space that enables tuning of the reduction potential, and the ability to insert a range of alkali cations including sodium and potassium. Additionally, PBAs are made through a low-

temperature scalable aqueous processing route and can be made from earth-abundant inexpensive transition metals.

There were early reports of potassium-ion batteries based on PBAs in the early 2000s.[60] However, recent research into PBAs as electrode materials started in 2011 from the group of Cui,[61,62] and then in 2012 from the group of Goodenough,[15] supported by previous fundamental work on reversible ion insertion into PBA materials by the group of Moritomo.[63–70] Almost all previous work has been on transition metal hexacyanoferrate compounds that have high reduction potentials, suitable as cathode materials, and use sodium or potassium as the insertion ion. The group of Cui has primarily studied PBAs in aqueous electrolytes whereas Goodenough has studied them in non-aqueous electrolytes.

The first compositions studied by Wessells *et al.* in detail were copper hexacyanoferrate and nickel hexacyanoferrate, in which iron is electrochemically active.[61,62] A commonly used notation for PBAs is PHCR, and will be used throughout this thesis. For example, CrHCFe and NiHCFe for copper hexacyanoferrate and nickel hexacyanoferrate, respectively. They both had high vacancy contents and were operated in an aqueous electrolyte. They exhibited exceptional cycle life and rate capability; copper hexacyanoferrate maintained 83% of initial capacity after 40,000 cycles and maintained two-thirds of its capacity at 80C, Figure 1.8. Both materials had a single sloping voltage plateau indicating a single-phase solid solution reaction. They did, however, have relatively low specific capacities of approximately 60 mAh/g which was due to their high vacancy contents and that only iron was electrochemically active.

An important principle in designing PBAs as battery materials is the relationship between vacancy content and specific capacity. Since vacancies are positive defects they reduce the number of charge balancing alkali cations in the structure. For example, high-vacancy copper hexacyanoferrate only stores 2/3 sodium ions per formula unit when fully discharged, $Na_{2/3}Cu^{II}[Fe^{II}(CN)_6]_{2/3}$, corresponding to a specific capacity

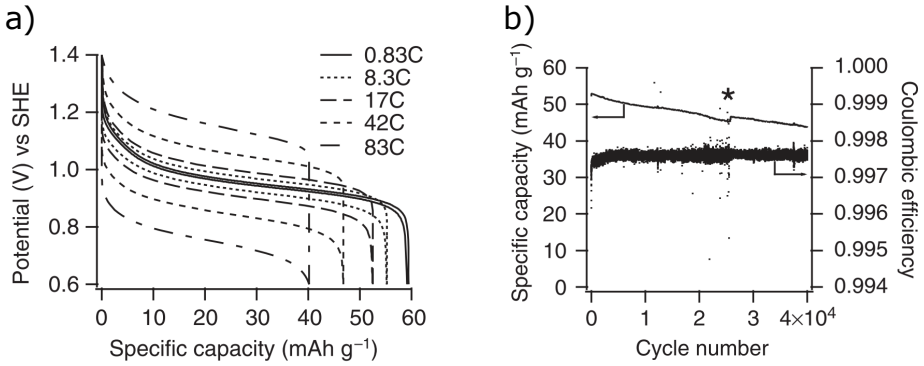


Figure 1.8: The electrochemical performance of copper hexacyanoferrate. a) A voltage plateau at ≈1 V vs. SHE, offering a specific capacity of 60 mAh/g and excellent rate capability. b) Cycling data up to 40,000 cycles. Reprinted from ref[61] with permission from Springer Nature.

of around 65 mAh/g. A hypothetical vacancy-free iron hexacyanoferrate can store 2 sodium ions per formula unit, $Na_2Fe^{II}[Fe^{II}(CN)_6]_1$, corresponding to a specific capacity of around 170 mAh/g. It is clear that a two-electron redox reaction is required to reversibly insert 2 sodium ions per formula unit to achieve this high capacity. This is typically, but not exclusively, from each transition metal exhibiting a single electron redox reaction. The electrochemical reactions of these two materials are shown below to demonstrate the charge storage mechanism.

$$Cu^{II}[Fe^{III}(CN)_6]_{2/3} + \frac{2}{3}Na^+ + \frac{2}{3}e^- \rightleftharpoons Na_{2/3}Cu^{II}[Fe^{II}(CN)_6]_{2/3} \tag{1.3}$$

$$Fe^{III}[Fe^{III}(CN)_6]_1 + 2\,Na^+ + 2\,e^- \rightleftharpoons Na_2Fe^{II}[Fe^{II}(CN)_6]_1 \tag{1.4}$$

Meanwhile, Gooednough *et al.* reported a number of transition metal hexacyanoferrates (P = Mn, Fe, Co, Ni, Cu, Zn) cycled in an organic electrolyte.[15] These systems performed poorly with very low coulombic efficiencies which was determined to be from parasitic reactions from water in the structure. Iron hexacyanoferrate did, however, display a specific capacity of around 100 mAh/g over two voltage plateaus indicating that both iron sites were electrochemically active.

Following this work there have broadly been two streams of research, although there is some overlap. Firstly, developing PBAs that have lower reduction potentials that can operate as an anode in conjunction with a PBA cathode in an aqueous full cell. PBA cathodes must be coupled to an anode material which limits the full cell performance. If a PBA with a low reduction potential can be developed that has comparable electrochemical properties, a high-performing PBA-PBA full cell can be produced. The second stream of research is improving the electrochemical performance of PBA cathodes in non-aqueous electrolytes. Specifically, increasing the attainable specific capacity of PBA cathodes materials, and improving their coulombic efficiency and cyclability.

Here I will describe the literature with respect to these two research streams since 2012, and then how the work in this thesis is related.

First, the PBA-PBA full cell stream. Copper hexacyanoferrate was used as the cathode in an aqueous full cell with a hybrid activated carbon/polypyrrole (AC/PPy) capacitive anode.[71] This full cell had a voltage of around 1 V and exhibited very stable cycling. In the search for low reduction potential PBA materials, informed by the work of Dostal and Scholz, Pasta *et al.* studied manganese hexacyanomanganate and chromium hexacyanomanganate.[72] The redox couple $Mn^{II}[Mn^{III/II}(CN)_6]$ had a reduction potential of around 0 V vs. SHE, within the limited electrochemical stability of conventional aqueous electrolytes. This CuHCFe|MnHCMn full cell, see Figure 1.9, had a potential of approximately 1 V, very good rate capability (80% capacity retention at 50C), and no measurable capacity loss after 1000 cycles.

Following this work a vacancy-free synthesis of manganese hexacyanomanganate was developed and a more thorough characterisation reported.[17] This article reported that sodium manganese hexacyanomanganate had three redox couples and could accommodate three sodium ions per formula unit, instead of just two. This increased the specific capacity to 210 mAh/g. The lower reduction potential redox couple

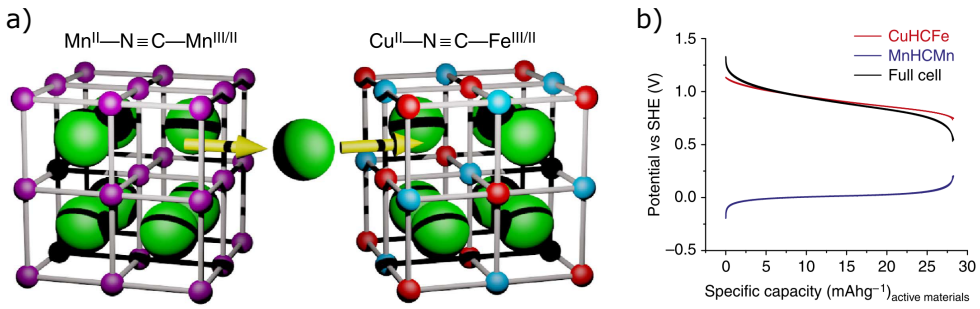


Figure 1.9: a) A schematic of the PBA-PBA full cell and b) the voltage profiles of the cathode, anode, and full cell. The insertion ion (green sphere) in this system is sodium. Reprinted from ref[72] with permission from Springer Nature.

$Mn^{II}[Mn^{II/I}(CN)_6]$, −0.7 V vs. SHE, was then used as an anode in conjunction with copper hexacyanoferrate cathode in a full cell with an average discharge voltage of 1.55 V.[73] Due to the anode operating outside the conventional electrochemical stability window of water a novel co-solvent (10:90 water:acetonitrile) electrolyte was used. The thermodynamic electrochemical stability window of water is 1.23 V, although the experimentally measured values are higher due to the addition of overpotentials necessary to drive the electrochemical reactions. The novel co-solvent electrolyte increased the electrochemical stability window to at least 1.74 V and also significantly reduces PBA material dissolution. This full cell exhibited excellent cycling stability, maintaining around 95% capacity after 1000 cycles and a coulombic efficiency of more than 99.5%. This is the current state of the art in PBA-PBA full cell research and is being commercialised by Natron Energy, Inc.

Meanwhile, there have been advancements in PBA cathodes, specifically in the synthesis and doping of manganese hexacyanoferrate,[74–77] and 'water-in-salt' electrolytes have emerged.[78–81] A doped manganese hexacyanoferrate cathode with a high specific capacity of 135 mAh/g and good cycling stability in a highly concentrated potassium triflate electrolyte was reported.[75] It is clear that PBA cathodes perform well and it is the anodes that are limiting performance. The drive for lower reduction potential anode materials, to increase full cell voltage and therefore energy density, led to the

development and study of $Mn^{II}[Mn^{II/I}(CN)_6]$. However, this material has a specific capacity of only 65 mAh/g. Improvements in both further lowering the reduction potential and increasing the specific capacity require both transition metals to be electrochemically active at low potentials, and the material to have a low vacancy content. A clear candidate material is chromium(III) hexacyanomanganate(II) (or chromium(II) hexacyanomanganate(III) as the oxidation state is uncertain), as both the $Cr^{3+/2+}$ and $Mn(CN)_6^{4-/5-}$ have low reduction potentials. Synthesis of this material was attempted but resulted in very poor crystallinity and low specific capacity of 30 mAh/g.[72] This was down to the tendency of Cr^{2+} to hydrolyse during synthesis. The next logical family of materials to study are the transition metal hexacyanochromates, which forms the basis of this thesis.

The second stream of research will now be described briefly. Transition metal hexacyanoferrates with iron,[82] manganese[83] and cobalt[69] in the P site were identified as three compositions for which both transition metals are electrochemically active in the potential range suitable for cathode materials, enabling two-electron redox reactions and utilisation of all interstitial sites, increasing the theoretical specific capacities to around 170 mAh/g.[84,85] The major research problem has been synthesising these materials with minimal, or zero, vacancies. This is essential because the lower the vacancy content the higher the specific capacity, and water strongly bound in vacancies leads to parasitic reactions when operated in a non-aqueous electrolyte. For Prussian white a single-iron-source synthesis was developed leading to a specific capacity of 170 mAh/g.[82,86] For manganese and cobalt hexacyanoferrate a citrate-assisted synthesis method has been developed which produces materials with lower vacancy contents and larger particle sizes.[87,88] These high capacity cathode materials operated in non-aqueous electrolytes have poorer rate capability, compared to when operated in aqueous electrolytes, and crucially have worse cyclability which has been associated to the electrochemical activity of the P site species.[85,86,89] Manganese hexacyanoferrate,

having a high operating voltage and containing only inexpensive elements (no cobalt), is the most attractive cathode material. However, during electrochemical cycling it undergoes a phase transition from cubic to tetragonal, due to the Jahn-Teller distortion from the $Mn^{III}N_6$ octahedra, and disproportionation from Mn^{3+} leads to dissolution of the material.[75,90] Mitigating these capacity loss mechanisms is currently the most pressing issue.

1.4 Magnetic properties of Prussian blue analogues

PBAs are categorised as molecular-based magnets and have been of interest to the field of molecular magnetism since the early 1990s. Although the focus of my thesis is on the electrochemical properties of PBAs, to understand the significance of the work in this thesis to the field of molecular magnetism a summary of PBA magnetism theory and literature is necessary. The description below is by no means comprehensive and references are provided.

Molecule-based magnets are a class of extended solids that are comprised of molecular 'bricks' that exhibit common bulk magnetic behaviour such as ferromagnetism.[91] This is distinct from single-molecule magnetism in which the magnetic properties of isolated molecules are of interest. Molecule-based magnets are of interest because they are low density, chemically tuneable, produced using low-temperature solution-based methods, and have the ability to interact with external stimulus to alter their magnetic properties.

Fundamental work on molecular magnetism was carried out by Kahn and others. In 1991, vanadium(II) tetracyanoethylene ($V[TCNE]_x$), the first room temperature molecular-based magnet, was published.[92] During the rest of the 90s there was considerable work on the magnetic properties of Prussian blue analogues from Verdaguer[93–97], Girolami[98–100], Hashimoto[38,40,101] and others, developing theory alongside experimen-

tal work. Comprehensive summaries of this works are provided[102–105], a particularly useful reference is a book chapter written by Verdaguer and Girolami.[106]

Prussian blue analogues (PBAs) are one of the most versatile and interesting molecule-based magnetic systems to study. Their cubic structure, two spin environments, transition metal octahedral coordination and composition tunability make them a 'textbook' system. Transition metal magnetic centres interact through the cyanide bridge producing long-range magnetic order. There is considerable control over their bulk magnetic properties by tuning the local magnetic interactions. Control is achieved by substituting the transition metal species, changing their oxidation state, and modifying the vacancy content among other parameters, much like their electrochemical properties. Although the metal centres are approximately 5 Å apart they have strong magnetic exchange coupling through the cyanide bridge, as demonstrated by room temperature magnetisation of vanadium(II) hexacyanochromate(III).[95,100]

In addition to the ability to tune the magnetic properties of as-synthesised PBA materials, one of the most fascinating prospects is reversibly changing the magnetic properties of PBAs by external stimuli[107]. Electrochemical switching of the magnetic properties of chromium hexacyanochromate has been demonstrated[38]. It is easy to foresee that this is not restricted to this composition but for any for which can be easily oxdised or reduced. In addition, the photo-induced change in the structure and magnetic properties of rubidium cobalt hexacyanoferrate has been shown[40]. In particularly beautiful work, Verdaguer and coworkers showed that the ligand field around the cobalt was vital to this behaviour.[97] Rubidium manganese hexacyanoferrate demonstrates both photo and temperature induced phase and magnetic transitions[104]. The material shows a large thermal hysteresis loop of 75 K or more. Other external stimuli that can alter the magnetic properties are pressure and humidity.[39]

1.4.1 Types of magnetism

Different materials respond to applied external magnetic fields in different ways. Materials that have no permanent magnet moments exhibit diamagnetism in which a small internal magnetic field is generated that opposes the external magnetic field. Unpaired electrons produce permanent magnetic moments within materials. If these magnetic moments do not interact the material exhibits paramagnetism. When exposed to an external magnetic field magnetic moments in paramagnetic materials align themselves with the applied field. When there is no applied field the magnetic moments are randomly orientated and produce no net magnetisation.

Materials which contain permanent magnetic moments that strongly interact can maintain ordering of magnet moments when no external field is applied leading to ferromagnetism, antiferromagnetism or ferrimagnetism. The first interaction between magnet moments to consider is the dipolar interaction which is the direct interaction between magnetic dipoles. In a two dipole system the strength of the interaction is dependent on the distance between the dipoles and their directions. In a many dipole system the strength of the interaction is the dot product of each magnetic dipole and the global magnetic field, summed over all magnetic dipoles. Magnetic dipolar interaction energies are typically very low and equivalent to a fraction of a Kelvin of thermal energy, and so dipolar interactions are too weak to account for permanent magnetic ordering that is observed at temperatures well above absolute zero.

A different interaction, known as the exchange interaction, is responsible for stronger interactions between neighbouring spins resulting in magnetic ordering at high temperatures. The exchange interaction is a quantum mechanical effect based on the Pauli exclusion principle and has no classical counterpart.[108] As two electrons cannot occupy the same quantum mechanical state, electrons that have overlapping orbitals must either have opposite spin or antisymmetric spacial wavefunctions. In

ferromagnetic materials the lowest energy configuration having all spins aligned parallel to eachother. Above the Curie temperature the thermal energy becomes greater than the exchange energy, the spins no long align to each other and the material exhibits paramagnetism. In antiferromagnetic and ferrimagnetic materials neighbouring spins align antiparallel. The difference being antiferromagnetic materials produce zero net magnetisation whereas ferrimagnetic materials produce a small but non-zero net magnetisation. Like ferromagnetic materials, above a critical ordering temperature antiferromagnetic and ferrimagnetic materials exhibit paramagnetism. For antiferromagnetic and ferrimagnetic materials the critical ordering temperature is called the Néel temperature.

Within many compounds transition metal ions are separated by non metals, such as oxygen or cyanide ligands as in the case of PBAs. In these compounds the exchange interaction between metal centres is mediated by the nonmetal ligand orbitals. This is known as a superexchange interaction. In these systems the stronger the degree of covalency, the greater the overlap between metal and ligand orbitals, the stronger the exchange interaction, and the higher the magnetic ordering temperature.

1.4.2 Measurement of magnetic properties

The nature of magnetic ordering within a material is studied by measuring the magnetic susceptibility of the material as a function of temperature. The magnetic susceptibility, χ, is a measure of how a material will become magnetised in the presence of an external magnetic field. It is defined as the relationship between the strength of the applied magnetic field, H, and the magnetisation of the material, M.

$$M = \chi H \tag{1.5}$$

Diamagnetic materials have a magnetic susceptibility of between 0 and -1 whereas

the magnetic susceptibility of paramagnetic, ferromagnetic, antiferromagnetic and ferrimagnetic materials are greater than 0. Differences in susceptibility between materials exhibiting these types of magnetism are shown in Figure 1.10. The reciprocal of susceptibility is linear with temperature above the magnetic ordering temperature. The x-axis intercept of a line fitted to this region extrapolated to lower temperature is characteristic of the type of magnetic ordering. For paramagnetic materials the intercept is at 0 K, the intercept for ferromagnetic materials is greater than 0 K, and the intercept for antiferromagnetic or ferrimagnetic materials is less than 0 K.

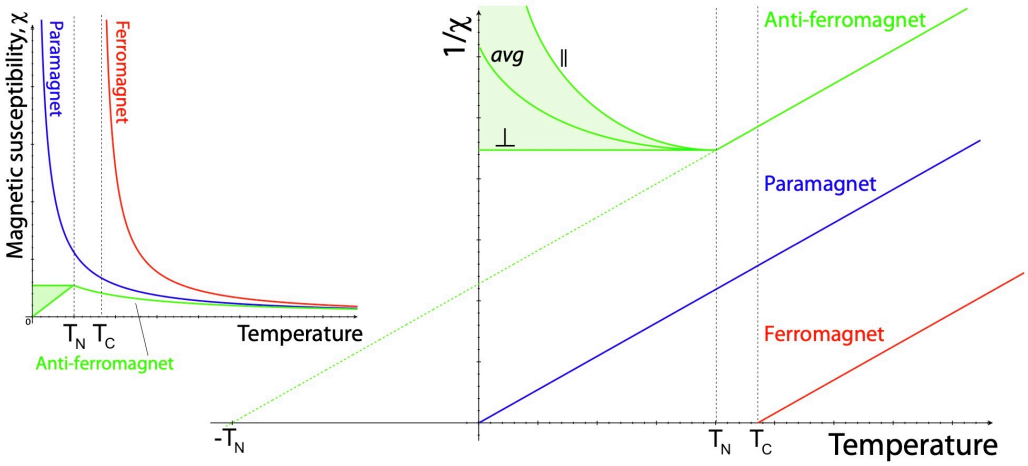


Figure 1.10: The relationship between the magnetic susceptibility and temperature for different types of magnetic materials. T_C and T_N are the Curie temperature and Néel temperature, respectively. Reproduced from ref[108].

The magnetic ordering temperature of ferromagnetic and ferrimagnetic materials are most often observed experimentally by measuring how the magnetisation of the material changes as the temperature is increased under an applied magnetic field, see Figure 1.11. Below the ordering temperature the magnetisation is high as the magnetic moments are aligned. Above the ordering temperature the thermal energy is greater than the exchange energy which disrupts the alignment of magnetic moments and the material exhibits paramagnetism. Since antiferromagnetic materials do not have a net magnetisation below the magnetic ordering temperature this method cannot be used to observe the magnetic ordering temperature.

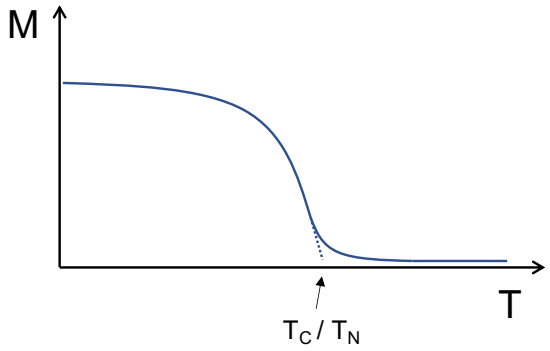


Figure 1.11: A schematic representation of a field cooled magnetisation curve.

M-H curves study the magnetic hysteresis of magnetic materials and consist of cycling the external magnetic field, H, between high positive and negative values and recording the magnetisation, M, see Figure 1.12. The remnant magnetisation is the residual magnetisation a material has once the external field is removed. The coercive field is the magnitude of external magnetic field necessary to reduce the magnetisation to zero. 'Hard' magnetic materials are characterised as having high coercive fields, whilst 'soft' magnetic materials have low coercive fields.

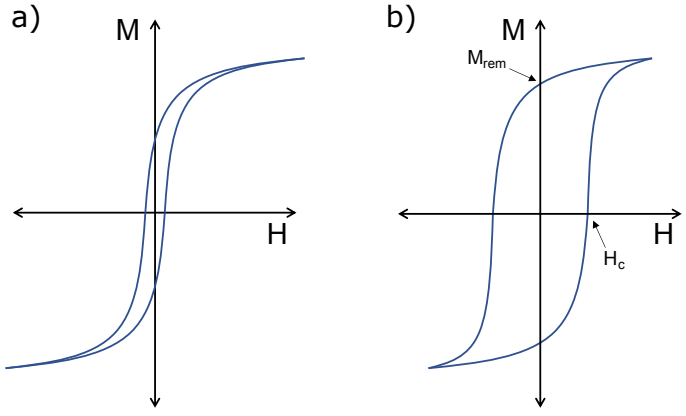


Figure 1.12: Schematic of M-H curves for a) soft and b) hard magnets. The coercive field (H_c) and remnant mangetisation (M_{rem}) of the M-H curve in panel b are labelled.

1.4.3 Interaction between spin centres

The magnetic interaction between two neighbouring spin centres with spin S1 and S2 is described by the Hamiltonian

$$H = -2JS_1.S_2 \tag{1.6}$$

where J is the exchange interaction coefficient. The spin of the ground state depends on the magnitude of $S1$ and $S2$ as well as the sign of J. In the case of PBAs this can be thought of the interaction between two metals centres bridged by a cyanide ligand, which is an example of the superexchange mechanism. Due to the long bond distances to a first approximation it is sufficient to consider only nearest neighbour interactions. The sign of J describes the type of coupling, whether ferromagnetic ($J >0$) or antiferromagnetic ($J <0$).

The nature of magnetic exchange interaction depends on orbital symmetry, as described previously. Electrons in orthogonal orbitals on neighbouring sites (t_{2g} and e_g) align parallel contributing to the ferromagnetic exchange term, whilst electrons in non-orthogonal orbitals align antiparallel contributing to the antiferromagnetic exchange term.[106] The net J value is the sum of ferromagnetic and antiferromagnetic terms. Due to having such as large crystal field splitting energy the R-site transition metal only ever has unpaired t_{2g} electrons (more than six electrons is unstable due to high energy e_g orbitals). The P-site transition metal can have unpaired t_{2g} or e_g electrons, or both. Three interactions arise based on this; purely ferromagnetic, purely antiferromagnetic, or mixed (ignoring diamagnetic centres). Examples of such systems are vanadium(II) hexacyanochromate(III) (t_{2g}-t_{2g}), nickel(II) hexacyanochromate(III) (e_g-t_{2g}), and manganese(II) hexacyanochromate(III) (e_g/t_{2g}-t_{2g}), respectively.

Assuming both transition metal sites are paramagnetic, the resultant net magnetisation can be ferromagnetic (if net ferromagnetic interaction), antiferromagnetic (if net

antiferromagnetic interaction between spins of the same magnitude) and ferrimagnetic (if net antiferromagnetic interaction between spins of different magnitude). Once long range ordering is taken into account antiferromagnetic behaviour can be avoided if, for example, vacancies are present so the sublattices have different total spins.

1.4.4 Mean field and ligand field models

The mean field model developed by Weiss and later Néel[109] describes the magnetic properties of insulating solids and has been successfully applied to PBAs. It assumes the magnetic moments of each interpenetrating sublattice, each transition metal site in PBAs, are aligned parallel. The magnetic ordering temperature, T_c, is given by equation[106]

$$kT_c = \frac{Z|J|C_A C_B}{N_A g^2 \beta^2} \tag{1.7}$$

where Z is the number of magnetic neighbours, C_P and C_R are the Curie constants for transition metals sites P and R, g is the mean Lande factor for P and R, and β is the Bohr magneton. In PBA materials to maximise T_c you must maximise Z by reducing the vacancy content, maximise J by changing the metal species, and maximise C_P and C_R by ensuring the maximum number of unpaired electrons.

Ligand field theory is required to understand the exchange mechanism across the cyanide bridge, the delocalisation of spin, and the magnitude of J. Delocalisation of spin from the transition metal happens through both σ and π bonding. It appears that delocalisation of the t_{2g} electrons onto the cyanide π^* antibonding orbitals is the most prominent mechanism.[106,110] Therefore, it is predicted that unpaired electrons in high-energy, more diffuse t_{2g} orbitals lead to stronger coupling and so earlier transition metals in lower oxidation states will give higher $|J|$ values.

1.4.5 Comparison to experimental data

A summary of experimental data is shown in Figure 1.13. Most experimental data uses $Cr(CN)_6^{3-}$ as the R site complex (filled inverted triangles) as it is chemically stable and has the maximum spin of 3/2. Exchanging different P^{2+} species aligns with theory; P site species with only e_g electrons exhibit ferromagnetic behaviour and those with only t_{2g} electrons exhibit ferrimagnetic behaviour.[106] Interestingly, antiferromagnetic interactions produce a larger $|J|$ than ferromagnetic interactions, which in combination with the larger number of possible interaction pathways (9 instead of 6), leads to higher magnetic ordering temperatures. High temperature magnetic ordering is only possible with antiferromagnetic interactions. The effect of vacancy content is also observed; the lower the vacancy content the greater number of magnetic interactions and the higher the ordering temperature, for a given composition. By studying isoelectric compounds it is clear that earlier transition metals in lower oxidation states on the R site produce a larger $|J|$ as higher energy, more diffuse t_{2g} electrons interact more with the cyanide π^* orbitals, as predicted from the overlap model[99]. It is not clear, however, if this effect is also the case for P site metals as the bonding to the cyanide ligand is considerably different in character.

1.4.6 Vanadium(II) hexacyanochromate(III)

Of all PBAs materials vanadium(II) hexacyanochromate(III) is the only composition with room temperature magnetic ordering. V^{2+} and Cr^{3+} both have three unpaired t_{2g} electrons giving the maximum Curie constants and number of magnetic interaction pathways. It was first reported as an amorphous material, $V^{II}[Cr^{III}(CN)_6]_{0.86}$, with an ordering temperature of 315 K by Vedaguer and coworkers in 1995.[95] By using a sol-gel synthesis route, leading to increased crystallinity and lower vacancy content, the ordering temperature was increased to 376 K, Figure 1.14.[100] The stoichiometric

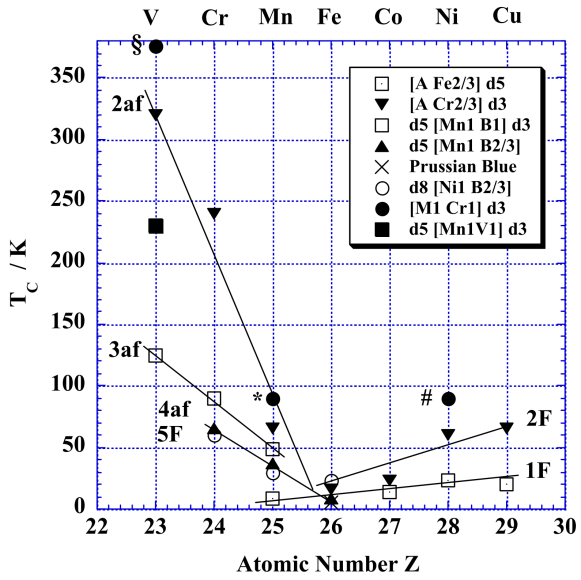


Figure 1.13: A graph displaying the Curie temperatures of a number of PBA compositions. Atomic number Z refers to the P site metal, the R site metal is given by the legend. Reprinted with permission from ref[106]. Copyright © 2004 WILEY-VCH Verlag GmbH & Co. KGaA, Weinheim.

material would be antiferromagnetic, as both metals are t_{2g}^3, however, the material is still ferrimagnetic with a small saturation magnetisation due to a non-zero vacancy content and partial V^{2+} oxidation to V^{3+} or VO^{2+}. Synthesis of vanadium hexacyanochromate is unreliable and its magnetic properties degrade if exposed to air. A mixed-valence vanadium(III/II) hexacyanochromate(III) was reported by Miller and coworkers that maintained a magnetic ordering temperature of 372 K after exposure to air.[111]

1.4.7 Current state of PBA magnetism research

Research throughout the 90s reached a pinnacle with the report of room temperature magnetisation exhibited by vanadium(II) hexacyanochromate(III). There has been no significant progress since the year 2000 and no commercialisation of these materials, even with computational studies pointing directions and apparent applications.[112] There are a number of reasons for this. First, PBA compositions cannot be synthesised

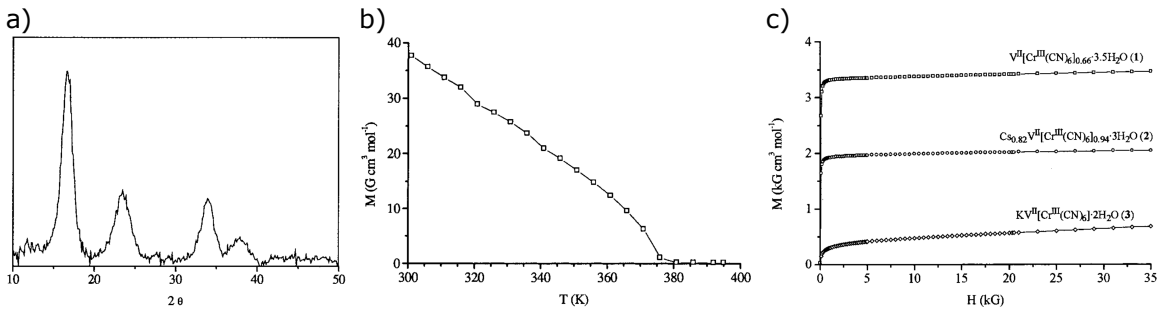


Figure 1.14: Characterisation of potassium vanadium hexacyanochromate, $K_1V^{II}[Cr^{III}(CN)_6]_1$. a) X-ray diffraction pattern, b) field-cooled magnetisation, and saturation magnetisation (compared to other compositions). Reprinted (adapted) with permission from ref[100]. Copyright © 1999 American Chemical Society.

in a reliable and repeatable manner that controls for exact composition, vacancy content, particle size, bond angles, and many compositions have not been successfully synthesised at all. It is clear that magnetic properties are determined not only by the transition metals but by these other parameters, and their dependence on magnetic ordering temperature has not been sufficiently studied. For example, increasing crystallinity clearly increases the magnetic ordering temperature for a given composition but crystallinity cannot be reliably tuned for many compositions and therefore its impact has not been systematically studied. Additionally, parameters cannot be changed independently of all other factors and so cannot be studied. An example is bond angles which depend on metal species, oxidation state and vacancy content. Second, no one computational method accurately models the magnetic properties and many omit crucial factors. This leads to great overestimation in computed J values and predicted ordering temperatures.[112,113] Experimental data to fit or validate results from computational models have all the issues discussed above.

1.5 Synthesis of Prussian blue analogues

On first inspection the synthesis of PBA materials is very simple. An aqueous solution containing transition metal ions P^{j+} is mixed with an aqueous solution containing a

transition metal anion complex, $R^k(CN)_6^{(k-6)}$ and the PBA, $A_xP[R(CN)_6]_{1-y}$, precipitates out of solution.

$$xA^+_{(aq)} + P^{j+}_{(aq)} + (1-y)R^k(CN)_6{}^{k-6}{}_{(aq)} \rightarrow A_xP^j[R^k(CN)_6]_{1-y\ (s)} \tag{1.8}$$

Alkali metals, or other positively charged species, present in solution can occupy interstitial sites. The stoichiometry of the precipitated material depends on the oxidation state of the species. Either interstitial species or hexacyanometallate vacancies can provide charge neutrality, and so a range of composition is possible for many PBA materials. However, this description is an oversimplification and there are many properties of the synthesised material, in addition to stoichiometry, that a chemist would like to control. These properties include particle size, crystallinity, morphology, water content, and inclusion of other ionic or solvent species.

Available P site species are V through Zn and available R site species are V through Co. Possible A site species are Li through Cs and other divalent and molecular cations. P site transition metals must be kinetically labile to take part in the precipitation reaction. Stable R site complexes used in PBA synthesis include V(II) Mn(II) Ti(III) Cr(III) Mn(III) Fe(III) Co(III) Mn(IV) Pt(IV). Precursors must be stable (enough) against disproportionation, hydrolysis or oxidation.

In some cases the R site complex can be formed in situ. For example, synthesis from Mn^{2+} and CN^- will form $Mn(CN)_6^{4-}$ as an intermediate compound, which then reacts with remaining Mn^{2+} to form $A_xMn[Mn(CN)_6]_{1-y}$.[17] Also, acid decomposition of $Fe(CN)_6^{3-}$ produces Fe^{3+} which is reduced to Fe^{2+} which then reacts to form $A_xFe[Fe(CN)_6]_{1-y}$.[82] These types of synthesis can effectively limit the availability of one of the precursors resulting in limited nucleation and growth of large crystalline particles.

Particle size and crystallinity can be explained by classical nucleation theory (CNT) and LaMers nucleation theory. Rapid nucleation followed by only limited

growth of particles leads to small, low crystallinity particles.[114] Slow, or limited, nucleation followed by a sustained period of particle growth results in large highly crystalline particles. The thermodynamics of reaction are primarily determined by the precursor species (composition) and the kinetics, although dependent on the composition, can be effectively influenced by reducing precursor concentrations or increasing the temperature.

For a given set of precursors there is a range of possible composition given by the charge neutrality mechanism. Factors that determine the vacancy content, and interstitial cation content, are not well understood. In the magnetic materials literature PBAs are typically in the mixed valence state and are synthesised with a high vacancy content in the presence of sodium or potassium in solution. To decrease the vacancy content cesium is added to solution.[93,104] As battery materials, the interstitial site species is typically restricted to sodium or potassium by the application of the material. In this case to reduce the vacancy content the concentration of alkali cations are increased, often to the solubility limit.[67] Experimentally it has been found that reducing the vacancy content is only possible by this method when the material is in the reduced state and it is not extremely effective, typically 10% vacancies remain in the material. In recent years adding a chelating agent, typically citrate, to the P^{j+} precursor has proved successful in reducing the vacancy content and increasing the particle size and crystallinity of the synthesised material by slowing the precipitation reaction.[77,87] These methods have been developed from empirical bases and there are limited satisfactory explanations as to why they work.

The water content of a PBA material can vary depending on synthesis conditions and vacancy content, but also storage conditions. Other ionic or solvent species in solution can be incorporated into the precipitate material if they are sufficiently small.

Other changes can take place from the precursor chemicals to the precipitated PBA which can be rationalised by reducing the total energy of the system. If Prussian blue

is synthesised from Fe^{2+} and $Fe(CN)_6^{3-}$ there will be intermetallic charge transfer and $Fe^{III}[Fe^{II}(CN)_6]_{0.75}$ will be formed, as the reduction potential of the hexacyanoferrate complex is increased above that of $Fe^{3/2+}$ when it is incorporated into the crystalline lattice. Also, there can be isomerism of the cyanide ligand which is particularly prevalent for transition metal hexacyanochromate compounds. For example, iron hexacyanoferrate can be converted into chromium hexacyanoferrate.[115]

To synthesise PBA nanoparticles with a narrow particle size distribution and control of particle shape colloidal methods have been developed.[116–119] These methods, known as microemulsion or micelle synthesis methods, consist of using an immiscible solvent mixture such as oil and water with the addition of a surfactant. Reverse micelles refers to when the fraction of water is low and water droplets are formed in the colloidal mixture stabilised by the surfactant. PBAs synthesised in reverse micelles typically have much narrower size distributions compared to alternative synthesis methods and their average size can be controlled by changing the synthesis conditions. Properties, such as magnetic properties, that are highly dependent on particle size and shape have been studied by synthesising PBA nanoparticles using such methods.[117,119]

1.6 Thesis objectives

Prussian blue analogues are an intriguing, complex family of materials that find diverse applications. As battery materials they are among the best performing sodium- and potassium-ion cathode materials, exhibiting extremely high rate capability and cyclability whilst also being low in cost. To fully utilise their excellent properties in a full cell an anode material of equivalent performance is required, an obvious candidate being another PBA material. So far, PBA compositions that are electrochemically active at low potentials, that can function as anode materials, have exhibited poor performance and limited by relatively high redox potentials and low specific capacities.

There is clear motivation to search for lower reduction potential, higher capacity PBA compositions. In addition, due to the increased interest in solid state batteries the intriguing and unique possibility of an all-PBA solid-state battery, where the cathode, anode, and electrolyte are PBA materials, warrants exploring.

The objectives of this thesis are to explore new PBA compositions that provide higher performance as anode materials and that can be used as a solid electrolyte. In the pursuit of these objectives significant advances in synthesis methodology and understanding, as well as the synthesis of a new material of interest for its magnetic properties, have been made.

A detailed outline of the thesis's objectives are as follows:

1. Structural and electrochemical properties of manganese hexacyanochromate (Chapter 3)
    - Characterise the crystal structure, bonding, and water in manganese hexacyanochromate
    - Evaluate the electrochemical properties in a 'water-in-salt' electrolyte
    - Investigate the charge storage mechanism and limit of stability at low potential
2. Synthesis of zero-vacancy chromium(III) hexacyanochromate(III) (Chapter 4)
    - Develop a synthetic procedure to produce zero-vacancy chromium(III) hexacyanochromate(III)
    - Identify the key parameters that enable the synthesis
    - Characterise the electrochemical and magnetic properties of chromium(III) hexacyanochromate(III)
3. Holistic thermodynamic and kinetic model for determining the charge neutrality mechanism in PBA synthesis (Chapter 5)

- Formalise the PBA synthesis in a manner that can be examined from a theoretical perspective
- Understand parameters that determine the charge neutrality for a given PBA reaction based on experimental evidence and basic thermodynamic and kinetic principles
- Generate conclusions from the model that inform the design of new PBA syntheses

4. Sodium zinc hexacyanoferrate as a solid electrolyte material (Chapter 6)

    - Identify a candidate PBA solid electrolyte material
    - Characterise how the structure and properties of sodium zinc hexacyanoferrate is dependent on applied pressure and water content
    - Examine the electronic conductivity and electrochemical stability window of sodium zinc hexacyanoferrate

Chapter 2

Methods

2.1 Synthesis 38
2.2 Physiochemical characterisation 40
2.2.1 Powder X-ray diffraction 40
2.2.1.1 Rievteld refinement 41
2.2.2 Scanning electron microscopy 43
2.2.3 Fourier-transform infrared spectroscopy 44
2.2.4 Simultaneous thermal analysis 47
2.2.5 Inductively coupled plasma - optical emission spectroscopy . . 48
2.2.6 Dynamic light scattering 49
2.3 Electrochemical characterisation 49
2.3.1 Three-electrode flooded cell 50
2.3.2 Solid-state impedance cell 51
2.3.3 Electrode preparation 52
2.3.4 Voltammetry 54
2.3.5 Galvanostatic cycling 55
2.3.6 Electrochemical impedance spectroscopy 56
2.4 Other techniques 61
2.4.1 Superconducting quantum interference device 61

2.1 Synthesis

Prussian blue analogues are conventionally synthesised through a co-precipitation reaction between aqueous precursors. One solution is added in a dropwise manner

to the second under vigorous stirring and a PBA compound rapidly precipitates. Experimental parameters such as precursor concentrations, temperature, dripping rate can be altered to control the precipitation reaction.

The precipitate is collected and washed through centrifugation. On centrifugation the precipitate is separated from the supernatant due to its higher density. Centrifuge rotation frequencies used range from 3000 to 12000 rpm and primarily depend on the particle size; smaller particles require higher speeds. After centrifugation the supernatant is poured away leaving the precipitate and a small amount of remnant liquid. More water is added to the centrifuge tube and the precipitate dispersed through agitation. This washing procedure is performed multiple times to ensure that all unreacted precursor chemicals are removed. The precipitate is placed in an oven overnight to remove any remnant water or other solvents. Once dried the material is scraped from the centrifuge tube and lightly ground to a fine powder in a mortar and pestle.

Manganese hexacyanochromate and sodium zinc hexacyanoferrate were synthesised in a conventional manner described above. In contrast, during the synthesis of alkali-metal chromium(II) hexacyanochromate(II) compounds a nonaqueous solvent was used instead of water and the synthesis was performed in an Ar-filled glove box. The precipitate was collected and washed through centrifugation with the same nonaqueous solvent and acetonitrile. Vials and centrifuge tubes were sealed to avoid air exposure during centrifugation. Materials were dried in a furnace under vacuum without air exposure. These changes were necessary as the precursors and product of the alkali-metal chromium(II) hexacyanochromate(II) syntheses were unstable in air or in contact with moisture, primarily due to oxidation of Cr^{2+}. Much smaller particles with lower crystallinity were produced which was a result of not only the nonaqueous synthesis but also the composition. Discussion and further details on the synthesis of manganese hexacyanochromate, sodium zinc hexacyanoferrate, and alkali-metal

chromium(II) hexacyanochromate(II) compounds can be found in their respective chapters.

2.2 Physiochemical characterisation

2.2.1 Powder X-ray diffraction

Diffraction-based techniques are fundamental when characterising the crystal structure of crystalline materials. These techniques rely on scattering between incident waves and atoms in an ordered lattice. Scattered waves can interfere constructively, if they are in phase, or destructively, if they are out of phase. Bragg's law, below, defines the relationship between radiation wavelength (λ), angle of incidence (θ), and interplanar spacing (d) that gives rise to constructive interference. n is a non-zero positive integer.

$$n\lambda = 2dsin(\theta) \tag{2.1}$$

Bragg's law applies to X-rays, neutrons, and electrons as each can behave as a wave. In a typical experiment the intensity of the diffraction beam is recorded as a function of angle 2θ.

In this thesis, only powder X-ray diffraction (XRD) data is presented. XRD diffraction is the most commonly used method as X-rays are easily produce and they have wavelengths that are of a similar order of magnitude as interplanar spacings in crystalline materials.[120,121] X-rays scatter with electrons in atoms and, therefore, the atomic scattering factor, f_i, increases with atomic number. Additionally, the intensity of the scattered beam decreases with increasing angle, 2θ, which is corrected using the Lorentz-polarization (Lp) factor, which incorporates two different corrections. Firstly, the Polarization correction is required as the intensity of scattering of electromagnetic radiation is proportional to the sine of the diffraction angle, 2θ. Secondly, the Lorentz

factor which corrects for the length of time the detector sits in the diffracting position for any given reflection.

Powder XRD refers to performing XRD on powder samples that contain a large number of randomly orientated crystalline domains. Powder XRD analysis assumes that for each set of planes there is a statistically significant number domains orientated correctly (the plane perpendicular bisects the incidence and diffracted beam), so that each possible diffraction peak is observed.[120] Data presented in this thesis is from both lab and synchrotron X-ray sources, for which the X-ray wavelengths are different. All lab XRD measurements were from instruments with a copper X-ray sources, therefore producing copper Kα radiation with an average wavelength of 1.541 84 Å. X-rays produced from the synchrotron source has significantly higher flux and a wavelength of approximately 0.825 Å, which was calibrated using silicon standard for each measurement session.

XRD patterns can be simulated from a model structure using software such as VESTA.[122] This is powerful tool as changes in site occupancy, in particular for large alkali cations such as rubidium and cesium in PBAs, have a minor effect on the unit cell symmetry or lattice parameters but a significant effect on relative peak intensities and can, therefore, be used as a proxy for alkali cation content.

An example of a powder XRD pattern of a PBA, in this case manganese hexacyanochromate, is shown in Figure 2.1. The XRD pattern has been refined and major reflections have been assigned. The PBA structure is well-known and there are many reference patterns for peak assignment. In addition, as the structure is high symmetry and relatively simple (FCC) the allowed reflections can be easily predicted.

2.2.1.1 Rievteld refinement

Rietveld refinement, named after Hugo Rietveld who first described it, is a method to generate a model crystal structure from powder X-ray or neutron diffraction data.[124]

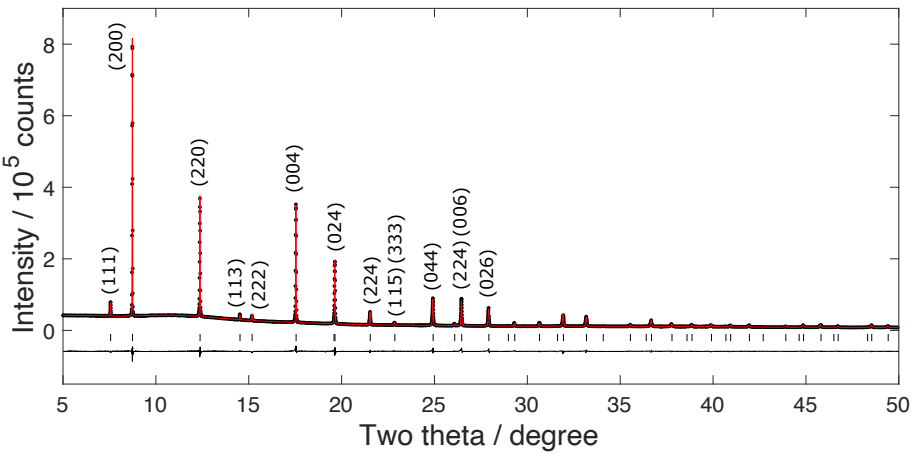


Figure 2.1: An XRD pattern of manganese hexcayanochromate that has the standard PBA crystal structure (space group *Fm-3m*). Black dots are data points, the red line is the fitted profile and the black line is the residual. Vertical black lines are the positions of reflections and some reflections are assigned. The X-ray wavelength was $\lambda = 0.824\,53\,\text{Å}$. Reprinted (adapted) with permission from ref[123]. Copyright © 2013 American Chemical Society.

The method uses a least-square minimization of a simulated diffraction pattern, from a model, to best match experimental data. A simplified description of the procedure is as follows. Firstly, the position and relative intensities of each reflection is determined by the model unit cell symmetry, lattice parameters, and structure factors. Secondly, these reflections are convolved with peak shape functions that account for instrument and material broadening. Thirdly, these peaks are summed with a background function. Fourthly, the simulated diffraction pattern is compared to the experimental pattern and a 'goodness of fit' value is calculated. Lastly, model, peak shape, and background parameters are adjusted iteratively to minimise the 'goodness of fit' value.

There are a number of parameters that describe the 'goodness of fit' of a model to experimental data.[125] The most common parameters are weighted profile R factor, R_{wp}, and expected R factor, R_{exp}. R_{wp} is a discrepancy index that takes the square root of of the summed differences between the model and experimental, scaled by the observed intensities. R_{exp} is the best possible R_{wp} for a given data set. The χ^2, often termed 'goodness of fit' is the ratio between these two factors. These parameters are

defined as follows:

$$R_{wp}^2 = \sum_i w_i[y_i(calc.) - y_i(obs.)]^2 / \sum_i w_i y_i(obs.)^2 \tag{2.2}$$

$$R_{exp}^2 = (N - P) / \sum_i^N w_i y_i(obs.)^2 \tag{2.3}$$

$$\chi^2 = R_{wp}^2 / R_{exp}^2 \tag{2.4}$$

where w_i is the weighting of each intensity difference, y_i is the intensity, N is the number of observations and P is the number of refined parameters.

It should be noted that goodness of fit values alone are not sufficient to evaluate to success of a refinement and, instead, more important are visual inspection of the Rietveld fit and ensuring the model is chemically plausible.[125]

GSAS and GSAS-II software is used for Reitveld refinements throughout this thesis.[126–128]

2.2.2 Scanning electron microscopy

Scanning electron microscopy (SEM) is a powerful tool for imaging samples at small length scales.[129] SEM uses electrons, providing much higher resolutions that optical microscopes due to their smaller wavelength. Electrons are produced from a source, either by thermal emission or field emission, accelerated in an electric field and focussed to a spot on the sample using electromagnetic condenser and objective lenses, and apertures. The electron beam is rastered across the sample surface and an image is formed by mapping signal intensity (grayscale) against electron beam position. Three primary signals are detected and used for imaging and analysis; secondary electrons, backscattered electrons, and characteristic X-rays. Secondary electrons are electrons ejected from the sample atoms through inelastic scattering with incident electrons.

They are of low energy and have a relatively short escape depth. The detector is positively charged, attracting the electrons that are ejected in any direction. Due to the short escape depth secondary electrons give greater surface detail and higher resolution. Backscattered electrons are incident electrons that scatter inelastically on samples atoms. They are of high energy leading to longer escapes depths in a greater interaction volume, leading to less surface detail and lower resolution. The intensity of backscattered electrons depends significantly on the atomic number of sample atoms, giving atomic number contrast. The detector is placed above the sample around the incident electron beam and is not positively charged as this would have a negligible effect on the electrons as they are of high energy. Characteristic X-rays are produced when incident electrons eject inner shell electrons of sample atoms which leads to an outer shell electron filling the vacancy and emitting an X-ray. These X-rays are *characteristic* as their wavelength is determined by the energy difference between discrete electron energy levels and, therefore, quantised and specific to each element. SEMs are often equipped with a X-ray detector for analysis of characteristic X-rays emitted from the sample, a technique known as energy dispersive X-ray spectroscopy (EDX). EDX identifies elements present in a sample and can be used for quantitative element analysis, although with only moderate precision ($\approx 1\%$). It is common to map EDX spectra to gain information about the spacial distribution of elements in a sample.

Examples of secondary electron SEM images of potassium manganese hexacyanoferrate with a range of particle sizes are shown in Figure 2.2. In PBA research SEM is most often used to observe the particle size and shape of as-synthesised material.

2.2.3 Fourier-transform infrared spectroscopy

Infrared (IR) spectroscopy is the study of a material by its interaction with infrared radiation.[131] An IR spectrum is the absorption or transmission of IR radiation as

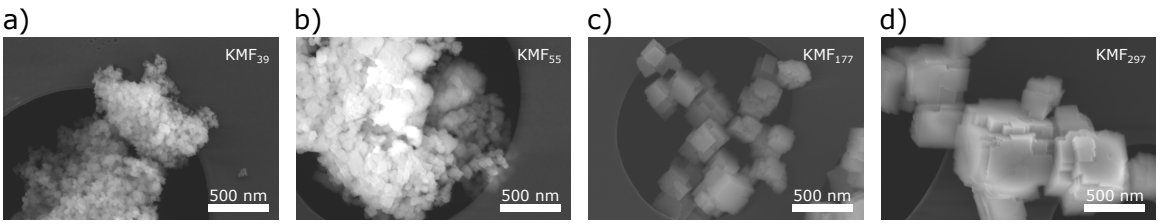


Figure 2.2: SEM images of four potassium manganese hexacyanoferrate samples with a range of particle sizes. Reprinted (adapted) with permission from ref[130]. Copyright © 2020 American Chemical Society.

a function of energy, the conventional unit of frequency being cm^{-1}. A bond, or functional group, will absorb infrared radiation at its resonant vibrational frequency, and most resonant vibrational frequencies are in the mid-infrared region, 4000 to $400\,cm^{-1}$. There are many different modes of vibration including symmetric stretch, asymmetric stretch, scissoring, rocking, wagging and twisting. The number of modes for a given molecule depends on the number of vibrational degrees of freedom; 3N - 5 for linear molecules and 3N - 6 for non-linear molecules (N is the number of atoms in the molecule). For a vibrational mode to be IR active is must induce a change in dipole moment. The resonant frequencies are a function of the masses of the atoms, the strength of the bond, and the molecular potential energy surfaces Resonant frequencies of common functional groups are well known, including those in PBAs.

Fourier-transform infrared (FTIR) spectroscopy is the preferred method of IR spectroscopy. Compared to standard scanning (dispersive) spectrometry it gives greater signal to noise for the same scan time, as it gathers information for many wavelengths simultaneously, and can have greater wavelength accuracy as its calibrated by a laser of known wavelength.[131] Using a beam splitter and mirrors the FTIR spectrometer generates a beam of light that contains many wavelengths that is incident on the sample and the signal, whether in transmission of reflection, is measured. By moving one of the mirrors the wavelengths present in the light source produced changes. After taking spectra for many mirror positions a reconstructed 'interferogram' is produced. The term *Fourier-transform* is arises as a Fourier transform is required during data

processing to produce the interferogram.

Two sampling techniques were used in this thesis. The first is attenuated total reflection (ATR) mode in which the IR beam is contained within a crystal, such as diamond, via total internal reflection. The powder sample is pressed onto the surface of the crystal and an evanescent wave extends into the sample by a few microns. The second mode is transmission mode in which a small amount of sample is pressed into a pellet with an IR transparent binder, such as cesium iodide.

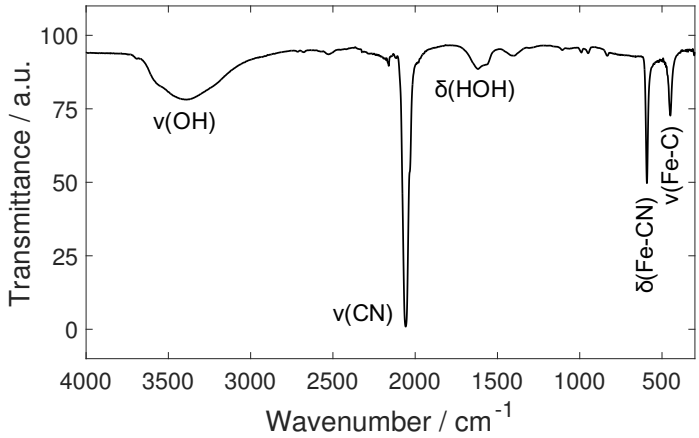


Figure 2.3: A FTIR spectrum of potassium manganese hexacyanoferrate taken in ATR mode. Adapted from ref[130].

IR spectroscopy is valuable technique for studying PBAs. Firstly, the frequency of the cyanide stretch, ν(CN), in the range 2000 to 2300 cm^{-1}, is dependent on its bonding environment; the transition metal species its bonded to and their oxidation state.[23,132,133] The cyanide donates electron density through the σ bond to the transition metal bonded to the carbon atom, and receives electron density onto its π^* orbitals through backbonding. This π backbonding weakens the cyanide bond and shifts its resonant frequency to lower wavenumbers. The amount of backbonding, and therefore the shift in resonant frequency, is dependent on the R site transition metal and its oxidation state, and also the polarizing effect of the P site transition metal. Secondly, water molecules with different bonding environments within the PBA structure produce distinct FTIR spectra. Water has an absorption band, $\delta(H_2O)$,

at around 1600 cm^{-1} from a bending vibration, and O-H symmetric and asymmetric stretches, v(OH), between 3400 and 3700 cm^{-1}.[134] In the gaseous state the IR spectra of water is dominated by rotational-vibrational coupling giving rise to many absorption bands, whereas in the liquid state absorption bands are broad and shifted to lower wavenumbers due to extensive hydrogen bonding. A typical FTIR spectrum of a PBA material, potassium manganese hexacyanoferrate, is shown in Figure 2.3.

2.2.4 Simultaneous thermal analysis

Thermal analysis is the study of how properties of materials change with temperature. Simultaneous thermal analysis (STA) is the simultaneous application of thermogravimetry (TG) and differential scanning calorimetry (DSC). TG is a technique in which the mass of a sample is measured over time or as a function of temperature. TG is useful if there are changes in mass as the sample is heated, for example, if gases are evolved or if the materials undergoes an oxidation reaction. DSC is a technique in which the heat required to maintain the same temperature between the sample and a reference in measured. DSC can be used to identify if chemical reactions take place. In addition, the instrument is coupled to a mass spectrometer via a capillary for concurrent simultaneous thermal analysis - mass spectrometry (STA-MS). As the STA measurement is taking place the gas headspace is sampled to identify gases given off during the measurement.

In this thesis samples are studied using STA-MS under a constant heating ramp under inert atmosphere. Typically, the samples are loaded into the instrument and the atmosphere is evacuated and refilled twice with argon. Under a constant argon flow the temperature in increased at 5 K/ min up to 500 °C. STA-MS is a useful tool to study water in the structure of PBAs. As the temperature is increased water leaves the structure, between 100 and 200 °C, resulting in a decrease in mass, an endothermic peak in the DSC trace, and peaks in the MS trace at m/z (mass over charge) values

of 17 and 18. Additionally, at higher temperatures mass loss steps and evolving gases such as carbon dioxide and cyanide suggest breakdown of the crystalline structure. This is currently the best method for measuring the water content in PBA materials. A literature example of TG curves for a number of PBAs displaying different behaviour are shown in Figure 2.4.

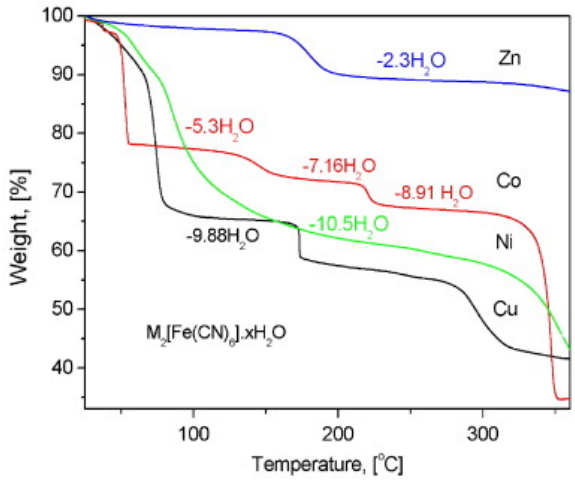


Figure 2.4: TG curves for a number of transition-metal hexacyanoferrate compounds. Reprinted from ref[135] with permission from Elsevier.

2.2.5 Inductively coupled plasma - optical emission spectroscopy

Inductively coupled plasma - optical emission spectroscopy (ICP-OES) is a type of emission spectroscopy that uses an inductively coupled plasma to produce ions in the excited state which then decay into a ground state and emit light of characteristic wavelength.[136] The inductively coupled plasma is a specific type of plasma that is maintained via induction from a high-frequency magnetic field. The material of interest is dissolved, or digested, into solution (usually 2% HNO_3). The solution is then diluted so that each constituent element is within the range of detection of the instrument, and within the range of standards. Standards of each element of interest (or multi-element standards containing more than one element) are prepared with a range of known concentrations. Standards and sample solutions are fed into the

ICP-OES instrument, the elements ionized in the plasma, and light of characteristic wavelengths for each element present is emitted.[137] The emission intensity for standards generate a calibration curve of intensity versus concentration. The intensity of the sample solutions can then be compared to the calibration curve to calculate the concentration of each element. ICP-OES (or inductively coupled plasma - optical emission spectroscopy) is the preferred technique to measure the composition of Prussian blue analogues. In particular, the vacancy content which can simply be calculated from the concentrations of transition metals. When the same transition metal occupies both P and R sites this technique cannot be used.

2.2.6 Dynamic light scattering

Dynamic light scattering (DLS) is a technique used to determine the particle size distribution of particles in a suspension.[138] A monochromated light source is directed at the suspension and scatters off the particles. The diffracted light scattered from all the particles can interfere constructively or destructively. A number of snapshots of the resultant interference pattern are taken at small time intervals. As particles undergo Brownian motion the location of particles, and therefore the interference pattern, changes over time. The change in correlation between snapshots decays in approximately an exponential manner which can be related to the diffusion coefficient of particles in suspension, and using the Stokes-Einstein relationship a particle size distribution can be derived.

2.3 Electrochemical characterisation

Since the primary application of materials developed in this thesis are for battery applications it is clear that studying their electrochemical properties are fundamental. Here I will describe the experimental apparatus and basic electrochemical techniques.

2.3.1 Three-electrode flooded cell

Three-electrode flooded cells are often the first electrochemical cell used to study the fundamental electrochemical properties of new electrode materials.[139,140] They are easy to prepare in a repeatable manner with a range of working electrode formats, have a reference electrode for accurate measurement of voltage, and excess electrolyte which masks effects from electrolyte transport or electrolyte side reactions. A schematic of a three-electrode cell is shown in Figure 2.5a. The cell contains a relatively large volume of electrolyte in which the working, reference, and counter electrodes are immersed. When conducting electrochemical measurements the current flows between the working and counter electrodes, whilst the voltage is measured between the working and reference electrodes. For accurate measurement of the working electrode voltage it is important that the electrode voltage that it is measured in reference to, in the case of a three electrode cell the reference electrode, is stable. This means the reference electrode should have a robust, fixed potential and no current passing through it. In two electrode cells, such as coin cells, the counter electrode and reference electrode are the same and, therefore, the potential changes with polarisation. For a fixed potential the redox reaction, and concentration of participating ions in solution, must be held constant, as described by the Nernst equation.

Electrochemical measurements in this thesis used a Ag/AgCl pseudo-reference electrode. A pseudo-reference electrode is a reference electrode for which the participating ion in solution is of low or zero concentration. It is necessary to calibrate the potential using a chemical in solution with a fixed redox potential. The ferrocene redox couple was used for calibration. The Ag/AgCl pseudo-reference electrodes were prepared by immersing a silver wire in a NaCl solution slightly acidified with HCl and applying a small anodic current of around $10\,\mathrm{mA\,cm^{-2}}$. After a few minutes the dark AgCl layer could be observed. A platinum wire was used as the counter electrode. Figure 2.5b

shows an image of a three-electrode flooded cell with a PBA composite carbon cloth working electrode, a Ag/AgCl pseudo-reference electrode, and a platinum wire counter electrode.

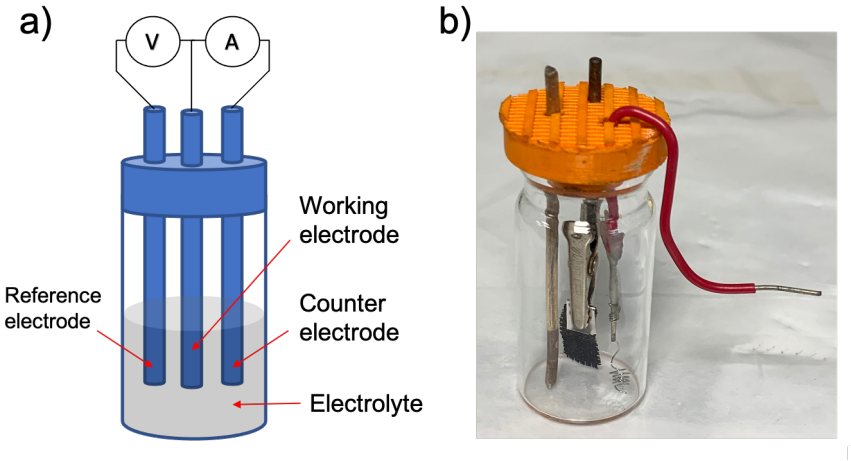


Figure 2.5: a) A schematic and b) digital image of a three-electrode flooded cell.

2.3.2 Solid-state impedance cell

To investigate the ionic conductivity of sodium zinc hexacyanoferrate, among other properties, it was necessary to design and build a cell. This cell was designed to densify the sodium zinc hexacyanoferrate powder into a pellet under uniaxial pressure and then perform electrochemical impedance spectroscopy and electrochemical measurements. For the body of the cell an electronically insulating, high strength, and chemically resistant material was required, and polyther ether ketone (PEEK) was used. For the plunger rods an electronically conductivity, high strength and chemically resistant material was required. A standard stainless steel would conventionally be used in this application but because high pressures were required a duplex steel was used. Duplex steels retain the corrosion resistance of stainless steel but have higher Young's modulus and higher ultimate tensile strength values. The surface of the steel in contact with the sample was sputtered with gold to ensure a good electrical contact. O-rings were used

to seal the cell. Approximately 100 mg of material was used for each measurement which, when compressed in the cell, formed a cylinder with a diameter of 8 mm and thickness of around 1 mm. In addition, an external clamp was designed to apply a small external pressure for when temperature dependent measurements were made inside an environmental chamber. Figure 2.6 shows images of the cell.

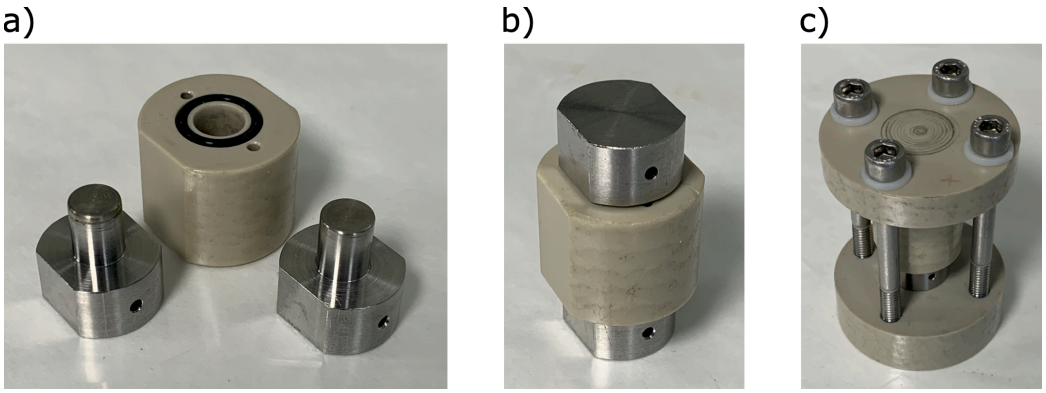


Figure 2.6: Digital images of the solid state impedance cell. a) The cell deconstructed, b) the cell constructed, and c) the cell in the external clamp.

2.3.3 Electrode preparation

To study the electrochemical properties of a material it is necessary to prepare electrodes. To ensure the electrode is robust a polymer binder is added to the active material to form a composite. Electrochemical reactions incorporate both ion and electron transfer. Ion transfer is provided by intimate contact between the active material and the liquid electrolyte. Electron transfer is provided by a electronically conducting pathway from the active material to the current collector. For electronically conducting material, such as graphite, this is provided by the active material, but for semiconducting or insulating active materials an electronically conductive additive is added to the composite. The conductive additive is usually a form of carbon. Any materials added to the composite should be electrochemically inactive in the voltage range of operation.

For experiments presented in this thesis the binder used was PVDF (Kynar 2850 GL), the carbon additive used was carbon black (Timical SUPER C65) and the current collector used was carbon cloth (Fuel Cell Store plain carbon cloth). PVDF is the most commonly used binder in both research and commercial cells because of its high electrochemical, chemical and thermal stability, its selective solubility, and it provides good adhesion between the composite electrode and current collector. Carbon black is commonly used as electronically conducting additive due to its high electrical conductivity, good dispersibility and high surface area which forms a percolating network even at low weight fractions. Carbon cloth is commonly used as a current collector in research flooded cells as it is easy to handle and prepare electrodes with.

The ratio of materials in the composite depend on the active material and purpose of the experiment. In this thesis the mass ratio between active material, polymer binder, and carbon additive was 8:1:1. This is a higher fraction of carbon and binder compared to commercial cells but is a common ratio used in research work as effects from binder and carbon are minimised.

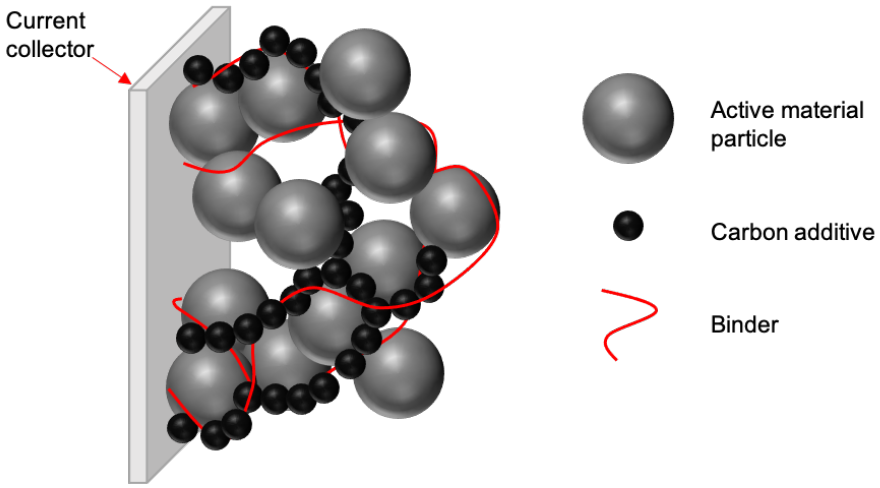


Figure 2.7: A schematic representation of an electrode containing the current collector, active material particles, carbon additive and binder.

Electrodes were prepared by first mixing dry components of the composite in a mortar and pestle. Once sufficiently mixed n-methyl-2-pyrrolidone (NMP) solvent is

added to form a homogeneous slurry with a viscosity similar to oil. NMP is used as it can dissolve the PVDF. This slurry is then applied to the carbon cloth. Electrodes are then placed on a hot plate to evaporate the NMP solvent, leaving the composite electrode adhered to the carbon cloth. A schematic of the prepared electrode is shown in Figure 2.7. The carbon cloth pieces are weighed before application of the slurry and after drying to calculate the active material mass.

2.3.4 Voltammetry

Electrochemical techniques are the measurement of the response of an electrochemical cell to an applied electric input. As seen in Figure 2.5, an electrochemical cell consists of a series of electrodes immersed in or contacted to a common electrolyte. Standard electrodes being the working electrode, counter electrode and reference electrode.

Voltammetry is an electrochemical technique in which the current is measured as a function of applied potential.[139,140] There are many forms of voltammetry but the most common are potential sweep techniques in which the potential is swept at a constant rate from one potential to another, linear sweep voltammetry (LSV), or between two potentials, cyclic voltammetry (CV). These techniques are powerful as they obtain information regarding both thermodynamics and kinetics of a redox reaction. During CV as the potential is scanned positively above the reduction potential of a redox process species are oxidised and an anodic current is produced. The current increases to a peak and then decreases as the concentration of reduced species available for oxidation decreases, shown schematically in Figure 2.8a. E_{pa} is the potential at which the anodic current is the largest and i_{pa} is the magnitude of the peak anodic current. Then, the potential sweep is reversed. As the potential decreases below the reduction potential oxidised species are reduced, producing a cathodic current. Again, the current reaches a maximum and then decreases. E_{pc} is the potential at which the cathodic current is the largest and i_{pc} is the magnitude of the peak cathodic current.

This process is repeated. The average of E_{pa} and E_{pc} is the reduction potential of the material. A literature example of cycling voltammograms of nickel hexacyanoferrate is shown in Figure 2.8b.

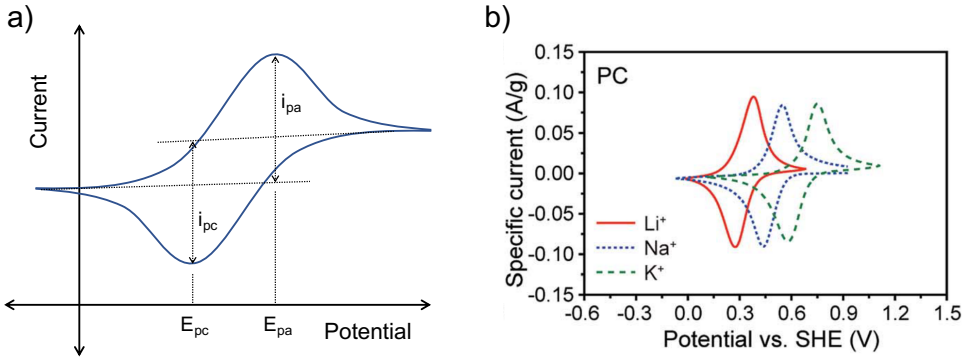


Figure 2.8: a) A schematic of a typical cyclic voltammogram. Labelled are the potential at peak anodic and cathodic currents, E_{pa} and E_{pc}, and the magnitude of peak anodic and cathodic currents, i_{pa} and i_{pc}. b) Cyclic voltammograms of nickel hexacyanoferrate in Li^+, Na^+ and K^+ containing PC-based electrolytes. Panel b) reproduced from ref[17] with permission from The Royal Society of Chemistry.

In this thesis, LSV measurements are used to study irreversible electrochemical reactions whereas CV measurements are used to study reversible electrochemical reactions. CV measurements of reversible electrochemical reactions for Prussian blue analogues can be used to calculate the reduction potential and kinetic parameters associated with an electrochemical process.

2.3.5 Galvanostatic cycling

Galvanostatic cycling is one of the most common electrochemical measurements performed on battery materials. It consists of applying a constant current and measuring the voltage. Once the voltage reaches a predetermined upper limit the current is reversed and the cell discharged until the cell reaches a predetermined lower limit. This process is repeated over many cycles. It is convention to plot specific capacity, charge passed normalised by the mass of active material in units of mAh/g, against voltage, an example is shown in Figure 2.9a. From these galvanostatic

charge/discharge profiles we can observe two voltage plateaus at 4.0 V and 4.1 V vs. K^+/K, the first cycle coulombic efficiency of around 72% and a reversible capacity of 128 mAh/g.

It is useful to plot the derivative of the capacity with respect to voltage, known as a dQ/dV plot, to highlight changes in slope of the galvanostatic cycling profile, see Figure 2.9b. Peaks in the dQ/dV plot correspond to electrochemical reactions. Depending on the nature of the electrochemical reaction the peaks can be sharp or broad. Single phase reactions take place over a range of potential and produce broad peaks in the dQ/dV plot, whilst two-phase reactions take place at a fixed potential and produce sharp peaks in the dQ/dV plot. There are two observable peaks in the dQ/dV plot on charge and discharge at around 4.0 V and 4.1 V vs. K^+/K.

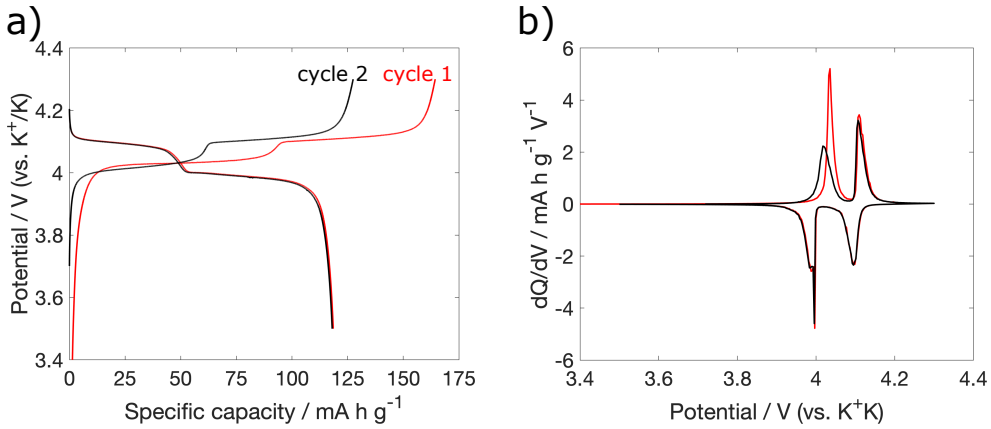


Figure 2.9: a) Galvanostatic cycling profile and b) differential capacity plot of potassium manganese hexacyanoferrate in a 1 mol dm^{-3} potassium bis(fluorosulfonyl)imide in N-Propyl-N-methylpyrrolidinium bis(fluorosulfonyl)imide electrolyte. Reprinted (adapted) with permission from ref[130]. Copyright © 2020 American Chemical Society.

2.3.6 Electrochemical impedance spectroscopy

Electrochemical impedance spectroscopy (EIS) is an electrochemical technique that measures the impedance of a system for a number of frequencies.[141] It is a powerful technique that can distinguish between different processes in an electrochemical system and has found a wide variety of uses.

An EIS measurement consists of applying a sinusoidal voltage (or current) to a system and measuring its current (or voltage) response for a number of frequencies. This is shown schematically for a single frequency in Figure 2.10. E_0 is the magnitude of the applied voltage, I_0 is the magnitude of the current response, and ϕ is the phase shift.

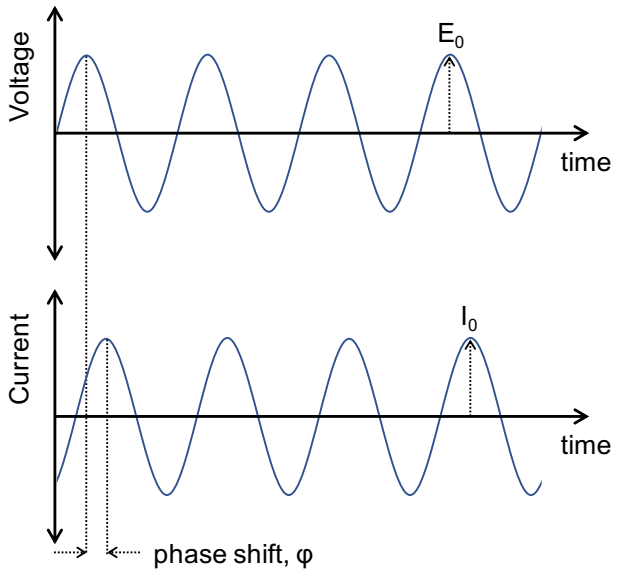


Figure 2.10: A schematic representation of the voltage signal and current response for a single frequency during an EIS experiment.

Since the relationship between radial frequency, ω, and frequency, f is

$$\omega = 2\pi f \tag{2.5}$$

the excitation voltage signal, E_t, and the response current signal, I_t, can be written as

$$E_t = E_0 sin(\omega t) \tag{2.6}$$

and

$$I_t = I_0 sin(\omega t + \phi) \tag{2.7}$$

The impedance, Z, is the complex version of resistance that contains both real and imaginary components. The impedance can be written as:

$$Z = \frac{E_t}{I_t} = \frac{E_0 sin(\omega t)}{I_0 sin(\omega t + \phi)} = Z_0 \frac{sin(\omega t)}{sin(\omega t + \phi)} \tag{2.8}$$

Given that Eulers relationship states that

$$exp(j\phi) = cos(\phi) + jsin(\phi) \tag{2.9}$$

it is possible to express the excitation voltage signal, E_t, and the response current signal, I_t, in complex forms:

$$E_t = E_0 exp(j\omega t) \tag{2.10}$$

and

$$I_t = I_0 exp(j\omega t - \phi) \tag{2.11}$$

From these expressions the impedance can be written in the following complex form:

$$Z(\omega) = \frac{E}{I} = Z_0 exp(j\phi) = Z_0(cos\phi + jsin\phi) \tag{2.12}$$

Data from EIS measurements is most commonly plotted as a Nyquist plot, in which the real part of the impedance is plotted on the x-axis and the imaginary component is plotted on the y-axis. Each data point is a measurement at a single frequency. An example of a Nyquist plot is shown in Figure 2.11a. Another popular presentation of

the impedance data is as a Bode plot which displays the frequency response of the system. In a Bode plot the frequency is plotted on the x-axis and either the absolute value of impedance, phase shift, or a different parameter is plotted on the y-axis. An example of a Bode plot with absolute value of impedance on the y-axis is shown in Figure 2.11b and with phase shift on the y-axis is shown in Figure 2.11c.

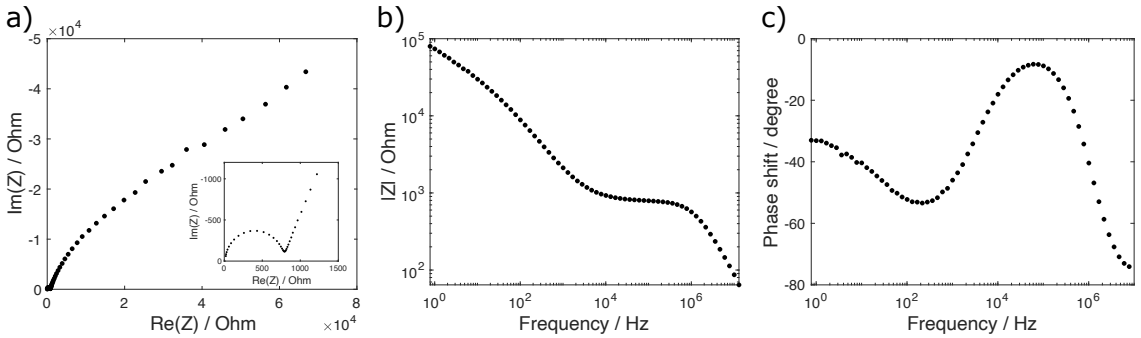


Figure 2.11: Impedance data for sodium zinc hexacyanoferrate taken in the frequency range 1 Hz to 13 MHz. a) Nyquist plot and the same data with reduced x and y axes is inset. b) and c) Bode plots with absolute value of impedance and phase shift on the y axes.

To interpret EIS data equivalent electric circuits must be made and parameters refined to closely reproduce the experimental data. Equivalent electric circuits are made up of simple elements such as resistors, R, capacitors, C, and inductors, L, that have defined impedance characteristics. For example, a resistor has an impedance of R (no imaginary component), whilst a capacitor has an impedance of $\frac{1}{j\omega C}$. Other elements often used in equivalent circuits to model electrochemical systems are Warburg elements, W, and constant phase elements, Q. Warburg elements are used to model low frequency diffusion processes in electrochemical cells. An 'infinite' Warburg element has the impedance of $\frac{1}{Y_0\sqrt{j\omega}}$, where Y_0 is a coefficient, and manifests as a 45° low frequency tail on the Nyquist plot. The 'infinite' Warburg element is only valid if the system has a diffusion layer that is effectively infinite, if this is not the case a modified 'finite' Warburg element can be used. In electrochemical systems interfaces do not behave like perfect capacitors and instead a constant phase element can be

used. A constant phase element has a impedance of $\frac{1}{Y_0(j\omega C)^\alpha}$. α is a tunable parameter which takes values between 0 and 1. For a perfect capacitor α would be equal to 1. A constant phase element can also be used as a 'nonideal' Warburg element; for an 'ideal' Warburg element α would be equal to 0.5. There are many system-specific cases where a 'nonideal' Warburg element would be necessary.

These individual elements are arranged in series and parallel to form equivalent circuits. To closely model the experimental data and extract useful information the choice and arrangement of elements must correspond to physical processes. For example, a Randles cell which models processes at an electrochemical interface, Figure 2.12, contains a resistor in series which corresponds to the solution resistance, R_s, and a capacitor and Warburg element in parallel with a second resistor corresponding to the double layer capacitance, C_{dl}, diffusion, W, and interfacial charge transfer, R_{ct}, respectively.

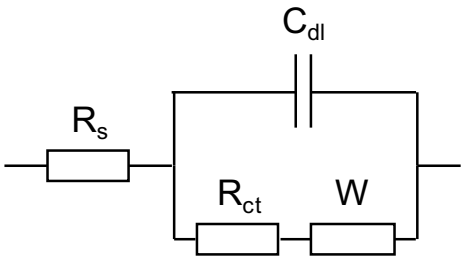


Figure 2.12: A Randles circuit.

Once an equivalent circuit has been constructed it is fitted to experimental data using a non-linear least squares fitting algorithm. In this algorithm all parameters have starting values and are changed one at a time. If the fit has been improved the new value is accepted before moving on to the next parameter. This process is iterated over all parameters many times until the fit is no longer improved. For a good equivalent circuit each element must correspond to a physical process and not simply added to improve the fit. The values of resistance, capacitance, and other parameters of the circuit elements can then be extracted and associated to physical phemonema.

Research into solid electrolytes rely on this technique to calculate the bulk ionic conductivity of materials by extracting the resistance of the resistor associated to bulk conductivity and knowing the geometry of the pellet.

2.4 Other techniques

2.4.1 Superconducting quantum interference device

Superconducting quantum interference devices (SQUIDs) are highly sensitive magnetometers. They consist a superconducting loop that contains two Josephson junctions in parallel.[108,142] A current, I, is passed through the loop and when there is no magnetic field the current is split equally between the two parallel branches. In such as system the allowed magnetic flux values through the loop is quantised. If the applied magnetic field is not an integer multiple of the magnetic flux quantum, Φ_0, then a small screening current, I_S, is produced within the loop which affects the measured voltage. As the applied magnetic field increases the measured voltage oscillates. From these oscillations it is possible to calculate the applied field. A schematic of the working principles of SQUID magnetometers is shown in Figure 2.13.

In this thesis only basic magnetometry measurements are presented, which have been previously discussed in Section 1.4.2. Firstly, field-cooled magnetometry measurements in which the sample is cooled to low temperatures, typically 5 K, under an external magnetic field. Then, the sample is slowly heated, still under the external field, and the induced magnetic moment recorded as a function of temperature. The nature of the magnetic behaviour can be studied as well as the magnetic ordering temperature. The second measurement type presented is the hysteresis loop. At low temperature, 5 K, the external magnetic field is swept from zero to a high applied field and then back through zero to high applied field in the reverse direction. The induced magnetic moment is recorded as a function of applied field. From the hysteresis loop

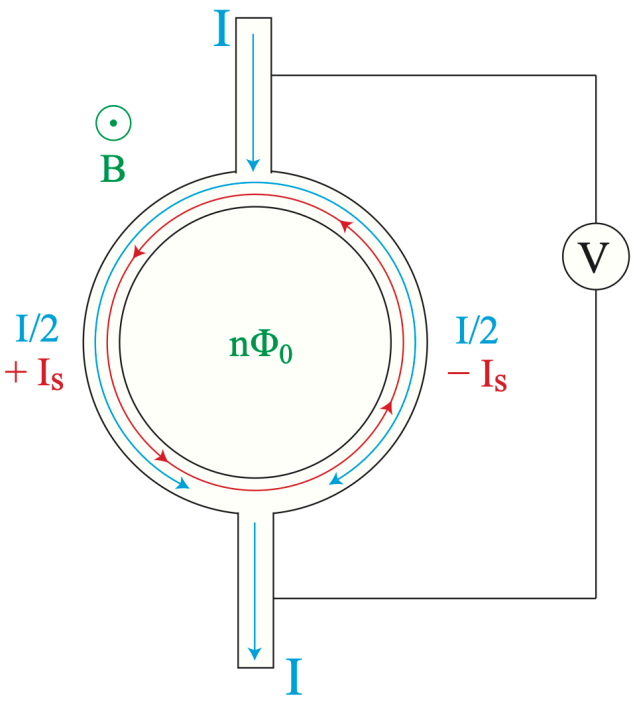


Figure 2.13: A schematic representation of a SQUID magnetometer. Reproduced from ref[108].

a number of magnetic properties can be derived including saturation magnetisation, remnant magnetisation and the coercive field. These measurements were conducted in a SQUID magnetometer.

Chapter 3

Structural and electrochemical properties of manganese hexacyanochromate

3.1 Abstract 63
3.2 Introduction 64
3.3 Experimental methods 65
3.4 Results and discussion 68
3.4.1 Physiochemical characterisation of as-synthesised manganese hexacyanochromate 68
3.4.2 Characterisation of water and thermal stability 73
3.4.3 Electrochemical characterisation of manganese hexacyanochromate 76
3.5 Conclusions 82

3.1 Abstract

Prussian blue analogues (PBAs) are some of the most promising sodium- and potassium-ion cathode materials as they exhibit reasonable specific capacities (up to 150 mAh/g), and excellent rate performance and cycle life. However, to fully utilise these excellent properties in a full cell an anode material of similarly good performance is required. This motivates research for PBA compositions that operate at low potentials and function as anode materials. However, the current state of the art have reasonably high reduction potentials and low specific capacities, or are structurally unstable. In this chapter the low potential structural and electrochemical behaviour of manganese hexacyanochromate is investigated. It shows reversible sodium insertion at −0.86 V

vs. SHE which is the lowest reported to date. Ex situ XRD and FTIR confirm the open-framework structure is maintained and charge storage is through reversible sodium insertion. Further reduction in potential in an organic electrolyte resulted in loss of the structure and reversible capacity arising from undesirable conversion-type mechanisms.

3.2 Introduction

Most of the literature on Prussian blue analogue materials for battery electrodes is focussed on hexacyanoferrate-based compounds. These materials have Fe in the R site, which changes its oxidation state between III and II at around 0.80 V vs. SHE, depending on the P site transition metal, making them ideal cathode materials in both aqueous and organic electrolytes.[15,61,62,86,89,143] These compounds are relatively well studied and they show excellent performance, particularly in terms of cycle life and rate capability. Their excellent electrochemical properties are associated to their open-framework structure that exhibits minimal modification on electrochemical cycling and allows facile movement on alkali cation species.[13] However, to utilise their excellent properties in a full cell an anode of comparable performance is required. This drives research to develop PBA materials that operate at lower potential.

Dostal and Scholz produced seminal work in characterising the electrochemical properties of a wide compositional range of PBA materials.[28] This work provides a basis for substituting the transition metals to lower the reduction potential of the PBA. This strategy was successfully utilised in the synthesis, characterisation and use of manganese hexacyanomanganate (MnHCMn).[72] MnHCMn has a redox couple at 0 V vs. SHE, $Mn^{II}[Mn^{III/II}(CN)_6]$. This material was used in conjunction with copper hexacyanoferrate as the cathode to produce a full cell with an average discharge voltage of 1 V, negligible capacity fade over 1000 cycles and high-rate capability.

MnHCMn also has an active redox couple at a lower potential of −0.7 V vs. SHE, $Mn^{II}[Mn^{II/I}(CN)_6]$.[17] Using a co-solvent electrolyte (water:acetonitrile) a full cell was produced with copper hexacyanoferrate as the cathode that had an average discharge voltage of 1.55 V and exhibited good electrochemical performance.[73] There have also been attempts to develop PBA materials that operate at even lower potentials.[144–146] These reports have shown that the open-framework structure breaks down at low potentials and unexpectedly high reversible capacity arises from conversion-type mechanisms.

The objective of this chapter is to investigate PBA materials that have reduction potentials lower than the transition metal hexacyanomanganate compounds. Due to the lower reduction potential of the parent complex, $Cr(CN)_6^{3-/4-}$, PBAs based on this complex, transition metal hexacyanochromates, have low reduction potentials themselves and warrant investigation. As a model compound manganese hexacyanochromate, with Mn^{2+} in the P site, is the most appropriate starting point. Occupying the low crystal field splitting P site, Mn^{2+} is high spin and has the electronic configuration $t_{2g}^3\ e_g^2$. This results in Mn^{2+} taking non-distorted octahedral symmetry and being highly stable against reduction or oxidation. In this chapter the structure and electrochemical properties of manganese hexacyanochromate will be studied with particular focus on the role water plays and structural stability at low potential. Figure 3.1 shows a schematic of the manganese hexacyanochromate crystal structure.

3.3 Experimental methods

Manganese hexacyanochromate was synthesised through a reaction between equal volumes of aqueous solutions of $MnCl_2$ and $K_3Cr(CN)_6$. Both solutions were 1 M NaCl. Typically, a 60 mM $MnCl_2$ solution was added in a dropwise manner to 60 mM $K_3Cr(CN)_6$ solution under vigorous stirring. After a few drops the solution began

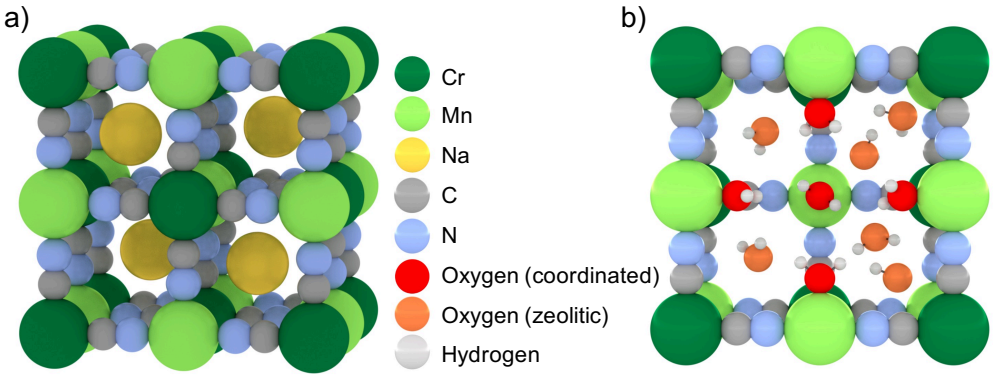


Figure 3.1: A schematic of the manganese hexacyanochromate crystal structure a) with zero vacancies and half of the interstitial sites filled and b) with a hexacyanochromate vacancy including the positions of water molecules in the structure. Reprinted (adapted) with permission from ref[123]. Copyright © 2013 American Chemical Society.

to turn cloudy indicating the precipitation reaction has occurred. After addition of all of the $K_3Cr(CN)_6$ solution the reaction was left to stir for 30 to 60 minutes. The precipitate was centrifuged, washed with deionized water three times and once with acetronitrile, and dried overnight in air at 80 °C. The dried product was ground in a mortar and pestle to a fine powder and stored for characterisation. Manganese hexacyanoferrate was synthesised in a similar manner apart from $K_3Cr(CN)_6$ was substituted for $Na_4Fe(CN)_6$.

Elemental composition was determined by inductively coupled plasma optical emission spectroscopy (ICP-OES). Thermal analysis was performed using simultaneous thermogravimetric analysis mass spectrometry (TGA-MS). Microscopy was performed on a field emission gun scanning electron microscope (FEG-SEM) that had electron dispersive X-ray spectroscopy (EDS) capability. X-ray diffraction was performed on both lab instruments (both standard and inside a glovebox with an N_2 atmosphere) and using a synchrotron X-ray source (Diamond light source beamline I11 using the position sensitive detector). Fourier transform infrared spectroscopy (FTIR) was performed inside a N_2-filled glovebox using both an attenuated total reflection (ATR) stage and in transmission using a CsI pellet. Particle size distribution was measured

using dynamic light scattering (DLS) using a He-Ne laser with a wavelength of 633 nm.

Electrodes were prepared using a mixture of active material, carbon additive, and poly(vinylidene fluoride) (PVDF) binder in a mass ratio of 8:1:1. Dry precursors were mixed in a morter and pestle with 1-methyl-2-pyrrolidone (NMP) to form a slurry. The slurry was prepared reasonably viscous and pasted on carbon cloth with areal loadings of 4 - 10 $\mathrm{mg\,cm^{-2}}$ and dried overnight in air at 80 °C. Electrochemical measurements were performed in a three-electrode flooded cell in an Ar-filled glove box (Figure 2.5). For aqueous measurements a 37 $\mathrm{mol\,dm^{-3}}$ sodium bis(fluorosulfonyl)imide (NaFSI) electrolyte was used with a manganese hexacyanoferrate counter electrode and Ag/AgCl pseudoreference electrode. For nonaqueous measurements a 1 M sodium perchlorate ($NaClO_4$) in propylene carbonate (PC) electrolyte was used with sodium metal as both counter and reference electrodes. Ag/AgCl pseudoreference electrodes were prepared by electrochemically driving oxidisation of silver wire in a HCl solution and calibrated using ferrocene as an internal standard. Electrochemical measurements were performed using a BioLogic VMP3 potentiostat.

Galvanostatic cycling experiments were stopped after specified amounts of charge had passed, and electrodes retrieved for ex situ analysis. The electrodes were washed three times with acetonitrile to remove the electrolyte and dried. XRD measurements were made directly on the electrode itself. For FTIR measurements the composite was scraped from the carbon cloth current collector for analysis.

3.4 Results and discussion

3.4.1 Physiochemical characterisation of as-synthesised manganese hexacyanochromate

An SEM micrograph and particle size distribution of as-synthesised manganese hexacyanochromate (MnHCCr) are shown in Figure 3.2. The particles are large and cubic with edge lengths of approximately 1.5 µm, or hydrodynamic diameter of around 2.5 µm. There appears to be a very low fraction of particles with a hydrodynamic diameter of less than 1.5 µm. EDX analysis, Figure 3.3, shows a uniform distribution of Mn, Cr, N, C over a single MnHCCr particle, as expected.

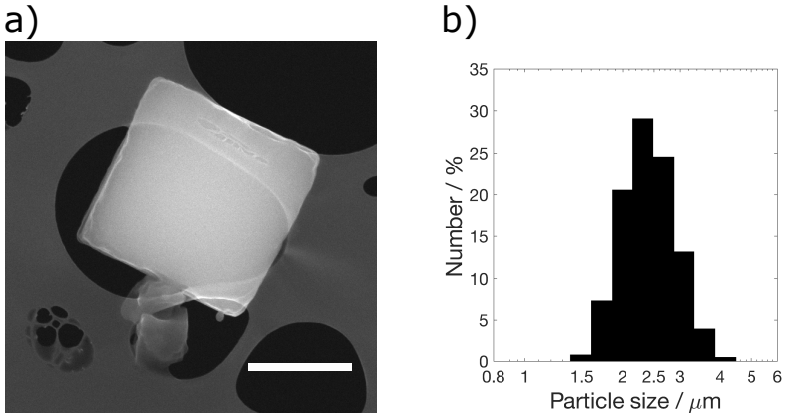


Figure 3.2: a) Scanning electron micrograph of as-synthesised MnHCCr, scale bar 1 µm. b) Particle size distribution of MnHCCr, showing a unimodal distribution centred at around 2.3 µm. Note that this data was taken using dynamic light scattering which produces a hydrodynamic particle diameters. The average cube side length is approximately, 1.5 µm. Reprinted (adapted) with permission from ref[123]. Copyright © 2013 American Chemical Society.

The large particle size of manganese hexacyanochromate is somewhat unusual given the synthesis route. Typically, PBAs made under the same conditions are formed with particle sizes less than 100 nm, and measures have to be introduced to increase the particle size.[61,62] Typically, as the two precursor solutions are mixed there is an instantaneous reaction and many small particles are formed. From a nucleation and

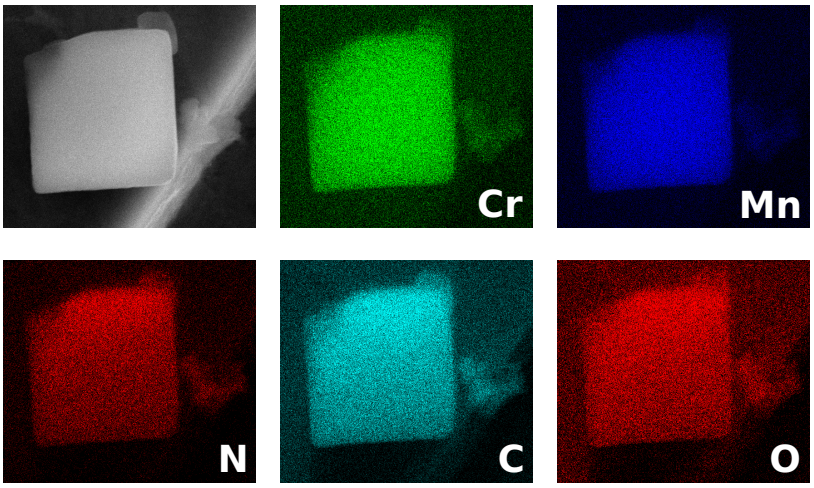


Figure 3.3: Energy-dispersive X-ray (EDX) spectroscopy of a single MnHCCr particle showing an even distribution of elements. Reprinted (adapted) with permission from ref[123]. Copyright © 2013 American Chemical Society.

growth viewpoint the critical nuclei radius is small leading to very fast nucleation of many particles and those particles growing only a small amount. To overcome this, specific synthesis strategies have been developed to alter this process to produce larger particles such as adding a chelating agent[77,87] or using a single transition metal source which ensures a very low concentration of the second reactant.[82,86]

The synthesis of manganese hexacyanochromate, in contrast, produces very large particles using the conventional method. The crucial difference is observed during the synthesis. On the first addition of the $MnCl_2$ solution there is no immediate precipitation. It is only after a few more drops that precipitation occurs. This suggests there is a larger critical nuclei radius for the precipitation of manganese hexacyanochromate, requiring a larger concentration of precursors in solution to initiate the reaction. Once particles are nucleated and start to grow there is insufficient concentration of the reactants for subsequent nucleation to occur. These observations can be explained through classical nucleation theory (CNT), which explains the thermodynamics, and LaMer nucleation theory, which considers the kinetics.[114] Schematics of these two theories are shown in Figure 3.4.

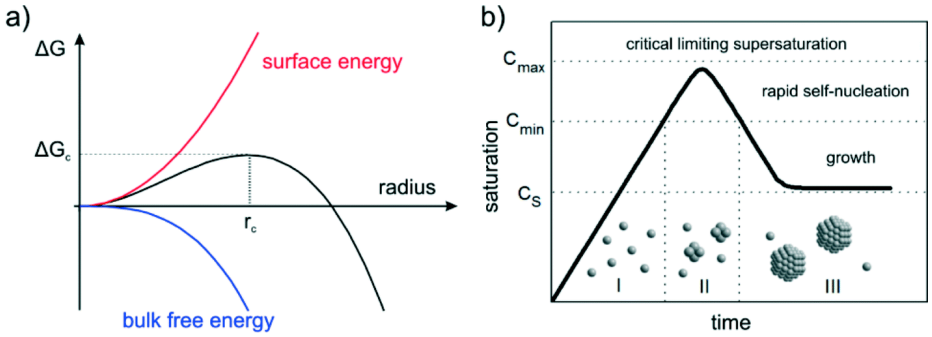


Figure 3.4: a) A schematic representation of how volumetric Gibbs energy of reaction and surface energy terms result in a critical nuclei radius and activation energy for homogenous nucleation. b) The LaMer model of nucleation. Reproduced from ref[147] with permission from the Royal Society of Chemistry.

First taking the thermodynamics; the critical nuclei radius for homogeneous nucleation is governed by the Gibbs energy per volume and surface energy terms. The Gibbs energy per volume is a negative energy which scales with the volume of the particle, with r^3. The surface energy is positive and scales with the surface area, with r^2. This creates a critical nuclei radius which if a particle is smaller it will dissolve, and if it is bigger it will grow. The larger critical nuclei radius of manganese hexacyanochromate compared to other PBA compositions suggests that either the Gibbs energy per volume is lower or the surface energy is higher.

The kinetics of the nucleation step of PBAs is adequately described by LaMer's nucleation theory.[114,147] The model begins with the slow increasing of the concentration of the critical reagent. In the case of PBA synthesis this will be the transition metal salt. At a critical supersaturation concentration homogeneous nucleation is thermodynamically possible but prevented due to the activation energy barrier. As the concentration continues to increase the energy barrier for nucleation is overcome and there is rapid burst nucleation. After this process the concentration is reduced considerably, preventing additional nucleation, and existing particles grow in a diffusion limited regime and the concentration is stabilised. This theory explains differences seen in the PBA nucleation and growth. For compositions that nucleate very quickly

the concentration for nucleation is small, as is the critical nuclei radius. However, for manganese hexacyanochromate due to the differences in the thermodynamics the critical nuclei radius is larger and the concentration for nucleation is larger. For manganese hexacyanochromate once the burst nucleation step occurs the concentration of the reagent stays below the critical supersaturation level. This means there is a single nucleation period after which particles grow.

The molecular formula of manganese hexacyanochromate is derived from the ratio between elements from ICP data, ICP results presented in Table 3.4.1. The molecular formula is calculated to be $Na_{0.04}Mn[Cr(CN)_6]_{0.70}$, which gives a vacancy content of 30%. This is consistent with results from other PBA compositions synthesised in a similar manner and in the oxidation state $P^{II}R^{III}$. For battery materials it is preferable to reduced the vacancy content, to increase the specific capacity. This is typically accomplished by synthesising the material in the reduced state and increasing the alkali metal concentration in solution. However, it is inherent when synthesising PBA materials with low reduction potentials that the precursors and the synthesised PBA are not stable against oxidation in water. To put is simply $Fe(CN)_6^{4-}$ is stable in water whereas $Cr(CN)_6^{4-}$ is not. This prevents synthesis in water in the reduced state. Additional experiments found that increasing the concentration of NaCl in solution during synthesis had no appreciable effect on the composition.

Element	Normalised concentration / no units
Mn	1
Cr	0.70
Na	0.04

Table 3.1: Inductively coupled plasma - optical emission spectroscopy (ICP-OES) results for as-synthesised MnHCCr. The material has a hexacyanochromate vacancy content of 30%.

High-resolution synchrotron XRD was used to characterise the crystal structure of manganese hexacyanochromate. The XRD pattern, Reitveld fitting and residual are shown in Figure 3.5.

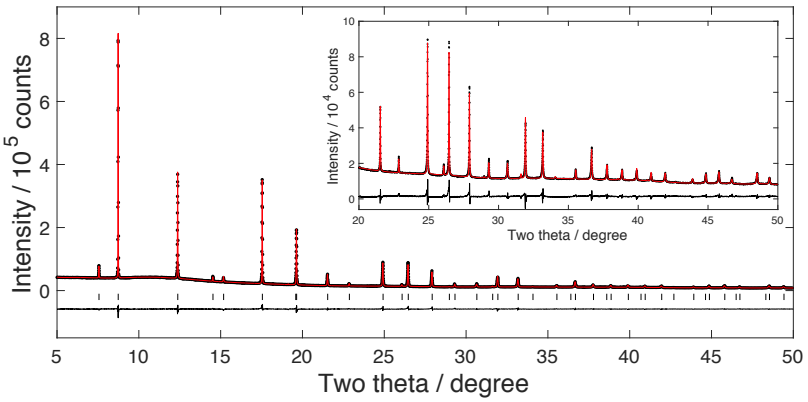


Figure 3.5: High-resolution synchrotron X-ray diffraction pattern of as-synthesised MnHCCr with Rietveld refinement fit and residual. Reprinted (adapted) with permission from ref[123]. Copyright © 2013 American Chemical Society.

Prussian blue analogues typically crystallise in the space group *Fm-3m*, which is indeed what MnHCCr takes.[148] Mn and Cr take 4a and 4b sites respectively, whereas C and N take 24e sites (x, 0, 0). Water is present in the structure in two distinct binding environments: coordinated water bonded to Mn in vacancies and zeolitic water distributed loosely bound throughout the structure.[8,148] Hexacyanochromate vacancies are randomly distributed which is modelled in the Rietveld refinement as fixed fractional occupancy on the Cr, C, and N sites.

The refinement model was taken from Ludi *et al.*[148] Within the model sodium was omitted as it had very low occupancy, of 0.04 from ICP. Also, water within the structure was treated as only oxygen atoms as hydrogen has extremely low scattering.[50,134]

The refinement parameters are reported in Table 3.4.1. The lattice parameter was calculated to be 10.804 Å, which is within the range of previously reported values.[148–150] The range in these values arise primarily from the sensitively of the lattice parameter to water content (atmospheric humidity) but also from adjustable parameters such as vacancy content. The refined vacancy content of 31% was in good agreement with the result of ICP, of 30%. The occupancies of the two oxygen positions are reasonable. Coordinated water had an occupancy value of 0.41, which is reasonably

close to the expected value of 0.30. The zeolitic water had an occupancy value of 1.42 but also a large atomic displacement parameter of 0.40 $Å^2$. This is unreasonably high and indicative of inaccuracies in the model. In MnHCCr the vacancy content is high and the lack of vacancy order results in a number of local environments. Each interstitial site could have zero, one, two, three or four hexacyanochromate vacancies, a principle described in more detail elsewhere.[134] This results in a number of off-centre oxygen sites. Additionally, water is not a centrosymmetric molecule and there is considerable hydrogen bonding between coordinated and zeolitic water within intersties.[8,148] Because of all of these factors the location of water molecules is complex and somewhat irregular. Efforts to further refine the positions of O(1) oxygen atoms, more specifically than the 8c site, proved unsuccessful.

Atom	Site	g	x	y	z	U_{iso} / $Å^2$
Mn	4a	1	0	0	0	0.02822(21)
Cr	4b	0.6931(6)	0.5	0	0	0.02259(30)
O(1)	8c	1.4218(29)	0.25	0.25	0.25	0.4025(16)
C	24e	0.6931(6)	0.30836(20)	0	0	0.0649(13)
N	24e	0.6931(6)	0.20041(15)	0	0	0.0344(8)
O(2)	24e	0.4124(18)	0.2449(4)	0	0	0.1908(18)

Table 3.2: Structural parameters of MnHCCr from Rietveld refinement in the space group Fm-3m (Z = 4). Occupancy g, atomic positions (x, y, z), and isotropic atomic displacement U_{iso} are given. The X-ray wavelength was $\lambda = 0.824\,53$ Å. The lattice parameter was calculated to be 10.803 920(13) Å. Oxygen takes two positions, O(1) bonded to Mn in vacancies and O(2) at the centre of the interstitial site. $R_P = 1.65\%$, $R_{WP} = 2.79\%$, $\chi^2 = 16.26$, GOF = 4.03.

3.4.2 Characterisation of water and thermal stability

Water within the structure is important to the electrochemical behaviour and stability in PBA materials. Here the role of water is studied by selectively removing different types of water from the structure. Additionally, it is important to be able to control the water content of MnHCCr for electrochemical testing. In order to do this thermal analysis was performed consisting of simultaneous thermal analysis - mass spectrometry.

The results are shown in Figure 3.6.

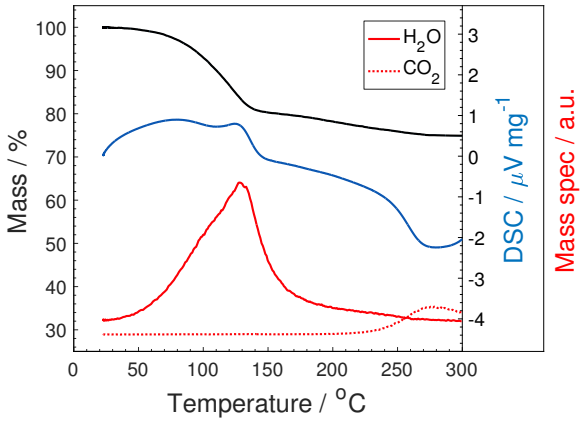


Figure 3.6: Thermal analysis of MnHCCr. Thermogravimetric analysis shows two distinct mass loss events with corresponding differential scanning calorimetry and mass spectrometry traces. Reprinted (adapted) with permission from ref[123]. Copyright © 2013 American Chemical Society.

The mass loss trace shows two distinct mass loss steps. These are between room temperature (RT) and 150 °C, and between 150 °C and 280 °C. The first mass loss step is ≈20% and the second is ≈5%. From the mass spectrometry data it can be seen that water loss is the most significant contributing factor to the mass loss. Based on the mass loss due to water the number of water molecules per formula unit can be calculated to be 2.8, giving the molecular formula as $Na_{0.04}Mn[Cr(CN)_6]_{0.70} \cdot 2.8\,H_2O$. Within this first step two distinguishable water loss steps can be seen, most evidently in the DSC trace. These are thought to be from zeolitic water initially, and then from coordinated water at higher temperature.[151] The nature of the second mass loss step is uncertain. Carbon dioxide release at high temperature signalling breakdown of the structure.

To study manganese hexacyanochromate at different levels of hydration four samples were prepared by drying at RT, 80 °C, 150 °C, and 220 °C under vacuum. The XRD patterns and FTIR spectra of these samples are shown in Figure 3.7. The most intense peak and characteristic CN stretch absorption band of CN is at 2164 cm^{-1} for the RT sample, increasing to 2166 cm^{-1} then 2170 cm^{-1} as water is removed.[10]

The broad band between 3100 and 3700 cm^{-1} and the sharp peaks at 3604 cm^{-1} and 3650 cm^{-1} are stretching modes of water in the sample. The broad band reduces in intensity once the material is dried at 80 °C under vacuum. There are two sharp absorption bands at 1616 cm^{-1} and 1678 cm^{-1} that correspond to bending modes of water. Dehydration at 80 °C results in a reduction in intensity of the peak at 1616 cm^{-1} whereas the peak at 1678 cm^{-1} does not change. This suggests that the peak at 1616 cm^{-1} is from the zeolitic water and the peak at 1678 cm^{-1} is from the coordinated water.[135] Peaks in the FTIR spectra between 2260 cm^{-1} and 2320 cm^{-1} and at 2945 cm^{-1} are from acetonitrile impurities introduced during the washing procedure.

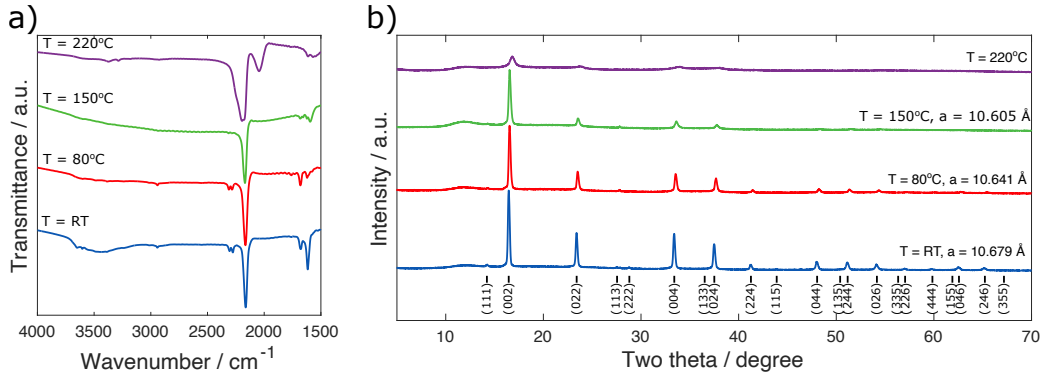


Figure 3.7: X-ray diffraction patterns and Fourier-transform infrared spectra of MnHCCr samples dried at room temperature, 80 °C, 150 °C, and 220 °C under vacuum. Reprinted (adapted) with permission from ref[123]. Copyright © 2013 American Chemical Society.

XRD patterns shows a decrease in lattice parameter of the material as it is dehydrated. From RT to 80 °C to 150 °C the lattice parameter decreases from 10.679 Å to 10.641 Å to 10.605 Å. Additionally, as the material is dehydrated there is a decrease in the relative intensity of high angle reflections, which is likely caused by reducing the zeolitic water content which reduces the structure factor of higher angle planes. Zeolitic water occupying the 8c interstitial sites modifies the relative peak highs in the same manner as alkali cations. There is a significant decrease in the intensity of XRD peaks as well as an increase in the full-width half-maximum for the sample dried

at 220 °C under vacuum. FTIR data shows the v(CN) absorption band is broadened and shifted to higher wavenumbers whilst a new peak emerged at lower wavenumbers. Combining the XRD and FTIR data it appears on full dehydration the material loses almost all long range order, there is significant loss of symmetry, and changes to the local bonding environment.

3.4.3 Electrochemical characterisation of manganese hexacyanochromate

Typically PBA materials with high vacancy content perform best when in an aqueous electrolyte as they have to be dehydrated to operate well in a non-aqueous electrolyte. Previous reports have shown PBA materials in aqueous electrolytes have very fast electrode kinetics and long cycle lives.[61,72] This is due to very low interfacial charge transfer, as alkali cations undergo only partial dehydration when inserting into the lattice, and high ionic mobility within the structure, as water shields local charges.[152] Density functional theory has shown a stabilising effect of structural water.[153]

Since manganese hexacyanochromate has a high vacancy and water content it was first explored in a water-based electrolyte. However, because the material has such a low reduction potential, much lower than the reductive stability limit of water, conventional aqueous electrolyte could not be used. Instead a high-voltage 'water-in-salt' (WiS) electrolyte was employed. The electrolyte was 37 m NaFSI (sodium bis(fluorosulfonyl)imide) solution prepared at the solubility limit. This is an example of a highly concentrated electrolyte which have attracted much research attention and has significant development in recent years.[80,154] Their primary benefit is that the electrochemical stability window of the electrolyte is enhanced, compared to the solvent, at high concentrations. Locally the solvent molecules are primarily bonded to salt ions which increase their stability and reduce their activity. Characterisation of the electrochemical stability window of the electrolyte was carried out by performing

linear sweep voltammetry (LSV) at $1\,\mathrm{mV\,s^{-1}}$ using both glassy carbon (GC) and platinum (Pt) electrodes, shown in Figure 3.8.

There are no standardised values of potential scan rate and current density limit to use when measuring the electrochemical stability window of an electrolyte. The values used here, $1\,\mathrm{mV\,s^{-1}}$ and $10\,\mu\mathrm{A\,cm^{-2}}$, are conservative values and results in a conservative electrochemical stability window. As seen in Figure 3.8 there are significant differences between glassy carbon and platinium which arise from surface layers that form on the electrodes and electrocatalytic effects. The electrochemical stability window when using glassy carbon was measured to be $-1.08\,\mathrm{V}$ to $1.20\,\mathrm{V}$ and when using platinum was measured to be $-0.77\,\mathrm{V}$ to $1.59\,\mathrm{V}$.

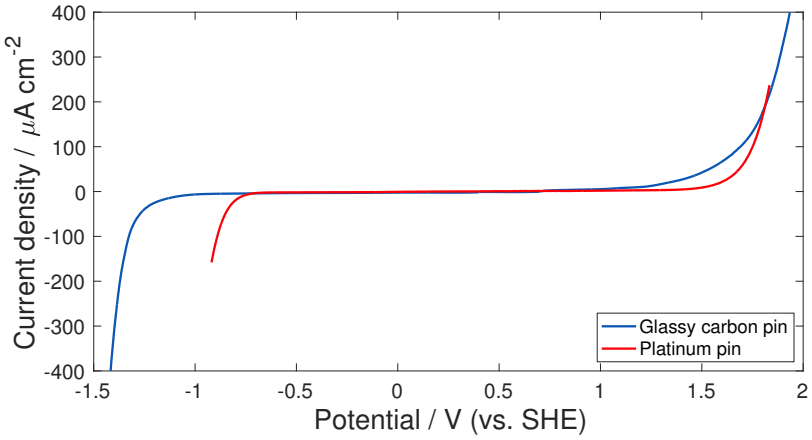


Figure 3.8: Linear sweep voltammetry of the WiS electrolyte taken using glassy carbon (GC) and platinum electrodes at a scan rate of $1\,\mathrm{mV\,s^{-1}}$.

Figure 3.9 shows the differential capacity (dQ/dV) plot of MnHCCr, alongside the dQ/dV of MnHCFe. The LSV traces are plotted for comparison. The reversible electrochemical reaction of manganese hexacyanochromate is centered at $-0.86\,\mathrm{V}$ vs. SHE. The reversible capacity is $62\,\mathrm{mA\,h\,g^{-1}}$ at a current density of $15\,\mathrm{mA\,g^{-1}}$. Although this capacity appears low it is expected for a PBA material where only the R site is electrochemically active and the material contains 30% vacancies.

To study the electrode reaction kinetics cyclic voltammograms of MnHCCr were taken at a series of scan rates, shown in Figure 3.10. As the scan rate increased the

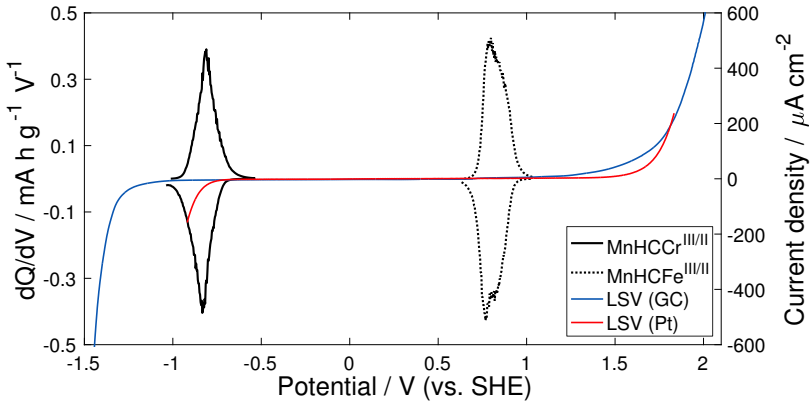


Figure 3.9: dQ/dV plots of MnHCCr and MnHCFe using a current density of 15 mA g^{-1}. MnHCCr has a redox potential of −0.86 V vs. SHE. The LSV plots of the electrolyte are included to show the electrochemical stability window of the electrolyte. Reprinted (adapted) with permission from ref[123]. Copyright © 2013 American Chemical Society.

peak separation increased and the peak current density increased. Plotting the square root of the scan rate against peak current gives a linear relationship which indicates the reaction is quasi-reversible and diffusion limited. The diffusion coefficient can be calculated through the following relationship between peak current, i_{peak}, and scan rate.[139]

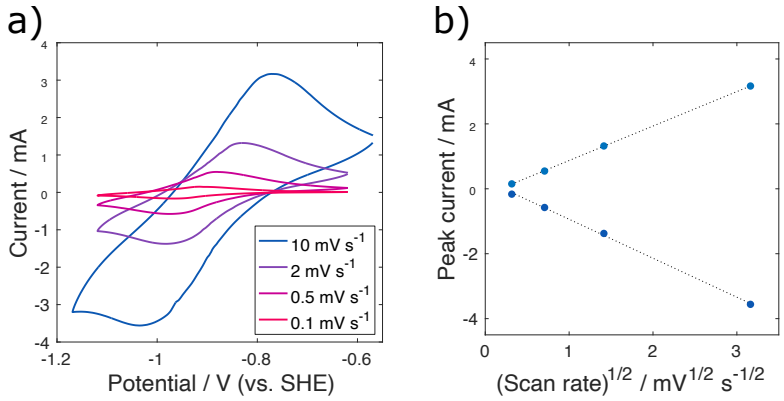


Figure 3.10: a) Cyclic voltammograms of MnHCCr in the WiS electrolyte with scan rates between 0.1 mV s^{-1} to 10 mV s^{-1}. (b) The peak current at each scan rate plotted against the square root of the scan rate. The gradients of the lines of best fit are 1.07 mA $s^{1/2}$ $V^{-1/2}$ and −1.20 mA $s^{1/2}$ $V^{-1/2}$. Reprinted (adapted) with permission from ref[123]. Copyright © 2013 American Chemical Society.

$$i_{peak} = 0.4463 \cdot \sqrt{\frac{n^3 F^3}{RT}} \cdot \sqrt{D} \cdot C_o \cdot \sqrt{V_{rate}}$$

Where n is the number of electrons involved in the reaction, D ($\mathrm{cm\,s^{-1}}$) is the average diffusion coefficient, $\mathrm{C_0}$ ($\mathrm{mol\,cm^{-3}}$) is the concentration of active sites, $\mathrm{V_{rate}}$ ($\mathrm{mV\,s^{-1}}$) is the scan rate and F, R, and T take their conventional meanings. $\mathrm{C_0}$ can be estimated from the specific capacity and density of the material. Using the gradient of the line of best fit during oxidation of $1.07\,\mathrm{mA\,s^{1/2}\,V^{-1/2}}$ gives an average diffusion coefficient of $1.9 \times 10^{-6}\,\mathrm{cm^2\,s^{-1}}$. This value is high for solid state diffusion but similar in order of magnitude to diffusion in other PBA compounds.[17]

The electrode reaction and charge storage mechanism was studied by ex situ XRD and FTIR spectroscopy. Samples were prepared by cycling electrodes twice and on the third discharge stopping at various charge states between 0 (fully oxidised) and 1 (fully reduced). The XRD patterns, Figure 3.11a, show that the structure remains cubic with a slight change in lattice parameter. The (2 2 0) reflection, Figure 3.11b, shows a slight increase to higher two theta values as the material is reduced. This peak was used to illustrate the change in lattice parameter as it is of significant intensity and at high angle leading to a larger shifts in peak position. The lattice parameters of a cubic cell is refined and plotted in Figure 3.11c. The material exhibits a linear change in lattice parameter and an overall change of less than 1%. As the material is reduced and sodium enters the material and the lattice parameter decreases. This unexpected behaviour is because the $\mathrm{Cr(CN)_6^{n-}}$ complex radius decreases as it is reduced, with a minimal direct effect on lattice parameter from the insertion ion.[69,155] A change in relative peak intensities can be observed as the sodium content in the material increases.

Ex situ FTIR spectra can be used to study changes in bonding in the material. The strong v(CN) absorption band between $1900\,\mathrm{cm^{-1}}$ and $2200\,\mathrm{cm^{-1}}$ has been used in literature to probe the oxidation state of the transition metals in PBA materials.[72,133,134]

The position of this band is dependent on both the transition metal species and their oxidation states. The peak at 2164 cm^{-1} is characteristic of $Mn^{II}-N\equiv C-Cr^{III}$ bonding and the peak 2049 cm^{-1} is characteristic of $Mn^{II}-N\equiv C-Cr^{II}$ bonding. Figure 3.11e shows that as the material is oxidised the intensity of the band at 2164 cm^{-1} decreases and the intensity of the band at 2049 cm^{-1} increases. Figure 3.11f shows the points in the discharge curve at which electrodes were discharged to.

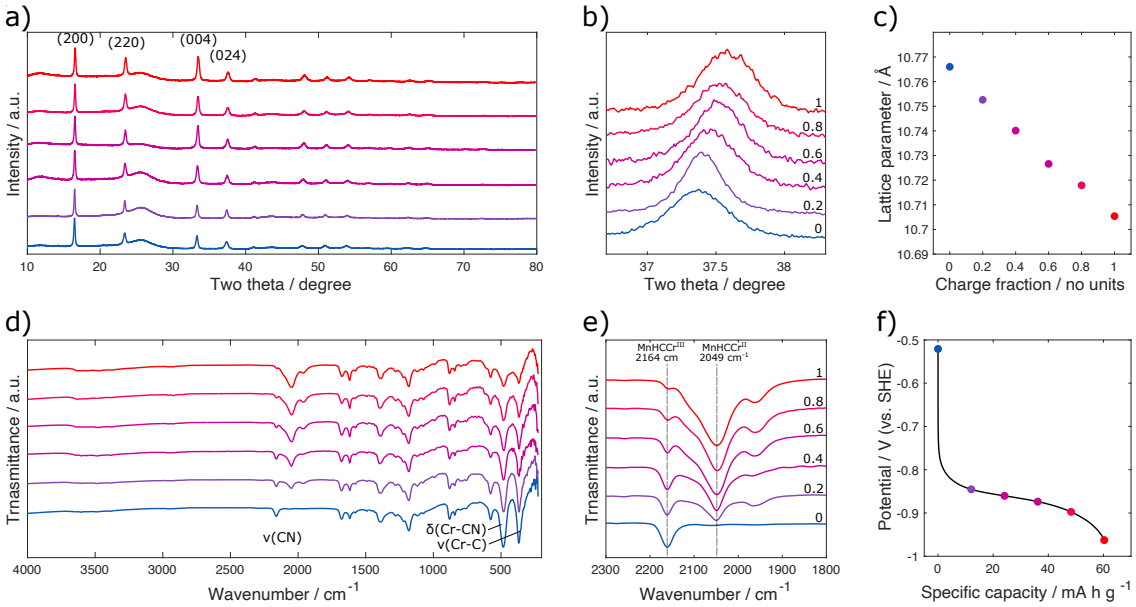


Figure 3.11: Ex situ XRD patterns and FTIR spectra were taken on MnHCCr electrodes at a series of charge states between 0 (fully oxidised) and 1 (fully reduced). a) and b) show the XRD patterns. The unit cell lattice parameter of the samples and plotted against charge state in c). d) and e) show the FTIR spectra of the samples. f) Shows a characteristic discharge curve and the points at which electrodes were discharged to. Major XRD reflections and FTIR absorption peaks are assigned. Reprinted (adapted) with permission from ref[123]. Copyright © 2013 American Chemical Society.

Ex situ analysis confirms that the structure is maintained and charge storage is from sodium insertion and transition metal redox. To explore the stability of the material at even lower potential, lower than limit of stability of the WiS electrolyte, an organic electrolyte (1 M $NaClO_4$ in PC) was used.

Prior to measurement in the organic electrolyte the electrodes were dried at 150 °C under vacuum to remove water from the material. It was important to remove the

water as at low potential, without the stabilising effect the high salt concentration, water would be reduced which produces hydroxide ions. Hydroxide ions are known to exchange with the cyanide ligands, causing dissolution of the material, which is why PBAs generally are less stable in neutral and basic pH conditions.[156]

MnHCCr electrodes were cycled to two cut-off voltages; $-1.30\,\mathrm{V}$ vs. SHE and $-1.65\,\mathrm{V}$ vs. SHE. The electrodes were cycled twice at $15\,\mathrm{mA\,g^{-1}}$ and ex situ XRD patterns taken in the pristine state, after the first discharge, and after the first full cycle. The equivalent plot for MnHCCr cycled in WiS is also shown, Figure 3.12.

Figures 3.12a and b show the galvanostatic profile and corresponding XRD patterns of MnHCCr operated in the WiS electrolyte. Operating in the organic electrolyte with a voltage cut-off of $-1.30\,\mathrm{V}$ vs. SHE MnHCCr shows the same single reversible redox couple corresponding to the reduction of chromium and the maintenance of the crystal structure, Figures 3.12c and d. Compared to when operating in the WiS electrolyte the specific capacity is lower and the kinetics are slower, as seen in the dQ/dV plot. This can be attributed to the slow kinetics of ion insertion and bulk ionic conduction when operating in a nonaqueous environment and within a dehydrated crystal structure. To quantify this difference the same kinetic analysis was performed for the material in the organic electrolyte and is shown in Figure 3.13. The average gradient of the lines of best fit in the root scan rate versus peak current is $0.094\,\mathrm{mA\,s^{1/2}\,V^{-1/2}}$, which corresponds to an average diffusion coefficient of $3 \times 10^{-8}\,\mathrm{cm^2\,s^{-1}}$. This is approximately two orders of magnitude lower than the diffusion coefficient in the water-containing electrolyte.

When operating with a cut-off voltage of $-1.65\,\mathrm{V}$ vs. SHE there is an additional voltage plateau at $-1.45\,\mathrm{V}$, Figures 3.12c and d. Ex situ XRD shows that after the first full discharge the crystalline structure has been lost. Over this lower voltage plateau there is large irreversible capacity and subsequent cycling shows higher specific capacity than the theoretical value for this material. This behaviour is similar to other

PBA materials cycled to low potential in nonaqueous electrolytes, where capacity has been associated with conversion-type charge mechanisms.[144–146] From this data it is clear that for MnHCCr there is a lower potential limit to the stability of the crystalline structure at around $-1.30\,\mathrm{V}$ vs. SHE. This is an important finding as the low potential stability limits for PBA compounds are critical to developing PBA anode materials, but are currently unknown.

3.5 Conclusions

In summary, manganese hexacyanochromate (MnHCCr) was successfully synthesised with a large cubic particles. Its structure was comprehensively characterised with a particular focus on structural water. In a high-voltage 'water-in-salt' electrolyte MnHCCr exhibited a reversible redox couple at $-0.86\,\mathrm{V}$ vs. SHE. Crucially, ex situ XRD and FTIR spectroscopy has been used to study the reaction mechanism and confirms that charge storage is from reversible sodium insertion and chromium redox, whilst maintaining the crystal structure. This is the lowest potential PBA compound for which that has been reported. MnHCCr shows a high sodium diffusion coefficient of $1.9 \times 10^{-6}\,\mathrm{cm^2\,s^{-1}}$ and less than 1% strain on cycling.

Operating in a nonaqueous electrolyte the same MnHCCr redox couple is active but the reaction kinetics are comparatively sluggish. Further reduction in potential results in a breakdown in the crystalline structure. The low potential stability limit of MnHCCr was found to be around $-1.30\,\mathrm{V}$ vs. SHE.

Investigations into low potential PBA compounds are motivated by the development of PBA|PBA full cells in which both anode and cathode are PBA materials. To increase the voltage of such as cell there is a search for PBAs that operate at ever lower potentials. This study has shown that manganese hexacyanochromate has a low reduction potential and although the specific capacity is low at $62\,\mathrm{mA\,h\,g^{-1}}$

there is a clear roadmap for improvement. Specifically, investigating other transition metal hexacyanochromate compounds (other P site cations) and develop methods to synthesise those materials with low vacancy contents to enable high specific capacities.

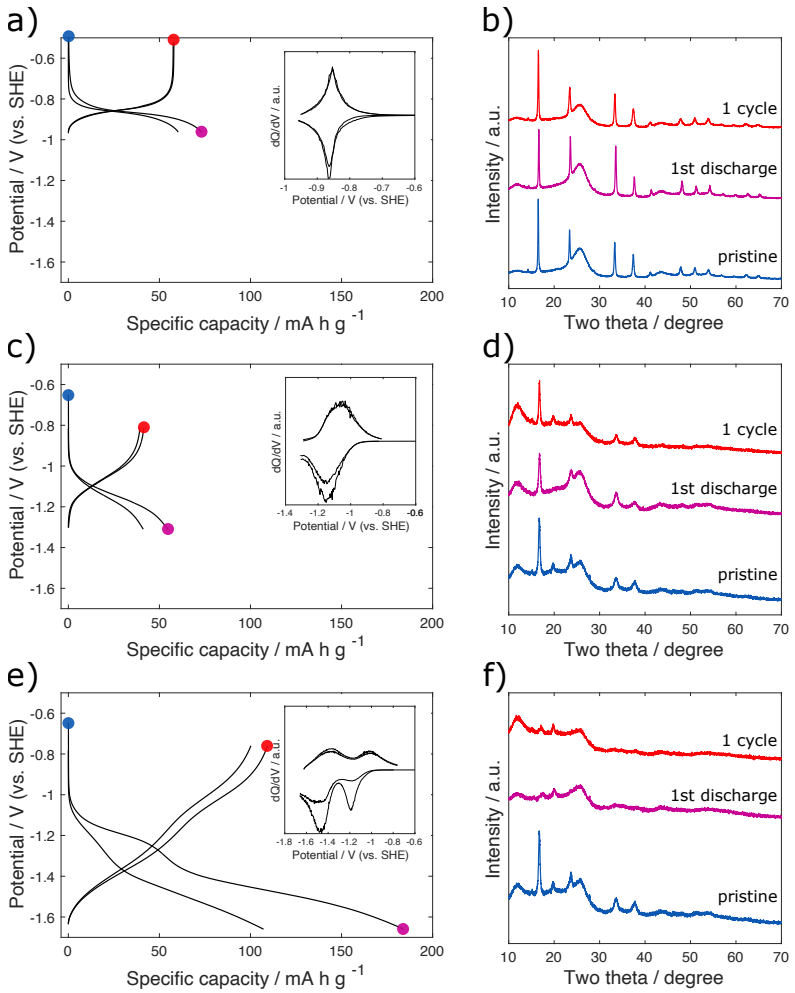


Figure 3.12: The galvanostatic profiles and corresponding dQ/dV plots (inset) of MnHCCr electrodes cycled twice in the WiS electrolyte (a) and in a organic electrolyte (b and c) with two different cut-off voltages. (c - e) Corresponding XRD patterns of ex situ electrodes taken in the pristine state, after the first discharge, and after the first full cycle. Reprinted (adapted) with permission from ref[123]. Copyright © 2013 American Chemical Society.

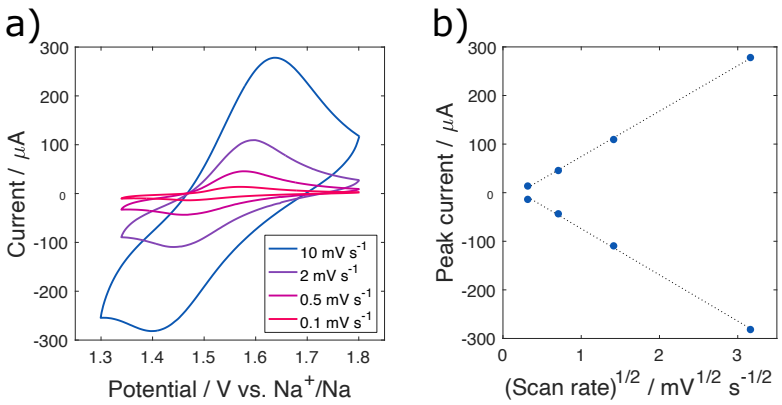


Figure 3.13: a) Cyclic voltammograms of MnHCCr in the organic electrolyte at scan rates between $0.1\,\mathrm{mV\,s^{-1}}$ to $10\,\mathrm{mV\,s^{-1}}$. (b) The peak current at each scan rate plotted against the square root of the scan rate. The average of the gradients of the lines of best fit is $0.094\,\mathrm{mA\,s^{1/2}\,V^{-1/2}}$. Reprinted (adapted) with permission from ref[123]. Copyright © 2013 American Chemical Society.

Chapter 4

Synthesis of zero-vacancy chromium(III) hexacyanochromate(III)

4.1 Abstract 86
4.2 Introduction 87
4.3 Experimental methods 91
4.4 Results and discussion 92
4.4.1 Preparation and characterisation of alkali metal chromium(II) hexacyanochromate(II) compounds 92
4.4.2 Preparation and characterisation of chromium(III) hexacyanochromate(III) 96
4.4.3 Magnetic properties 100
4.4.4 Electrochemical characterisation 102
4.4.5 Thermodynamic considerations 105
4.4.6 Alternative synthesis routes 106
4.5 Conclusions 107

4.1 Abstract

Low-vacancy chromium(III) hexacyanochromate(III) is an attractive material due to its predicted properties: two-electron redox reaction at low potential providing high specific capacities, and room-temperature magnetisation as it's isoelectric to vanadium(II) hexacyanochromate(III) whilst also being stable in air. It is also elusive. Synthesis is remarkably difficult and characterisation techniques cannot easily

distinguish low-vacancy chromium(III) hexacyanochromate(III) from a high-vacancy analogue. In this chapter I present a synthesis route of zero-vacancy chromium(III) hexacyanochromate(III) that consists of first preparing rubidium chromium(II) hexacyanochromate(II) using anhydrous N-methyl formamide (NMF) as the solvent, which is subsequently oxidised in water. Success of the synthesis relies of careful consideration of both alkali cation and solvent, which will be discussed in detail. The electrochemical and magnetic properties of zero-vacancy chromium(III) hexacyanochromate(III) are investigated.

4.2 Introduction

As previously discussed in the Introduction and in Chapter 3 a high specific capacity (150 mAh/g or more) PBA anode material requires low vacancy content and two redox couples that are active at low potential. This is the same logic as the development of high capacity PBA cathode materials apart from the redox couples are active at high potential. We have already observed that the redox couple in transition metal hexacyanochromates, $P[Cr^{III/II}(CN)_6]$, operates at low potential, and so transition metal hexacyanochromates are attractive materials. We also know that the reduction potential of the P site cations in PBA materials are reasonably close to their standard reduction potential. Therefore, $Ti^{III/II}$, $V^{III/II}$, and $Cr^{III/II}$, with standard reduction potentials around -0.4 V vs. SHE, appear to be promising P site metals, and therefore $Ti[Cr(CN)_6]$, $V[Cr(CN)_6]$ and $Cr[Cr(CN)_6]$ are possible high capacity anode materials assuming synthesis of low vacancy material is possible. However, titanium and vanadium are difficult to incorporate in the PBA lattice and tend to form titanyl or vanadyl ions when exposed to air, disrupting the structure and possibly rendering the ions redox inactive. The clear candidate material is chromium hexacyanochromate.

There is a rich history of synthesis and characterisation of transition metal hex-

acyanochromates, $P[Cr^{III/II}(CN)_6]$, in the molecular magnetism literature of the 1990s.[106] The hexacyanochromate(III) complex was the building block of choice owing to its stability in air and water, and having the maximum possible spin (electronic configuration of t_{2g}^3). The most important parameter in the development of molecular magnets is ensuring magnetisation up to and above room temperature, and the determinants of the magnetic ordering temperature are detailed in the Introduction. Briefly, a high magnetic ordering temperature is only possible for materials with antiferromagnetic interactions and the ordering temperature is maximised when the number of unpaired t_{2g} electrons is maximised and vacancy content is minimised. This logic is supported by vanadium(II) hexacyanochromate(III), the only PBA with room temperature magnetisation, in which both metals have the electronic configuration t_{2g}^3. Another prospective PBA composition with high magnetic ordering temperature is chromium(III) hexacyanochromate(III), as its isoelectric to vanadium(II) hexacyanochromate(III), and has the addition benefit of being thermodynamically stable in air.

The issue in the preparation of chromium(III) hexacyanochromate(III) is that Cr^{3+} is substitution inert in solution, preventing direct synthesis. One notable attempt was made to produce a complex that contained labile Cr^{3+} however the material produced was amorphous and had a low ordering temperature.[157] In the molecular magnetism literature chromium(II) hexacyanochromate(III), $Cr[Cr(CN)_6]_{2/3}$, was synthesised and characterised, and had a magnetic ordering temperature of 240 K.[94] This composition also supports the proposition that chromium(III) hexacyanochromate(III) would have a room temperature or high ordering temperature as $Cr[Cr(CN)_6]_{2/3}$ has a high vacancy content and an e_g electron on the P site that would interact ferromagnetically, both of which reduce the magnetic ordering temperature. There were subsequent attempts to produce chromium hexacyanochromate electrochemically.[38,158] From a solution containing Cr^{3+} and $Cr(CN)_6{}^{3-}$ an electrode was driven to low potentials,

electrochemically reducing the Cr^{3+} to Cr^{2+}, triggering precipitation onto the electrode. The oxidation state of the deposited material can then be controlled electrochemically. The magnetic ordering of such materials were increased to 270 K. Even though one report concluded the composition was indeed $Cr^{III}[Cr^{III}(CN)_6]_1$, it was likely these materials did, in fact, contain a significant fraction of vacancies and Cr^{2+}.

Characterisation of oxidised chromium hexacyanochromate is particularly difficult as compositions in the range ${Cr^{II}}_{1\text{-}z}{Cr^{III}}_z[Cr^{III}(CN)_6]_{1\text{-}y}$ (where $z = 3y$ and $0 < y < 1/3$) give remarkably similar XRD patterns, FTIR and XPS spectra, and ICP cannot be used to determine vacancy content for obvious reasons. Magnetic properties, and to a lesser degree electrochemical properties, provide a better measure of vacancy content and determination of whether zero-vacancy chromium(III) hexacyanochromate(III) is synthesised or not. The 'ideal' chromium(III) hexacyanochromate(III) would be antiferromagnetic as spin sublattices would be equal and opposite. The electrodeposited chromium hexacyanochromate materials gave large saturation magnetisations, similar to what is observed for $Cr[Cr(CN)_6]_{2/3}$, suggesting a significant vacancy content.[38,158] The highest ordering temperature for vanadium(II) hexacyanochromate(III) was achieved via a sol-gel synthesis route which reduced the vacancy content resulting in a reduced saturation magnetisation, compared to a high vacancy material, see Figure 1.14.[100] Non-stoichiometry in the material, resulting in ferrimagnetic behaviour was assigned to non-zero vacancy content and partial oxidation of V^{2+}.

Given that it is not possible to produce chromium(III) hexacyanochromate(III) directly as Cr^{3+} is substitution inert in solution, it must be synthesised in the mixed valence or reduced state, and then oxidised. There are two issues. First, is ensuring precursors, intermediate compounds, and the synthesised PBA are chemically stable. Cr^{2+} is thermodynamically unstable in water and in contact with oxygen (dissolved and atmospheric). However, it is kinetically stable in deaerated water. The intermediate complex, whether its ${Cr(CN)_6}^{3-}$ or ${Cr(CN)_6}^{4-}$, must be stable to dissociation.

Hexacyanochromate(III) is widely available, highly stable against ligand exchange, and chemically stable in water and air. Hexacyanochromate(II), however, is only stable against oxidation in deaerated water and, importantly, is in a dynamic equilibrium with $Cr(CN)_5^{3-}$, see equation below.[159]

$$Cr(CN)_5^{3-} + CN^- \rightleftharpoons Cr(CN)_6^{4-} \tag{4.1}$$

DFT modelling shows that the dielectric constant of the solvent is crucial and the higher the dielectric constant the more to the right of the above reaction the equilibrium sits.[155] In water ($\epsilon = 80$) the hexacyanochromate(III) complex is only stabilised with excess CN^- and so synthesis of chromium hexacyanochomate is either not possible[159] or inevitably results in high-vacancy material.[160] Solvents with lower dielectric constants such as acetonitrile ($\epsilon = 37.5$) show no stability of the hexacyanochromate(III) complex.[159]

Second, ensuring that the charge neutrality mechanism of the as-synthesised material is through inclusion of interstitial ions, rather than hexacyanochromate vacancies. For charge neutrality the material must have zero vacancies to form chromium(III) hexacyanochromate(III) when oxidised. In battery literature it is known empirically that it is easier to reduce the vacancy content in the reduced state compared to the mixed valence state. Strategies to promote synthesis of low-vacancy material include using a large excess (often to the solubility limit) of the interstitial cation in solution, increasing the reaction temperature, or using a chelating agent (most commonly citrate) on the P site transition metal which slows the reaction. In the literature for synthesising PBA magnetic materials, where the nature of the interstitial cation is not constrained unlike battery materials, the larger the cation the higher alkali cation content in the synthesised material, and lower the vacancy content. Often, cesium is added to a synthesis, instead or in addition to potassium, to lower the vacancy content. However, it has been shown previously that cesium will

not readily be removed from the chromium hexacyanochromate structure, therefore, syntheses that incorporate cesium into the structure are likely not viable.[94]

Motivation for developing a synthesis procedure for chromium(III) hexacyanchromate(III) is provided by its predicted magnetic and electrochemical properties. However, development of such a procedure is a challenging synthetic chemistry problem. This chapter details a synthesis procedure that consists of first producing zero-vacancy rubidium chromium(II) hexacyanochromate(II) in anhydrous N-methyl formamide (NMF) which is then oxidisation in water. Rationale in the design of the synthesis procedure and factors contributing to its success will be discussed.

4.3 Experimental methods

All solvents were purchased anhydrous and dried with molecular sieves. Salts were either purchased anhydrous ($CrCl_2$) or dried aggressively and stored in an Ar-filled glovebox. Syntheses were performed inside an Ar-filled glove box.

A typical synthesis comprised of dropwise addition of equal volumes of a solution containing 40 mM $CrCl_2$ to a solution of 120 mM ACl (A = Na, K, Rb, Cs) and 120 mM NaCN under vigorous stirring at 60 °C. Solvents used were formamide, N-methyl formamide (NMF) and dimethylformamide (DMF). Solutions were left to stir for 10 to 30 minutes then allowed to cool. Whilst maintaining an inert atmosphere, solutions were centrifuged and the supernatent poured out. The precipitate was washed with the corresponding solvent once and with anhydrous acetonitrile twice and dried under vacuum at 80 °C overnight.

To produce the oxidised material instead of drying the precipitate after washing with acetonitrile the precipitate was exposed to air and added to acidified deionised water. The pH of the water was reduced to 2 by addition of nitric acid. The precipitate-water mixture was allowed to stir exposed to air for 30 minutes. After stirring the

solution was centrifuged twice with water and once with acetronitrile, and dried overnight in air at 80 °C.

Samples were characterised using the same techniques that were described in Chapter 3. For reduced materials XRD and FTIR spectroscopy were performed in N_2-filled gloves boxes and samples transferred without exposure to air. In addition, the magnetic properties were studied using a superconducting quantum interference device (SQUID).

4.4 Results and discussion

4.4.1 Preparation and characterisation of alkali metal chromium(II) hexacyanochromate(II) compounds

Given that aqueous synthesis of zero-vacancy alkali metal chromium hexacyanochromate is not possible there was a search for suitable solvents to prepare alkali metal chromium hexacyanochromate in the reduced state. Due to the requirement that the solvent has a high dielectric constant ($\epsilon > 80$), to stabilise $Cr(CN)_6^{4-}$, formamide ($\epsilon = 110$)[161] and NMF ($\epsilon = 182$)[161] appeared promising and were studied. There are very few solvents with a dielectric constant higher than that of water and NMF has the highest dielectric constant of any liquid at room temperature.[161] For comparison DMF ($\epsilon = 39$) which is chemically similar but has a lower dielectric constant was also studied. The chemical structures of formamide, NMF, and DMF are displayed in Figure 4.1. They all had solubility of the precursor salts and were stable against reduction.

A series of alkali metal chromium hexacyaonchroamte materials were produced by dropwise addition of a solution of $CrCl_2$ to a solution of NaCN and ACl in the selected anhydrous solvent. There were stoichiometric ratios of Cr^{2+}:CN^- and excess alkali

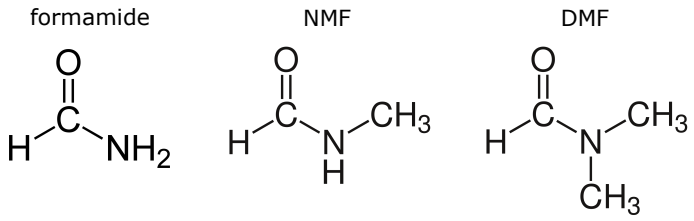


Figure 4.1: The chemical structures of formamide, N-methyl formamide (NMF) and dimethylformamide (DMF).

metal A^+. This reaction was designed so that in the reaction vessel there is always sufficient or excess CN^- and A^+, and the reaction is limited by ligand exchange.

The general chemical reactions are as follows

$$Cr^{2+} + 6\,CN^- \longrightarrow Cr(CN)_6{}^{4-} \tag{4.2}$$

$$Cr^{2+} + (1-y)Cr(CN)_6{}^{4-} + 2\,xA^+ \longrightarrow A_{2x}Cr[Cr(CN)_6]_{1-y} \tag{4.3}$$

The first step in the reaction is formation of the intermediate complex, $Cr(CN)_6{}^{4-}$. It has been reported that this complex is red in colour.[160] All the reactions in DMF did not produce any colour change from the precursor solutions on mixing and no precipitate was formed. It is reasonable to conclude that the low dielectric constant (ϵ=39) prevented the formation of the intermediate complex, inhibiting the reaction.

For syntheses in formamide and NMF a precipitate was formed for all compositions. However, there were distinct differences observed during the reaction, in the yields, and in the XRD patterns (Figure 4.2). The XRD patterns are significantly dependent on the alkali cation content and the changes are larger for larger cations. In addition to the experimental XRD patterns simulated patterns of three materials are shown for comparison. In formamide, syntheses with Na^+, K^+ and Rb^+ produced materials that had high vacancy contents, whilst synthesis with Cs^+ produced material with near-zero vacancy content. For Na^+ and K^+ syntheses on addition of the $CrCl_2$

solution the reactant mixture first turns red. After adding about half the $CrCl_2$ solution precipitation occurs and the solution turns dark green. It appears that the intermediate complex is formed until all the CN^- is consumed and only then the PBA is precipitated. For both Rb^+ and Cs^+ syntheses precipitation is instantaneous from the first addition of $CrCl_2$.

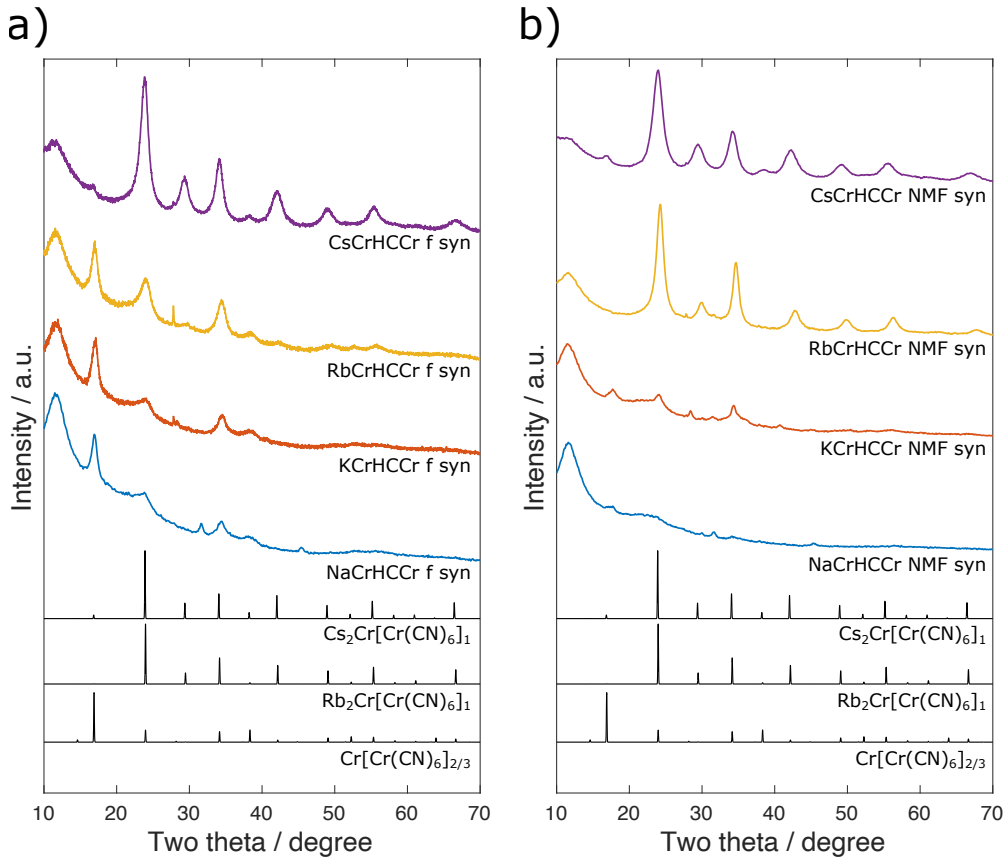


Figure 4.2: XRD patterns of materials produced with a series of alkali cations present in solution using a) formamide and b) NMF as the solvent. Simulated patterns are included for comparison.

In NMF, syntheses with Na^+ and K^+ produced very little precipitate even after 30 minutes of additional stirring. The material was also very low crystallinity. Conversely, in syntheses with Rb^+ and Cs^+ precipitation occurred instantaneously on first addition of $CrCl_2$ and material produced was cubic and had near-zero vacancy contents.

Both formamide and NMF have sufficiently high dielectric constants (ϵ=110 and

ϵ=182) to stabilise the hexacyanochromate(II) complex and remaining differences appear to be from the solvent molecule size. Formamide is small enough that it can bond within vacancies to stabilise them, in an analogous manner to water. NMF, however, is a larger molecule and cannot fit within vacancies, driving up the energy of including vacancies in the structure. It also appears that zero-vacancy sodium and potassium chromium hexacyanochromate compounds are inherently unstable, most likely due to the small size of the cations. It is worth noting that Na^+ and K^+ are insertion cations in most PBA battery materials, and stabilisation of these small cations rely on partial hydration within the subcube. In the absence of water, or an equivalent small solvent molecule, the energy cost of these small cations in the structure is relatively large. Formamide is small enough to bond within vacancies but not small enough to solvate interstitial ions in subcubes.

Comparing the formamide and NMF syntheses with rubidium; it appears that in the case of formamide forming both high and low vacancy material is possible yet the high-vacancy material is preferentially produced, whereas in the case of NMF only the zero-vacancy material is possible and so that is what is produced. For rubidium synthesis in NMF vacancy-free material is produced giving the reaction below.

$$Cr^{2+} + Cr(CN)_6{}^{4-} + 2\,Rb^- \longrightarrow Rb_2Cr[Cr(CN)_6]_1 \tag{4.4}$$

This synthesis fulfils the requirements stated previously of producing zero-vacancy chromium hexacyanochromate without including cesium. $Rb_2Cr[Cr(CN)_6]_1$ (RbCrHCCr) will be used in the next stage of the synthesis. The FTIR spectra using the ATR stage and in transmission of RbCrHCCr is shown in Figure 4.3. The material appears to be highly absorbing; data from the ATR stage has extremely low transmission and is almost featureless, whilst data collected in transmission mode also had very low transmission and only part of the spectra could be reliably produced after manual background subtraction. Regardless, in transmission mode the absorption bands were

defined and the peak corresponding to v(CN) was at 2069 cm^{-1} with a shoulder at lower wavenumbers.

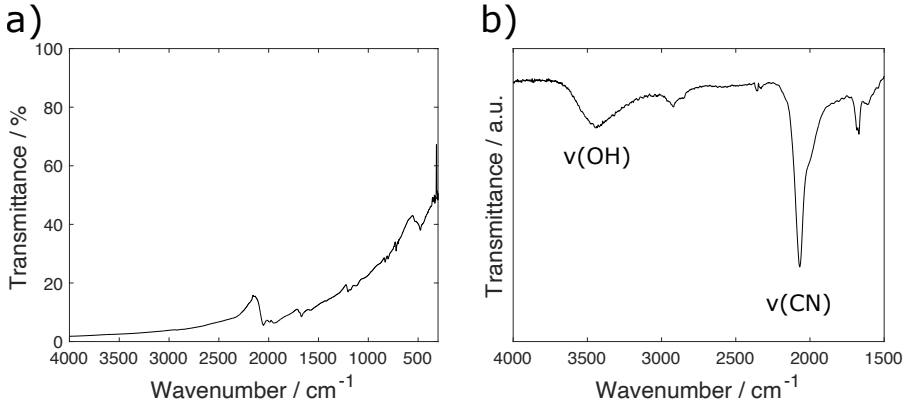


Figure 4.3: FTIR spectra of rubidium chromium(II) hexacyanochromate(II) synthesised in NMF using a) the ATR stage and b) in transmission mode. Majors absorption peaks are assigned.

4.4.2 Preparation and characterisation of chromium(III) hexacyanochromate(III)

Rubidium chromium(II) hexacyanochromate(II) synthesised in NMF (previous section) was oxidised spontaneously by addition of acidified water to form chromium(III) hexacyanochromate(III) (CrHCCr). The reaction is as follows.

$$Rb_2Cr^{II}[Cr^{II}(CN)_6] + 2\,H^+ \rightleftharpoons Cr^{III}[Cr^{III}(CN)_6] + 2\,Rb^+ + H_2 \qquad (4.5)$$

The water was acidified prior to adding the PBA material as the oxidation process drives the pH basic and PBAs are less stable in basic conditions. A significant pH increase was observed during the reaction, typically from ≈2 to ≈6. This reaction is spontaneous as the reduction potentials of both chromium sites, $Cr^{III/II}$, is below the reduction potential of protons, or water, or nitrate. Schematics of the crystal structures are shown in Figure 4.4.

Electron micrographs of CrHCCr shows that the material has a primary particle

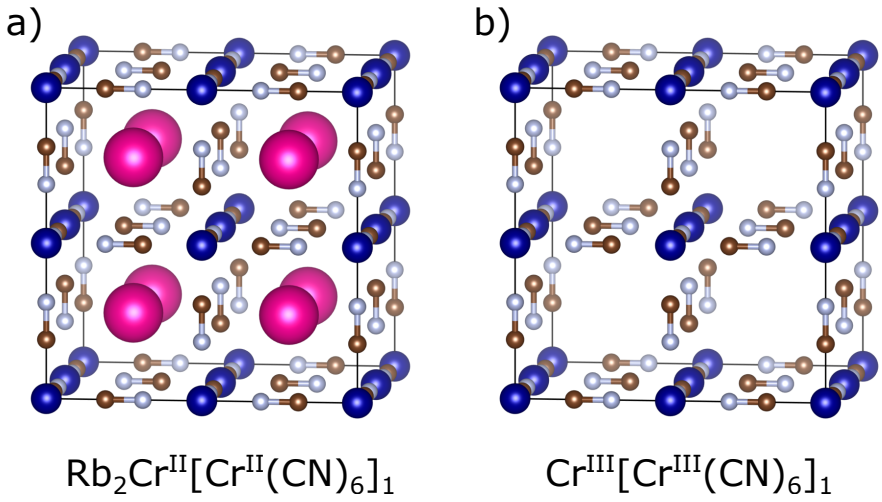


Figure 4.4: Schematics of the crystal structures of a) rubidium chromium(II) hexacyanochromate(II) and b) chromium(III) hexacyanochromate(III).

size of approximately 10 nm, Figure 4.5. The small particle size is a result of rapid nucleation of the PBA and very low solubility in NMF.

As a comparison, chromium(II) hexacyanochromate(III), $Cr^{II}[Cr^{III}(CN)_6]_{2/3}$, was synthesised in a conventional manner in water from Cr^{2+} and $Cr(CN)_6{}^{3-}$, with a high vacancy content. This material is labelled CrHCCr-aqsyn. The XRD patterns, Figure 4.6a, shows both CrHCCr and CrHCCr-aqsyn have the cubic structure as expected with lattice parameters of 10.43 Å and 10.39 Å, respectively. A crucial difference between the patterns is the relative intensity, or structure factor, of the $(1\,1\,x)$ planes, the most prominent examples being the (1 1 1) reflection at around 15°, highlighted in Figure 4.6b.

It has been described previously that the relative peak intensity of the (1 1 1) reflection reduces as the vacancy content of the PBA material reduces[97], and simulated patterns give this result (structure factor for the (1 1 1) reflection in CrHCCr and CrHCCr-aqsyn are 0.19 and 8.9 respectively, calculated by VESTA). Within the cubic PBA structure $(1\,1\,x)$ planes are the only set of planes in which each individual plane contains only the P or R site transition metals. These P only and R only planes

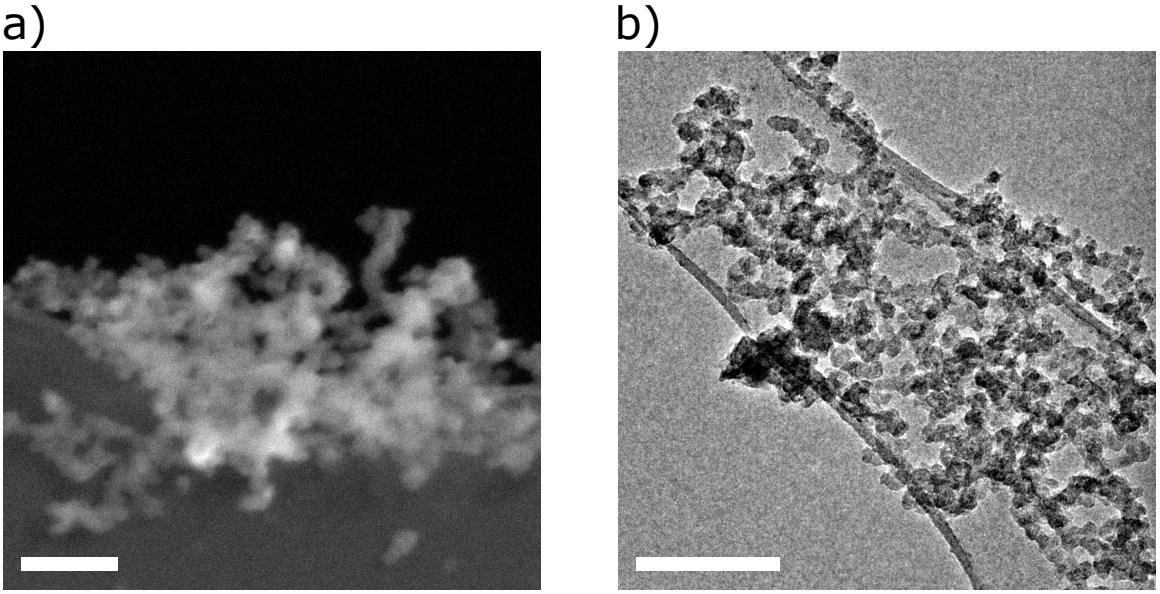


Figure 4.5: a) A scanning electron micrograph and b) transmission electron micrograph of CrHCCr. Scale bars are 100 nm. The transmission electron micrograph was taken by Dr. Weixin Song.

alternate and the interplanar distance is the distance between planes containing the same cation, schematically shown in Figure 4.7. If the vacancy content of the PBA is zero, giving a corresponding occupancy of R site metals as 1 then there is perfect destructive interference for the $(1\,1\,x)$ reflections. The calculated structure factors are very small but not zero as there are differences in X-ray scattering between C and N, and also between the P and R sites if they are different metals. As the vacancy content increases the scattering difference between the planes increases, resulting in less destructive interference and greater net scattering.

The FTIR spectra of CrHCCr and CrHCCr-aqsyn both have the v(CN) absorption band at around 2186 cm^{-1}, which is somewhat surprising as the oxidation state of the materials are different, Figure 4.8a. However, closer inspection of the bonding environment around the P site Cr is informative. The local environment around the CN in CrHCCr is $\mathrm{Cr^{III}(CN)_5-CN-Cr^{III}(NC)_5}$, and in CrHCCr-aqsyn is $\mathrm{Cr^{III}(CN)_5-CN-Cr^{II}(NC)_3(H_2O)_2}$. It appears that the effect on the CN stretch frequency of the decrease in charge on the P site Cr is offset by the fewer negatively charged

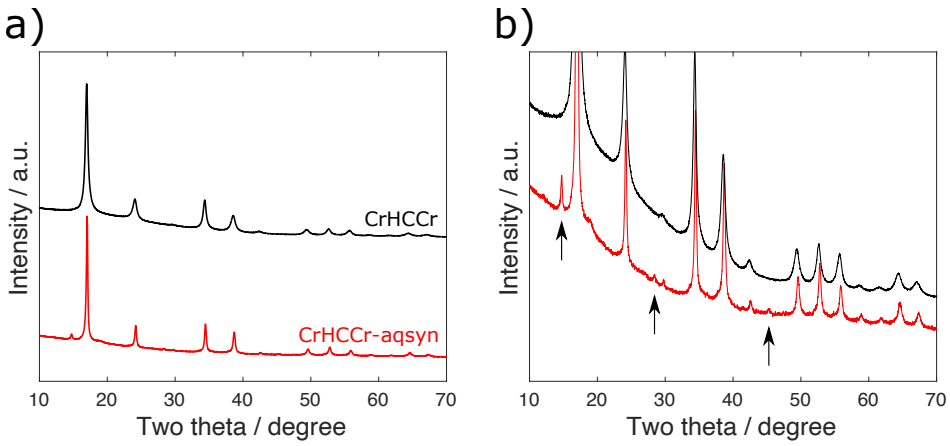


Figure 4.6: XRD patterns of CrHCCr and CrHCCr-aqsyn a) plotted over the whole data range and b) plotted with a reduced y axis. Arrows point to reflections from $(1\,1\,x)$ planes.

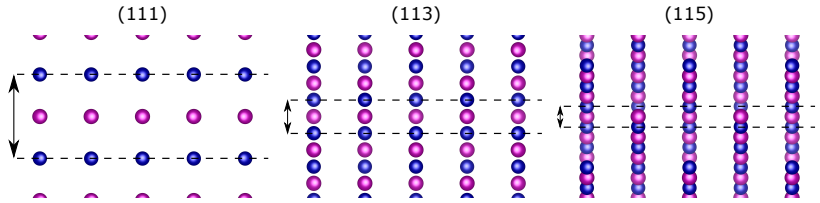


Figure 4.7: Schematic representation of planes of the PBA crystal structure. The view is along the plane and the normal direction to the plane is upwards. The arrows highlight the interplanar spacing for the given plane.

ligand bonded to it. Although this analysis is speculative it follows intuition that the remaining bonding environment around the P site metal will alter its influence on the cyanide ligand. CrHCCr-aqsyn has greater relative intensity of water stretching bands, ν(OH), in the range 3000−3700 cm^{-1}, including a sharp peak at 3660 cm^{-1}. Other framework vibrations are δ(Cr−CN) and ν(Cr−C) at 520 cm^{-1} and 437 cm^{-1}, respectively.

Thermogravimetry (TG) was used to study the water content of the two materials. CrHCCr-aqsyn loses approximately 4% of its mass up to 150 °C with a corresponding peak in the water mass spec trace (not shown) whereas CrHCCr does not lose significant mass in the same temperature window, Figure 4.8b. This suggests that the vacancies present in CrHCCr accommodate water which is then released whereas there is no

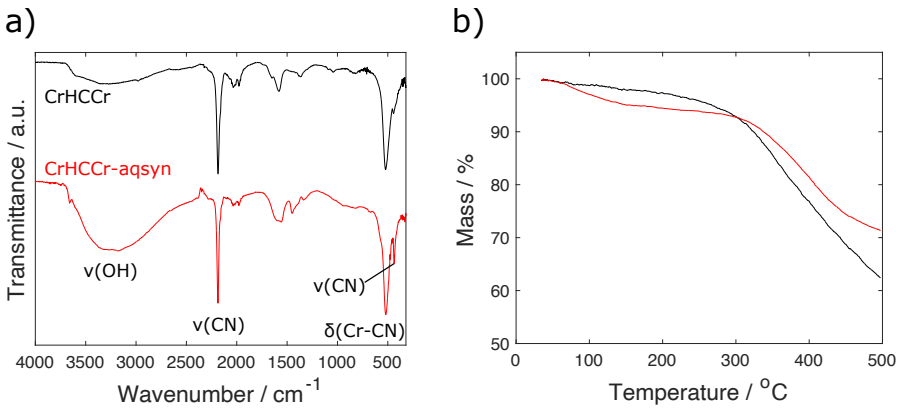


Figure 4.8: a) FTIR spectra and b) TG traces of CrHCCr and CrHCCr-aqsyn.

water in the CrHCCr sample.

4.4.3 Magnetic properties

Zero-vacancy chromium(III) hexacyanochromate(III) (CrHCCr) is predicted to be antiferromagnetic, however neither chromium(III) hexacyanochromate(III) or isoelectric vanadium(II) hexacyanochromate(III) have previously displayed antiferromagnetic behaviour, and instead show ferrimagnetic behaviour due to non-stoichiometry. CrHCCr-aqsyn provides an excellent comparison as its magnetic properties are known and have been reported previously.[94]

The field cooled magnetisation curves of CrHCCr and CrHCCr-aqsyn are shown in Figure 4.9a. CrHCCr-aqsyn is ferrimagnetic with an ordering temperature of 220 K. CrHCCr, however, has no appreciable magnetic moment at any temperature, consistent with it being antiferromagnetic. Plotting the same data with a log y axis, Figure 4.9b, shows that CrHCCr does in fact have an increase in magnetic moment at around 220 K, but its magnitude is around three orders of magnitude lower than that of CrHCCr-aqsyn.

Hysteresis loops of CrHCCr and CrHCCr-aqsyn at 5 K, Figure 4.9c, show characteristic antiferromagnetic and ferrimagnetic behaviour, respectively. Figure 4.9d shows the same data with reduced x and y axes. The coercive field for CrHCCr is

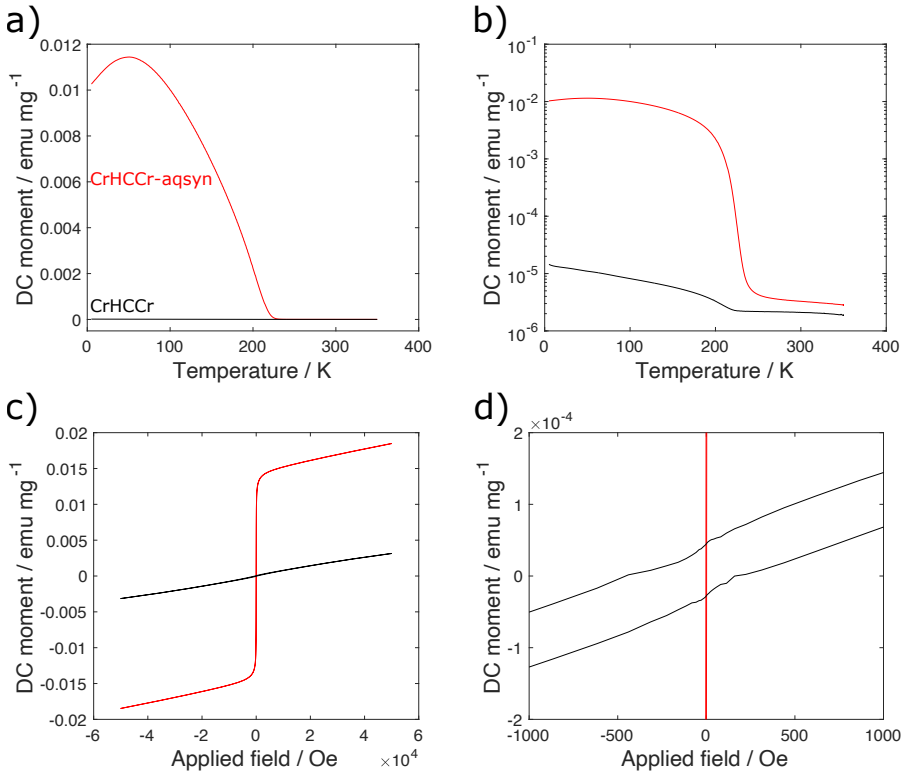


Figure 4.9: Magnetic properties measurements of CrHCCr and CrHCCr-aqsyn. a) and b) the field cooled magnetisation plots with linear and log y axes, respectively. An applied field of 100 Oe was used. c) and d) the hysteresis loops at 5 K over the whole data range and with restricted x and y axes, respectively.

>400 Oe, much higher than the coercive field for CrHCCr-aqsyn which is ≈2 Oe.

CrHCCr-aqsyn displays magnetic properties consistent with $Cr^{II}[Cr^{III}(CN)_6]_{2/3}$ reported previously and follows what is predicted from theory. CrHCCr, appears to primarily be antiferromagnetic with a small $Cr^{II}[Cr^{III}(CN)_6]_{2/3}$, or similar, impurity 'phase'. For CrHCCr to be antiferromagnetic the contributions from each spin sublattice must be equal in magnitude and opposite in direction. This suggests that the material is in fact vacancy-free and all Cr are in the 3+ oxidation state. The nature of the impurity 'phase' must be considered. It is most likely that this magnetisation arises from uncompensated spins at the crystal surfaces, a phenomena predicted by Néel's model and observed in other antiferromagnetic materials with nanoscale particle size.[162,163] The ordering temperature of the impurity 'phase' being similar to

CrHCCr-aqsyn is unsurprising as Cr atoms in vacancy-free material would have fewer neighbours at crystal surfaces, similar to bulk atoms in high-vacancy CrHCCr-aqsyn. The observed coersive field for CrHCCr is remarkably high for PBA materials (165 Oe for KVHCCr[100]) and best rationalised as the surface sites, those producing the net magnetisation, being magnetically coupled to the antiferromagnetic bulk material. Switching spins at the surface would necessitate switching spins of the bulk material.

It is difficult to measure the magnetic ordering temperature of any antiferromagnetic phase, due to the absence of a magnetic moment, and especially of a phase with an ordering temperature above the upper temperature limit of most conventional instruments such as SQUIDs, physical property measurement systems (PPMSs) or electron paramagnetic resonance (EPR) spectrometers.

4.4.4 Electrochemical characterisation

Preliminary electrochemical measurements were performed on chromium(III) hexacyanochromate(III) (CrHCCr) electrodes. Figure 4.10 shows the first discharge and subsequent full cycle galvanostatic profile, and corresponding differential capacity plot and ex situ XRD pattern, of chromium(III) hexacyanochromate(III) electrodes cycled in 37 mol dm^{-3} sodium bis(fluorosulfonyl)imide (NaFSI) in water (Figures 4.10 a - c), 1 M sodium perchlorate ($NaClO_4$) in propylene carbonate (PC) (Figures 4.10 d - f), and 22 M potassium trifluoromethanesulfonate (KCF_3SO_3) in water (Figures 4.10 g - i). The aqueous and nonaqueous sodium-ion electrolytes are the same was used in characterisation of manganese hexacyanochromate. 22 M KCF_3SO_3 in water is a high-voltage 'water-in-salt' potassium-ion electrolyte that has been reported recently.[75] For each electrolyte the ex situ XRD pattern is taken at the end of the second discharge, and plotted with the XRD pattern of a pristine electrode.

The material shows distinctly different behaviour in each electrolyte. In the aqueous sodium-ion electrolyte the material has a sharp plateau on first discharge at

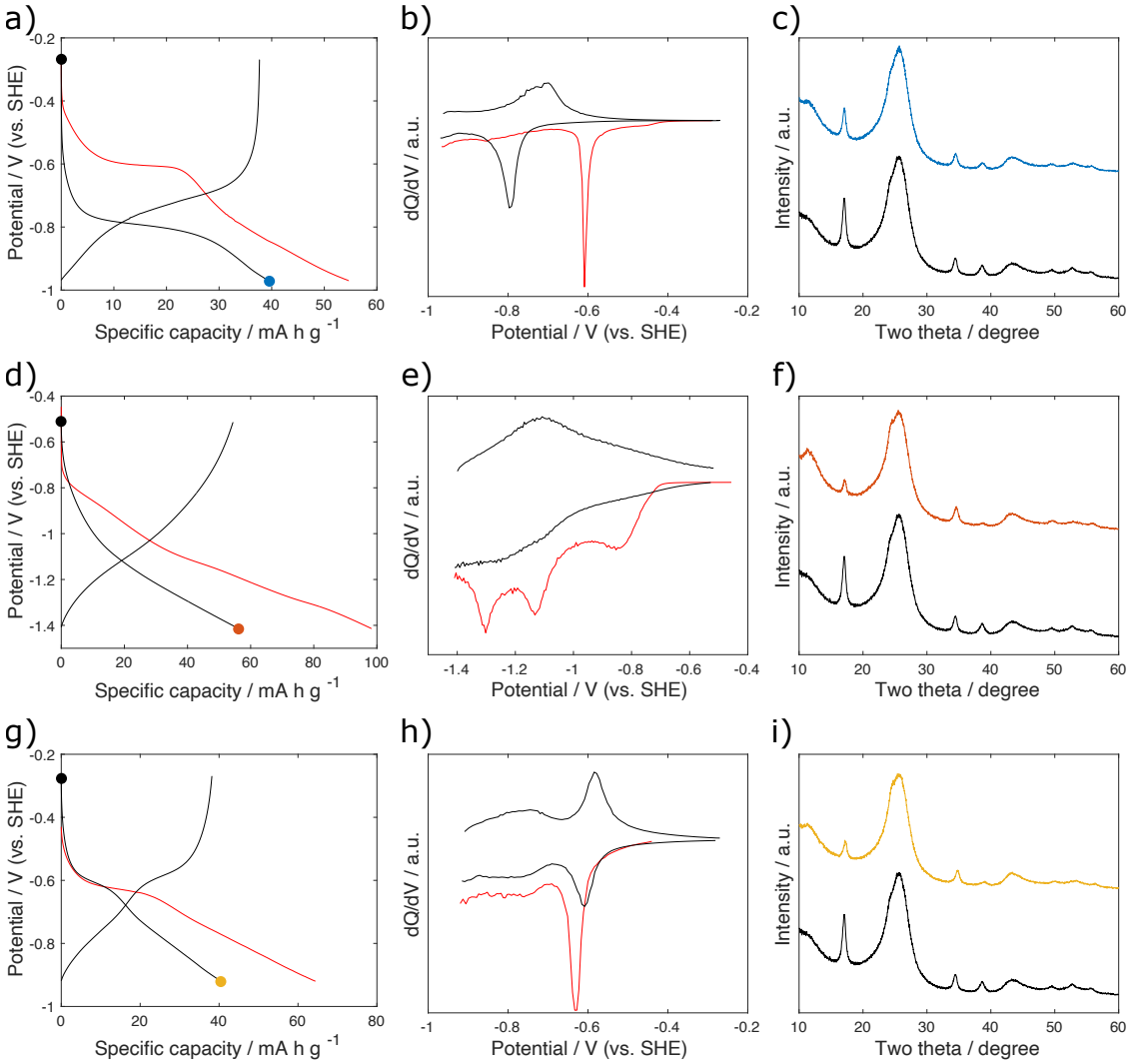


Figure 4.10: Galvanostatic profile, dQ/dV plot, and ex situ XRD patterns of CrHCCr electrodes cycled in (a - c) a sodium-ion aqueous electrolyte, (d - f) a sodium-ion nonaqueous electrolyte, and (g - i) a potassium-ion aqueous electrolyte. Red lines are the first cycle and black lines the subsequent cycle for electrochemical data. For XRD data the black line is the XRD pattern of a pristine electrode and the coloured line is the ex situ electrode taken at the end of the second discharge.

−0.6 V vs. SHE. On charge no corresponding oxidation peak is observed which means this capacity must come from an irreversible reaction. At lower potentials, around −0.8 V, there is a reversible redox couple observed. The ex situ XRD pattern shows the structure is maintained and moderate changes in the relative peak heights are observed.

In the nonaqueous sodium-ion electrolyte on first discharge there are three distinct

plateaus in the galvanostatic profile, observed as peaks in the dQ/dV. The subsequent cycle has a single broad plateau. The ex situ XRD shows the structure is maintained and the (2 0 0) and (4 0 0) peaks are of equal intensity, suggesting significant sodium concentration in the material.

Finally, in the aqueous potassium-ion electrolyte there are two distinct reversible redox couples at around −0.6 V and −0.8 V vs. SHE. Like in the nonaqueous sodium-ion case the ex situ XRD shows changes in relative peak height, indicative of potassium insertion into the structure.

All the samples show much lower specific capacities than predicted. This could be intrinsic to the material itself, but also could be from secondary factors. The electrochemical system presented here is not well-developed; few electrodes were made will low material loadings from small batches of chromium(III) hexacyanochromate(III). The extremely small particle size means any deleterious surface-specific reaction, such as partial solubility, could dominate the electrochemical behaviour. Additionally, it is difficult to ensure all particles are electronically connected to the current collector, which is necessary for them to take part in electrochemical reactions. Often when the active material particle size is so small great care is taken when preparing the active material composite electrode, such as creating carbon coatings on active material particles, using a larger weight fraction of carbon additive, and extensive mechanical milling of composite components.

Increasing the particle size and optimising the fabrication of composite electrodes are necessary to better characterise and improve the electrochemical properties of chromium(III) hexacyanochromate(III). Nevertheless, the two redox couples observed at around −0.6 V and −0.8 V vs. SHE demonstrates chromium(III) hexacyanochromate(III) undergoes a two-electron redox reaction, supporting the proposition that the material has a low vacancy content. The only other report of chromium hexacyanochromate exhibiting two redox couples observed them at very similar potentials

(-0.84 and −0.60 V vs. SHE).[38] This was from material produced via electrodeposition in attempt to reduce the vacancy content. Other literature reports of chromium hexacyanochromate produced through conventional synthesis routes, producing high vacancy material, only report a single redox couple at around −0.6 V vs. SHE.[28,115,164]

4.4.5 Thermodynamic considerations

The successful synthesis of zero-vacancy chromium(III) hexacyanochromate(III) via zero-vacancy rubidium chromium(II) hexacyanochromate(II) relies on considering and modifying the thermodynamics of the precipitation reaction. In the past, the thermodynamics of reaction have not been considered directly, and often kinetics is assumed to dominate the PBA precipitation reaction and resulting composition. However, it is likely that thermodynamics was indeed the factor controlling composition in many cases. For example, in the synthesis of low vacancy mixed valence state transition metal hexacyanochromate materials by substituting cesium in for potassium. Also, the role of water in conventional synthesis is seldom considered but does in fact influence the PBA composition in a number of ways. This work highlights the role that solvent and alkali cations play in stabilising the PBA structure.

Firstly, its appears that it is necessary to partially hydrate Na^+ and K^+ in the PBA structure otherwise the structure is too high energy to form. In nonaqueous synthesis PBAs containing these small cations did not form and density functional theory (DFT) modelling (without water) routinely, incorrectly predicts small cations on the face of the subcube rather than in the centre. Larger cations such as rubidium or cesium don't require partial solvation.[153,165]

Secondly, to stabilise hexacyanometallate vacancies in the PBA structure is it necessary for solvent molecules to fill the vacant N site and solvate the P site cation, otherwise the structure is too high energy to form. This role is conventionally played by water molecules but it appears that other small molecules, such as formamide or

acetonitrile, can also stabilise vacancies. If an appropriate solvent molecule is not present then structures with vacancies cannot form.

Thermodynamic and kinetic factors that influence the charge neutrality mechanism during the synthesis of PBAs are explored in further detail in Chapter 5.

4.4.6 Alternative synthesis routes

Alternative synthesis routes to form zero-vacancy chromium(III) hexacyanochromate(III) that were unsuccessful, but nevertheless informative, are presented below.

Firstly, it is known that using larger alkali cations during the synthesis of mixed valence state PBAs can effectively reduce the vacancy content. A deaerated aqueous solution of $CrCl_2$ was added dropwise to a solution of $K_3Cr(CN)_6$. Both solutions had high concentration of RbCl. On mixing a precipitate rapidly formed. The XRD pattern, Figure 4.11, shows no appreciable decrease in the (1 0 0) relative peak height compared to CrHCCr-aqsyn, or increase in relative peak heights that would indicate rubidium in the structure. The same synthesis was performed with the addition of potassium citrate ($K_3C_6H_5O_7$) to the $CrCl_2$ solution in a stoichiometric ratio of 1:1. On mixing no precipitate formed.

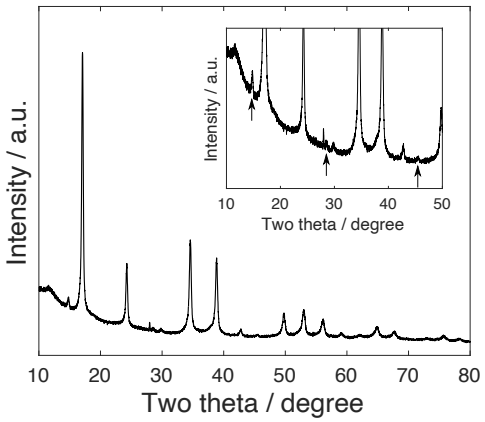


Figure 4.11: XRD pattern of the attempted synthesis of rubidium chromium(II) hexacyanochromate(III). Arrows point to reflections from (1 1 x) planes.

Secondly, cesium chromium(II) hexacyanochomate(II) ($Cs_2Cr[Cr(CN)_6]$) produced in NMF, in the same manner as rubidium chromium(II) hexacyanochomate(II), was oxidised in acidified water. Only a small fraction of the material was centrifuged out after the oxidisation step, the rest remained suspended. The XRD pattern and FTIR spectrum of the oxidised material are shown in Figure 4.12. It is clear that full oxidation of the material did not occurred and cesium remained in the structure.

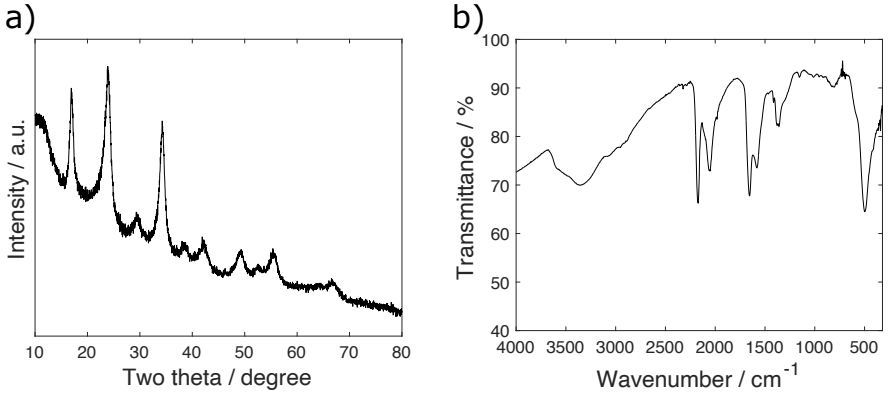


Figure 4.12: a) XRD pattern and b) FTIR spectrum of cesium chromium(II) hexacyanochomate(II) after oxidation in water.

4.5 Conclusions

In conclusion, the synthesis of zero-vacancy chromium(III) hexacyanochromate(III) was achieved through the development of an original synthetic procedure. The synthesis of rubidium chromium(II) hexacyanochromate(II) in NMF was successful due to the high dielectric constant of the solvent, which stabilised the $Cr(CN)_6^{4-}$ intermediate complex, and the inability of the solvent molecules to bond to the P site in hexacyanochromate vacancies, ensuring precipitation of material containing vacancies was not possible. Rubidium chromium(II) hexacyanochromate(II) was easily oxidised in acidified water to produce chromium(III) hexacyanochromate(III).

This is the first time that stabilisation of the $Cr(CN)_6^{4-}$ complex, without excess CN^-, has been demonstrated and the first time transition metal hexacyanochromate(II)

compounds have been synthesised. In addition to enabling the preparation of zero-vacancy chromium(III) hexacyanochromate(III) this synthesis demonstrates the ability to control the charge neutrality mechanism of synthesised PBAs through alkali cation and solvent selection.

Chromium(III) hexacyanochromate(III) exhibited antiferromagnetic behaviour and two redox couples at low potential whilst maintaining the crystalline structure. However, only a most primitive characterisation is presented here and there is great opportunity to optimise and improve the performance of the material for specific applications. Future experiments should aim to increase the particle size which will aid in more detailed characterisation of the as-synthesised material and improve its magnetic and electrochemical performance. In terms of magnetic properties, increasing the particle size will reduce the effect of the surface sites. Subsequent efforts should be focussed on experimentally measuring the magnetic ordering temperature, modelling the magnetic properties using modern DFT methods, and introducing non-stoichiometry into the material to induce ferrimagnetic behaviour. In terms of electrochemical performance, increasing the particle size will improve the electrochemical performance by reducing the effects of solubility, reducing surface reactions, and ensuring electrical contact to the current collector. In addition, the electrode preparation and electrolyte formulation should be studied and optimised in order to improve the specific capacity and cyclability of the material.

Chapter 5

Holistic model for determining the charge neutrality mechanism during the synthesis of Prussian blue analogues

5.1 Abstract 110
5.2 Introduction 110
5.3 Defining the problem 112
5.3.1 Treatment of water 113
5.4 Kinetic considerations 113
5.4.1 P site lability 114
5.5 Thermodynamic considerations 115
5.5.1 Separation of the reaction 115
5.5.2 Determining desolvation energy 116
5.5.3 Determining lattice enthaply 117
5.6 Application of the model 119
5.6.1 Alkali cation effect in mixed valence materials 119
5.6.2 Alkali cation effect in reduced materials 120
5.6.3 P site transition metal chelating agent 121
5.6.4 Rubidium chromium(II) hexacyanochromate(II) synthesis: effect of solvent and alkali cation 123
5.6.5 Prussian blue charge-transfer type synthesis 125
5.7 Conclusions 125

5.1 Abstract

Prussian blue analogues have a range of possible composition due to two competing charge neutrality mechanisms, either alkali cations or hexacyanometallate vacancies. The composition, in turn, significantly impacts many properties of the materials. Current methods to control the charge neutrality mechanism are based on empirical observations alone. In this chapter a holistic model is presented that attempts to rationalise the charge neutrality employed for PBAs given composition and synthesis parameters from basic thermodynamic and kinetic principles.

5.2 Introduction

In PBA literature almost all materials are synthesised in the mixed valence or reduced oxidation state. Typically they are synthesised from two precursors, the P site metal salt and R site metal complex. For such materials there is a range of possible composition given by the charge neutrality mechanism, whether hexacyanometallate vacancies or interstitial cations provide charge neutrality. For example, for the reaction between Mn^{2+} and $Fe(CN)_6{}^{3-}$ in the presence of K^+ the composition of the PBA formed can be $KMn[Fe(CN)_6]_1$, $Mn[Fe(CN)_6]_{2/3}$, or somewhere in between, Figure 5.1.

The properties of a given PBA material can vary widely based on the vacancy and interstitial cation content, and for specific application one charge neutrality mechanism is preferred over the other. As battery materials or magnetic materials the vacancy content is minimised in order to increase specific capacity or magnetic ordering temperature, respectively. In other applications, for example gas storage, the vacancy content is maximised. Furthermore, in certain cases the vacancy content is 'tuned' to a specific value. An explanatory example is cobalt hexacyanoferrate in which an intermediate vacancy content ($\approx$17.5%) is necessary to give the desired properties,

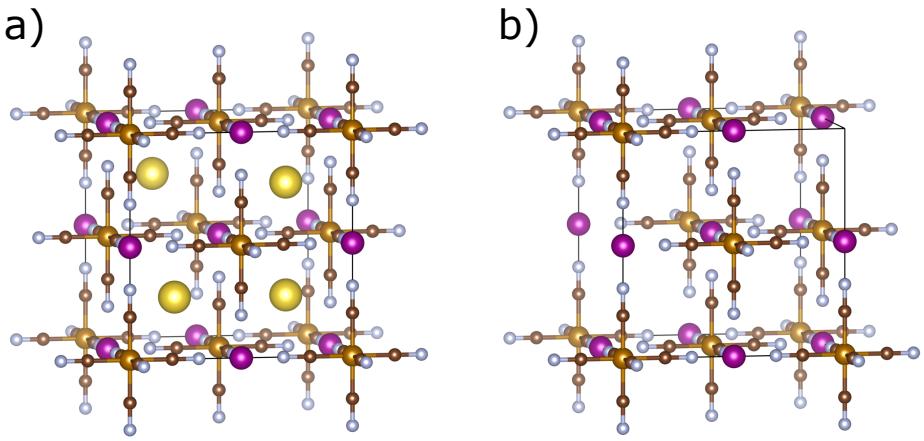


Figure 5.1: A schematic model of the PBA unit cell in the mixed valence state where charge neutrality is provided by a) alkali cations or b) hexacyanometallate vacancies.

in this case photo-induced changes to magnetisation.[97,166] A vacancy content too high or low does not give the desired properties.

Given the importance of controlling the vacancy content of PBA materials strategies have been developed to maximise or minimise the vacancy content. In most cases the desire is to minimise the vacancy content. Strategies include using larger alkaki metals such as cesium instead as sodium or potassium, increasing the alkali cation content in solution during synthesis (often up to the solubility limit), increasing temperature, or adding a chelating agent (citrate) to the P site metal. These strategies work to varying degrees of success but the rationale for their success, or failure, is not well understood. Additionally, they are not always applicable. For battery materials the alkali cation is not a variable that can be changed and adding citrate to mixed valence state material often prevents precipitation entirely. Additionally these strategies have limitations. Increasing the alkaki cation concentration of sodium or potassium enables the vacancy content to be reduced but only to around 10% in the reduced state, and sometimes there is no effect in the mixed valence state.

This chapter introduces a holistic model for the synthesis of Prussian blue analogues that attempts to predict and rationalise the charge neutrality mechanism, and therefore composition of the synthesised material, from basic kinetic and thermodynamic

principles.

5.3 Defining the problem

Convention in this model will be that a PBA in the 'oxidised' state has both transition metals in the 3+ oxidation state, in the 'mixed valence' state has one transition metal in 2+ and the other in 3+ state, and in the 'reduced' state has both transition metals in the 2+ state. This is a simplification and there are cases that fall out of these states by they do include most cases for which we are interested.

Firstly, synthesis in the oxidised state is trivial. To ensure charge neutrality the material must not contain vacancies or charge balancing cations. Below is the equation for synthesis in the oxidised state.

$$\mathrm{P}^{3+}_{(aq)} + \mathrm{R(CN)_6}^{3-}{}_{(aq)} \rightarrow \mathrm{P[R(CN)_6]_{1\ (s)}} \tag{5.1}$$

Not many PBA materials are actually synthesised in this oxidation state because there are few thermodynamically stable and labile P^{3+} aqueous species, the notable example being Fe^{3+}.

For mixed valance and reduced materials charge neutrality can either be achieved through hexacyanometallate vacancies or inclusions of charge balancing cations. Below are the reactions in the mixed valance and reduced state for which the variable y can take values between 0 and 1/3 and 0 and 1/2 respectively.

$$(1-3y)\mathrm{A}^{+}_{(aq)} + \mathrm{P}^{2+}_{(aq)} + (1-y)\mathrm{R(CN)_6}^{3-}{}_{(aq)} \rightarrow \mathrm{A_{1-3y}P[R(CN)_6]_{1-y\ (s)}} \tag{5.2}$$

$$(2-4y)\mathrm{A}^{+}_{(aq)} + \mathrm{P}^{2+}_{(aq)} + (1-y)\mathrm{R(CN)_6}^{3-}{}_{(aq)} \rightarrow \mathrm{A_{2-4y}P[R(CN)_6]_{1-y\ (s)}} \tag{5.3}$$

The values of y = 0 and y = 1/3 or 1/2 are the endpoints of a continuum and will

be termed zero-vacancy and high-vacancy respectively.

The function of this model is to predict the value of y for a reaction given the reactants, A, P, and $R(CN)_6^{n-}$, and reaction conditions such as reactant concentrations, solvent, temperature, other species present, reactant mixing among other variables. Given the complex and multivariate nature of this problem a quantitative, precise answer to this question is not possible and, rather, strategies that can promote either vacancy-rich or vacancy-poor synthesis will be proposed.

5.3.1 Treatment of water

The treatment of water in the system is very complicated. Water in the structure bonds directly to the P site transition metal in hexacyanometallate vacancies and also occupies interstitial sites. Clearly water in the structure is important and ignoring water completely would be unacceptable. In this model only coordinated water, which intuitively has the disproportionate impact on the lattice formation enthalpy, will be considered. Water bonded to A site cations in the structure will also be ignored.

5.4 Kinetic considerations

The PBA precipitation reaction can be described as a ligand exchange reaction around the P site metal. During the reaction the R site complex and A site cation, if present, must lose their solvation sphere. The P site metal must exchange its first solvation sphere water (or other solvent) ligands and replace them with $R(CN)_6^{n-}$ complexes. Due to the larger charge density of the P site cation it is assumed that the ligand exchange of the P site transition metal is kinetically the slowest step in the precipitation reaction, and therefore the reaction can be categorized as a ligand exchange reaction.

This is where the two reaction types, zero-vacancy and high-vacancy, differ. For the high-vacancy reaction only part of the P site solvation sphere must be exchanged;

the coordination environment of the P site changes from $P(OH_2)_6$ to $P(NC)_4(OH_2)_2$. Additionally, a relatively smaller number, (1 - 3y), of R site complexes are involved in reaction and no A site cations. In contrast, for the zero-vacancy reaction all the P site first solvation sphere ligands must be exchanged, from $P(OH_2)_6$ to $P(NC)_6$, a greater stoichiometric number of R site complexed must be desolvated, and A site cations are involved in reaction and must be desolvated. Crucially, the zero-vacancy synthesis requires three species present rather than two, slowing the reaction kinetics, and any kinetic restrictions from the A site cation will only impact the zero-vacancy synthesis.

The key takeaway from this reasoning is that the high-vacancy reaction is always kinetically easier than the zero-vacancy reaction.

5.4.1 P site lability

Since the reaction can be described as a P site ligand exchange reaction the ease with which the ligands can be replaced, otherwise known as the lability, is highly important. Lability is often quantified as the residence time of a water ligand in the first solvation sphere. In fact, the lability defined by this measure spans a vast range for the 3d transition metals. Cu^{2+} has a residence time of 5×10^{-4} µs whilst Cr^{3+} has a residence time of 2×10^{13} µs.[167] A lability this low means Cr^{3+} is effectively substitution inert in solution. Ligand field theory is necessary to explain differences across the 3d transition metals. If there are only electrons present in t_{2g} (bonding) orbitals then the bonds to the ligands are strong and the complex is inert, as in the case of Cr^{3+}. However, if there are also electrons in the e_g (antibonding) orbitals then the bonds to the ligands are weaker and the complex is labile. Other factors such as charge density are significant too.

The influence of P site lability on the preferred reaction mechanism is difficult to determine. It could speed up the precipitation process, inhibiting the ability for alkali cations to participate, or increase the likelihood that all the P site water ligands are

exchanged, promoting zero-vacancy synthesis.

5.5 Thermodynamic considerations

Firstly, the influence of entropy in the PBA synthesis reaction is complicated and hard to calculate. There are many sources of entropy; A site cations, solvent molecules, and vacancies. For the purpose of this model it is assumed to be small compared to other energies and will be excluded. What we do know, however, is that there will always be a decrease in entropy during the reaction.

As mentioned previously, water is crucial to the structural stability of PBAs. But, how to consider the thermodynamics of the coordinated water is complicated. For materials synthesised in the high-vacancy state the P site is partially hydrated. In this model the two reaction steps assumes the P site is fully desolvated and then partially resolvated. The accuracy of the model is then dependent on precisely calculating or modelling the effect of coordinated water on the lattice formation enthaply of the PBA, which is not trivial. Since the water molecules are directly bonded to the P site transition metal it is reasonable to assume the energy associated with the bond is significant.

5.5.1 Separation of the reaction

Taking the mixed valence state synthesis as an example the reaction can be broken down into two components; the desolvation enthalpy, $-\Delta H_{sol}$, and lattice formation enthalpy, U_{lat}, which are shown below.[168]

$$-\Delta H_{sol} \quad (1-3y)\mathrm{A}^{+}_{(aq)} + \mathrm{P}^{2+}_{(aq)} + (1-y)\mathrm{R(CN)_6}^{3-}{}_{(aq)} + 2y\mathrm{H_2O}_{(aq)} \rightarrow$$
$$(1-3y)\mathrm{A}^{+}_{(g)} + \mathrm{P}^{2+}_{(g)} + (1-y)\mathrm{R(CN)_6}^{3-}{}_{(g)} + 2y\mathrm{H_2O}_{(g)} \quad (5.4)$$

$$U_{lat} \quad (1-3y)\mathrm{A}^{+}_{(g)} + \mathrm{P}^{2+}_{(g)} + (1-y)\mathrm{R(CN)_6}^{3-}{}_{(g)} + 2y\mathrm{H_2O}_{(g)} \rightarrow$$

$$\mathrm{A}_{1-3\mathrm{y}}\mathrm{P[R(CN)_6]}_{1-\mathrm{y}} \cdot 2\,\mathrm{y}H_2O_{(\mathrm{s})} \quad (5.5)$$

The enthalpy of the precipitation reaction, ΔH_{rxn}, based on the these two components can be depicted graphically, Figure 5.2.

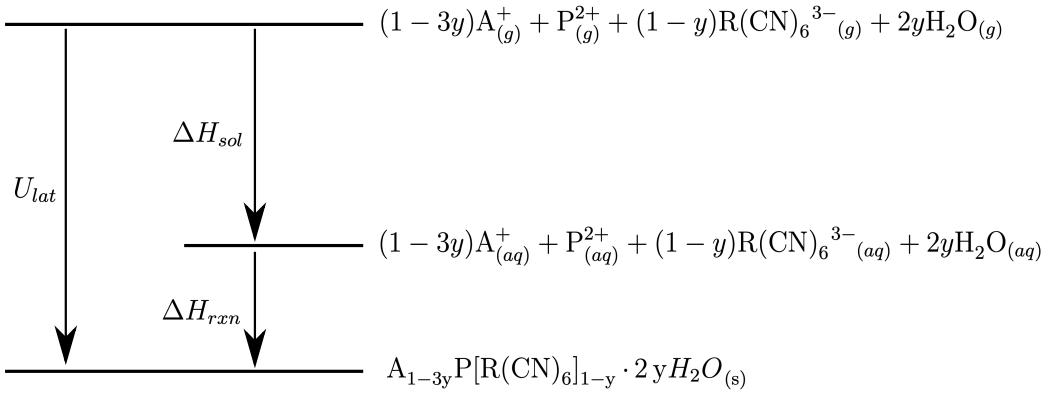


Figure 5.2: A graphical description of the relationship between reaction enthalpy, desolvation enthalpy, and lattice formation enthalpy.

These can be written as the following.

$$\Delta H_{rxn} = U_{lat} - \Delta H_{sol} \quad (5.6)$$

5.5.2 Determining desolvation energy

The (de)solvation enthalpy is the energy released when a ion isolated in vacuum is solvated, equation 5.4. The Born equation, shown below, estimates the electrostatic component of the Gibbs free energy of solvation of an ion, a. It treats the ion as isolated in a continuous dielectric medium.

$$\Delta G_{sol\ a} = -\frac{N_A e^2 z_a^2}{4\pi\epsilon_0(r_a + 2r_{H2O})}(1 - \frac{1}{\epsilon}) \quad (5.7)$$

z is the charge of the ion, r_0 is the effective radius of the ion, ϵ_r is the dielectric constant of the solvent, and other variables take there conventional definitions. What is important is that solvation enthaply scales with the charge density of the ion, that is charge divided by radius, and is also influenced by the dielectric constant, the larger the dielectric constant the larger the solvation enthaply.

The P site cation clearly has the largest solvation enthaply of the precursor chemicals. Also, the solvation enthaply of the alkali cations decrease as their size increases.

Additionally, a chelating agent can be used to modify the desolvation enthaply of the P site cation. Chelating agents, such as citrate[77] or pyrophosphate[169] preferentially bond to the P site cation over water and effectively increase the Gibbs free energy of solvation. This is an interesting modification to the precipitation reaction as the effect is the same, for the same P site cation, independent on whether high or low vacancy material is produced.

5.5.3 Determining lattice enthaply

Lattice formation enthaply, U_{lat}, is the energy released when isolated ions in vacuum are bought together into a solid, equation 5.5. Determining lattice formation enthaply is, in practice, the most complicated and difficult part when attempting to get quantitative results from this model. To be successful lattice formation enthalpies would have to be calculated as a function of vacancy content and whether water, or other small solvent molecule, is present to bond to the P site transition metal in vacancies.

Two methods were investigated to get quantatitive results; using the Born-Lande equation and using density function theory (DFT) methods.

The Born-Lande equation calculates the lattice formation enthaply of a crystalline compound from electrostatic interactions, as well as a repulsive potential energy term that dominates at small bond lengths. Whilst attractive due to its simplicity, the

Born-Lande equation has problems when being applied to PBAs. Firstly, it assumes all precursor species are isolated ions, whereas the R site complex ion is often a precursor for the synthesis of PBAs. It also does not treat fractional occupancy well. In a high-vacancy material the fractional occupancy of any carbon atom may be 2/3 but we know from the perspective of the R site transition metal the nearest carbon has an occupancy of 1 and next nearest most likely has an occupancy of less than 2/3. Although these problems exist they can be overcome by modifying the equation. Ignoring the nearest carbon and nitrogen atoms from the perspective of the R site transition metal would correctly 'model' the R site complex precursor, for example. The most unyielding problem is that the Born-Lande equations assumes point charges and only electrostatic and potential interactions, and no covalent bonding. As we known in Prussian blue analogues there is significant covalent bonding, especially within the R site complex. One could argue that seeing as most of the covalent bonding is within the complex, rather than between the complex, P site, and A site cations, the assumption of only ionic bonding is not as inappropriate as it seems on first inspection. However, there is still some covalent bonding between the P site cation and the cyanide linkages that cannot be reasonably ignored, and point charges would have to be assigned to all species for which, in isolation, we don't have reasonable estimates for.

DFT modelling can also be used to calculate lattice formation enthalpies by calculating the energy of a PBA and its corresponding precursor elements and compounds. However, PBAs are notoriously difficult to model accurately using DFT techniques due to their inherent complexity. The current state of the art is accurately modelling vacancy-free PBA materials. It is currently not possible to model PBA structures containing vacancies, whether water is present or not. This means DFT cannot be used to provide quantitative lattice formation enthalpy values for PBAs as a function of vacancy content and solvent. In the future when techniques to model PBAs have

improved it may be possible to incorporate them into this model.

For now, without accurate values of the lattice formation enthaplies the model is reliant on using experimental data and observations in combination with basic thermodynamic and kinetic principles.

5.6 Application of the model

It is clear that both the kinetics and thermodynamics of the precipitation reaction are crucial to determining whether a PBA will precipitate, and if it does which charge neutrality mechanism will dominate. If either the enthalpy of reaction, ΔH_{rxn}, is positive or the P site transition metal is substitution inert (Cr^{3+}) then no precipitation reaction will occur.

In the case that only the high vacancy or low vacancy synthesis is thermodynamically possible then clearly that will be the resultant composition. However, this case is not commonly found, with the notable exception of rubidium and cesium chromium(II) hexacyanochromate(II) synthesised in NMF which will be discussed later.

Rather, in most cases both high vacancy and low vacancy materials are thermodynamically possible. As the synthesis of high vacancy material is kinetically easier it is necessary, but not sufficient, that the enthalpy of reaction is more negative for the low vacancy synthesis otherwise high vacancy material will inevitably dominate. The amount that the enthalpy of reaction needs to be more negative depends on other factors.

Specific cases where the model has been applied are discussed below.

5.6.1 Alkali cation effect in mixed valence materials

For many Prussian blue analogues in the mixed valence state synthesis with only sodium or potassium in solution produces high vacancy material. This is even if the

concentration of alkali cation is greatly increased in the reaction solution medium. If either rubidium or cesium is added, even in relatively small concentration, then the vacancy content will be reduced and these large cations will be incorporated into the structure. This suggests that high vacancy material is thermodynamically more favourable compared to sodium or potassium containing low vacancy materials, but not compared to rubidium or ceasium containing low vacancy material, Figure 5.3. Increasing the size of the alkali cation size changes the thermodynamics in two ways; reducing the desolvation enthaply of the alkali cation and increasing the magnitude of the lattice formation enthaply.

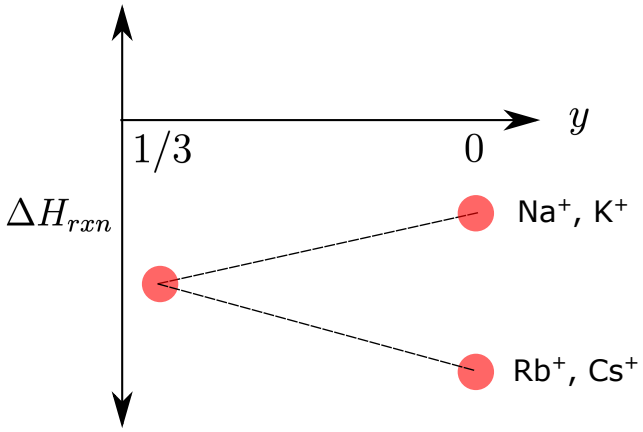


Figure 5.3: Schematic of how the enthalpy of reaction changes with vacancy content and alkali cation for mixed valence state materials.

5.6.2 Alkali cation effect in reduced materials

In reduced state materials it is common to increase the concentration of the sodium or potassium concentration in solution, often to the solubility limit, to minimise the vacancy content. Firstly, the fact that you can decrease the vacancy content at all in a meaningful way suggests that the low vacancy material is thermodynamically more favourable for any alkali cation, Figure 5.4. Increasing the concentration of alkali cations in solution reduces impact of slower kinetics associated with forming zero-vacancy material by ensuring the alkali cation is present in solution in vast excess.

There are diminishing returns to reducing the vacancy content as the alkali cation concentration is increased further as other factors promoting forming vacancies remain and become dominating. This suggests that, for a given composition and therefore fixed thermodynamics, there will be a limit to which the vacancy content can be reduced by changing reactant concentrations. In fact, a lower limit of a vacancy content of around 10% is attainable experimentally.

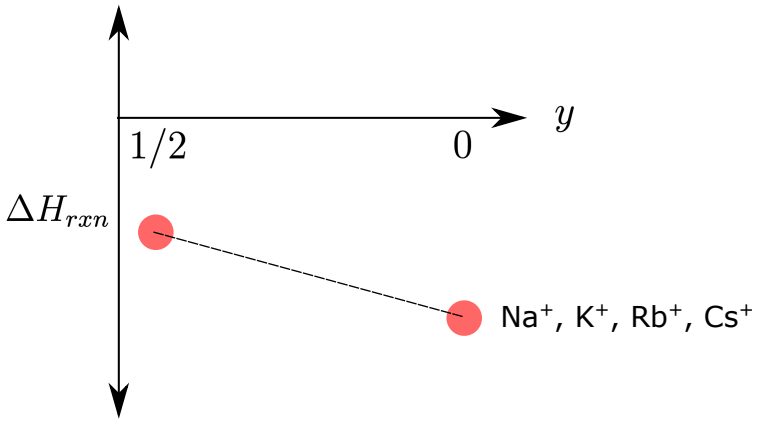


Figure 5.4: Schematic of how the enthalpy of reaction changes with vacancy content and alkali cation for reduced state materials.

5.6.3 P site transition metal chelating agent

Reducing the vacancy content with sodium and potassium in the structure is very important for battery applications. By simply increasing the concentration in solution and temperature the vacancy content can be reduced to around 10%. Recently, a citrate-assisted method has been developed that can reduce the vacancy content even further, approaching 0%. Citrate, or other chelating agents, are added to the P site salt solution prior to mixing with the solution the R site complex. The citrate-assisted method slows down the reaction dramatically and produces near zero-vacancy material with much larger particles. The rationale for its efficacy has been assigned to 'slowing the nucleation rate'[77] or citrate acting as a 'slow release reservoir' of P site cations[87]. Neither of these explanations are fully satisfying.

This model can describe the efficacy of the citrate-assisted method from a thermodynamic perspective. The citrate ligand replaces the water ligands around the P site cation prior to the reaction and can be thought of as increasing the desolvation enthaply. Admittedly the 'chelate effect' is primarily driven by entropy effects but from the perspective of the model, where entropy is largely ignored, the effect of the chelating agent can be though of as an increase in the desolvation enthaply. Since the P site cation is fully desolvated for any reaction, the shift in enthalpy of reaction is the same regardless of vacancy content, Figure 5.5. For materials synthesised in the reduced state the shift in enthalpy of reaction means that forming high vacancy materials are either no longer thermodynamically favourable or the magnitude by which it is favourable is considerably reduced. The enthalpy of reaction for low vacancy material is shifted by the same amount but remains negatives. This explains why the low vacancy reaction is promoted and the reaction is slowed considerably.

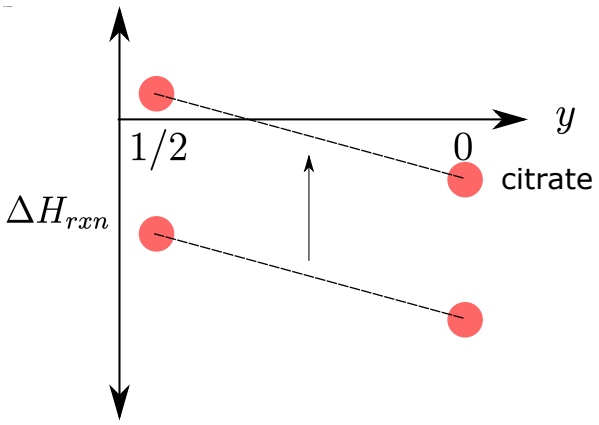


Figure 5.5: Schematic of how the enthalpy of reaction changes with the addition of citrate for reduced state materials.

There have been significantly fewer reports of using citrate-assisted synthesis in the mixed valence state. During attempts to reduce the vacancy content of mixed valence state rubidium chromium(II) hexacyanochromate(III) in water, citrate was added to the P site precursor solution. On mixing no precipitate formed. It appears that the enthalpy of reaction over the range of possible vacancy fractions was shifted

so that it was either positive, or negative but not sufficient in magnitude to drive the precipitation reaction. This experiment supports the thermodynamic rationale in the effect of chelating agents, and opposes the 'slow release reservoir' model for its effect.

In a reported synthesis of nickel(II) hexacyanoferrate(III), in the presence of potassium, adding citrate as a chelating agent did slow down the precipitation reaction but, contrary to its effect during the synthesis in the reduced state, did not reduce the vacancy content.[170] This results is supported by the thermodynamic model. Since the high vacancy content material is thermodynamically favourable without citrate, it is also favourable with citrate. Differing from the case of rubidium chromium(II) hexacyanochromate(III) the thermodynamic driving force for precipitation remained sufficient for nucleation, even after the increase in desolvation enthaply from the citrate. The model would predict that, for the same synthesis, if rubidium or ceasium were present low vacancy nickel(II) hexacyanoferrate(III) would be produced.

Using this model as a guide a greater number of chelating agents, with greater or lesser effect on the thermodynamics of synthesis, can be investigated. For example, a less strongly bound chelating agent may be effective in the synthesis of low vacancy rubidium chromium(II) hexacyanochromate(III).

5.6.4 Rubidium chromium(II) hexacyanochromate(II) synthesis: effect of solvent and alkali cation

The synthesis of reduced chromium(II) hexacyanochromate(II) with a number of alkali cations in a number of solvents is an excellent system for considering this model of PBA synthesis. In fact, rationalising the experimental results from the alkali metal chromium(II) hexacyanochromate(II) syntheses in Chapter 4 was a primary motivating factor in developing this model. In addition, the role normally water plays in the synthesis of Prussian blue analogues can be investigated due to its absence.

Taking the formamide syntheses first we see a very similar situation to conventional

synthesis in water. As you increase the alkali cation size the enthalpy of reaction for the low vacancy material gets more negative and at a critical point, for the Cs^+, it dominates and low vacancy material is produced.

Synthesis in NMF is different. Due to its inability to bond within vacancies the lattice formation enthaply of high vacancy material is drastically increased (less negative) and the reaction is no longer thermodynamically possible, Figure 5.6. This is the crucial point. The material is either precipitated in a low vacancy state or not precipitated at all. Also, the fact that the yield of material is low with potassium even after a long reaction time, and the structure of the precipitated material is different, is indicative that synthesis of the conventional PBA material with potassium in the structure is not thermodynamically possible. When comparing the synthesis of rubidium chromium(II) hexacyanochromate(II) in formamide and NMF it is likely that low vacancy material is thermodynamically possible in formamide but because that synthesis of high vacancy material is also possible and has faster kinetics, that is what is synthesised.

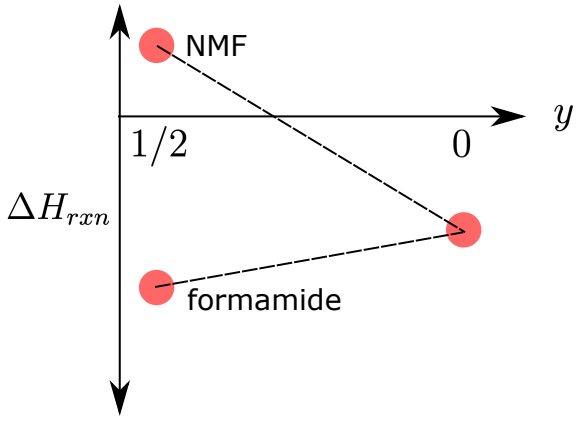


Figure 5.6: Schematic of how the enthalpy of reaction changes with solvent for reduced state materials.

Additionally, the fact that low vacancy sodium or potassium chromium(II) hexacyanochromate(II) does not precipitate in NMF tells us something about the role of water in the structure. You would conventionally expect sodium or potassium in

reduced materials to be stable. It is known that on ion insertion small cations, such as sodium or potassium, are only partially dehydrated. It appears that water hydrating small cations in the structure is not only favourable over not being hydrated but, in fact, is necessary to stabilise the structure during synthesis. This explains why dehydrating materials synthesised in water is so difficult and why phase transformations are often induced during dehydration of low vacancy materials.[89]

The syntheses in NMF are interesting because, for the first time, synthesis of high vacancy material is made thermodynamically unfavourable by changing the lattice formation enthaply for the material.

5.6.5 Prussian blue charge-transfer type synthesis

A notable exception to this general model is what can be termed the 'Prussian blue charge-transfer type' synthesis. In Prussian blue the oxidation state of the P site and R site components are different when in the precursor form, in solution, and in the PBA material. In solution Fe^{2+} and $Fe(CN)_6^{3-}$ are stable whereas as in Prussian blue Fe^{3+} and $Fe(CN)_6^{4-}$ are stable, which is due to the effect of increasing the $Fe(CN)_6^{3/4-}$ reduction potential from the polarising effect of the P site Fe. During or after the precipitation reaction there is metal to metal charge transfer (MMCT). This most likely increases the thermodynamic driving force for precipitation which explains the rapid nucleation of particles and high stability against dissolution.

5.7 Conclusions

This model fails to accurately describe the synthesis of PBAs in a quantitative manner due to the inherent complexity and lack of reliable methods to calculate crucial values. Instead, the model uses basic thermodynamic and kinetic principles in combination with experimental data and observations to infer information about the precipitation

reaction, and in particular the determinants of the charge neutrality mechanism employed. A few key conclusions can be made from this analysis.

- Forming high vacancy and low vacancy material are in competition and the result is determined by the kinetics and thermodynamics of reaction.
- It is kinetically easier to form high vacancy over low vacancy material due to only two species involved in the reaction and only partial P site ligand exchange.
- To form low vacancy material the thermodynamic driving force must be significantly larger.
- The reaction can be broken into desolvation and lattice forming steps, both of which are dependent on composition.
- Increasing the size of the alkali cation increases the thermodynamic driving force of the reaction by both decreasing the desolvation enthaply and decreasing the lattice formation enthaply (more negative).
- Citrate-assisted syntheses function by increasing the desolvation energy of the P site metal which reduces the thermodynamic driving force of the reaction by the same amount independent of vacancy content.
- Water or other solvent molecules bonded to the P site are crucial in decreasing the lattice formation enthaply and their absence makes synthesis of high vacancy material thermodynamically unfavourable.

This model allows for better informed design of PBA synthesis when a specific charge neutrality mechanism is desired. It also highlights that in almost all cases there are two competing charge neutrality mechanisms and one cannot presume the composition of a given material without sufficient thought and materials characterisation.

Chapter 6

Sodium zinc hexacyanoferrate as a solid electrolyte material

6.1 Abstract 127
6.2 Introduction 128
6.3 Experimental methods 131
6.4 Results and discussion 132
6.4.1 Physiochemical characterisation 132
6.4.2 Measurement of ionic conductivity 135
6.4.3 Optimisation of ionic conductivity 139
6.4.3.1 Effect of applied pressure 139
6.4.3.2 Effect of dehydration temperature 140
6.4.3.3 Activation energy 143
6.4.4 Electronic conductivity 145
6.4.5 Electrochemical stability 146
6.5 Conclusions 149

6.1 Abstract

There is great scientific interest in replacing the flammable liquid electrolyte in conventional lithium- and sodium-ion batteries with a solid material. Prussian blue analogues have already been demonstrated as cathode and anode materials, and through adjusting the composition, could also be employed as a solid electrolyte material, creating an all-PBA solid-state battery. This chapter investigates the

prospect of using sodium zinc hexacyanoferrate as a solid electrolyte material. The crystal structure, ionic conductivity, and other relevant properties of sodium zinc hexacyanoferrate are studied as a function of densifying pressure and water content. An optimum sodium zinc hexacyanoferrate composition is identified and the possibility of utilising it as a solid electrolyte is discussed.

6.2 Introduction

Development of solid-state batteries is currently one of the most active areas of battery research.[171] In these batteries the conventional liquid electrolyte is replaced with a solid, whether inorganic or polymer. The motivation for this research is two fold; improving safety by removing the flammable organic electrolyte, and enabling the use of a metal anode which increases energy density. In conventional liquid electrolytes metallic anodes cannot be used as they form dendrites that short circuit the battery.

There are a number of challenges in the development of solid electrolytes and their integration into solid-state batteries.[171,172] Firstly, there are restrictions on the solid electrolyte materials themselves which include high ionic conductivity, low electronic conductivity, and a wide electrochemical stability window or formation of passivating layers when in contact with cathode and anode materials, much like solid electrolyte interphases (SEIs) in conventional batteries. Secondly, the interface between the solid electrolyte and electrode materials must be low impedance and maintained during cycling. Electrode materials undergo volume changes which can quickly cause cracking and loss of contact between the solid electrolyte and electrode materials. Thirdly, solid state batteries must be manufacturable. Mature and highly productive battery manufacturing used for current lithium-ion batteries will most likely be inappropriate for solid state batteries and therefore alternative, but cost competitive, manufacturing procedures must be developed.

Prussian blue analogues offer a unique opportunity in the development of solid-state batteries. PBA electrode materials undergo relatively small volume changes during electrochemical cycling[62] and are mechanically soft which could help maintain interfaces within the battery. They have a wide composition space that enables tuning of the electrochemical and electronic properties. One could, in principle, develop and all-PBA solid state battery in which the cathode, anode, and solid electrolyte are PBAs.

This chapter focuses on the identification and characterisation of a PBA material suitable for use as a solid electrolyte. The initial considerations are that the PBA material has a wide electrochemical stability window and low electronic conductivity. A d^6 (t_{2g}^6) electronic configuration for the R site transition metal is desired to ensure electrochemically stability over a wide potential range. Therefore, $Fe(CN)_6^{4-}$ and $Co(CN)_6^{3-}$ are appropriate candidates. Since most PBAs are mixed conductors ensuring low electronic conductivity will be most likely be achieved by using a P site with a filled d orbital (d^{10}, t_{2g}^6 e_g^2). Therefore, Zn^{2+} appears to be the most suitable P site transition metal. Zn^{2+} is stable against oxidation and has a standard reduction potential of $-0.76\,\mathrm{V}$ vs. SHE.

Due to no crystal field stabilisation Zn^{2+} typically takes tetrahedral coordination, over octahedral coordination, which means, when reacted with a hexacyanometallate complex, materials with unconventional structures are formed.[173] They are no longer structural analogues of Prussian blue, but do behave in a similar manner. These rhombohedral structures are formed of ZnN_4 tetrahedra and RC_6 octaedra, which are bonded through the cyanide ligand, see Figure 6.1.[174] Within the structures are 'cavities' which can accommodate alkali cations and solvent molecules. The stoichiometric formula is $A_xZn_3[R(CN)_6]_2$ (A = alkali cations) and the structure does not contain hexacyanometallate vacancies. In fact, the structure is analogous to NASICON, the well-known sodium-ion superionic conductor.[175,176] The primary

difference is larger lattice parameters, and correspondingly larger cavitites, due to the CN^- replacing the O^{2-} bridging ligands.

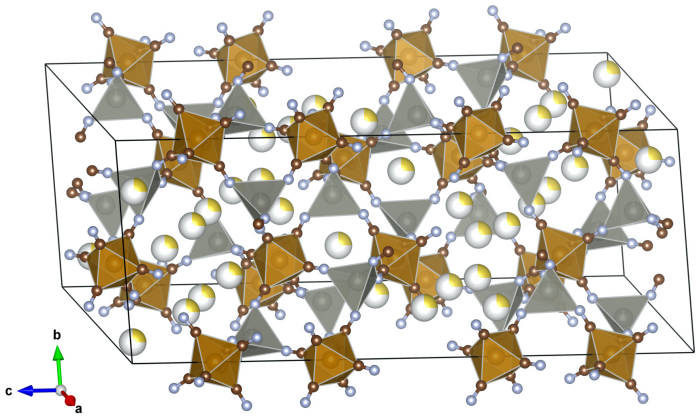


Figure 6.1: Crystal structure of sodium zinc hexacyanoferrate(II) with the space group R-3c consisting of ZnN_4 tetrahedra, FeC_6 octaedra, and sodium ions within cavities. Water molecules omitted for clarity.

The two possible compositions are $Na_2Zn_3[Fe(CN)_6]_2$ and $Zn_3[Co(CN)_6]_2$ which differ due to charge neutrality constraints. The requirement for sodium-ion conductivity prevents the use of $Zn_3[Co(CN)_6]_2$ as a high concentration of charge carriers in the material is required. Therefore, $Na_2Zn_3[Fe(CN)_6]_2$ appears to be the most promising candidate as a solid electrolyte material.

The structure of sodium zinc hexacyanoferrate(II) (NaZnHCFe) and related compounds have been investigated and reported previously, see Figure 6.1. The structure of NaZnHCFe was first resolved by Garnier et al. and takes the space group R-3c.[174] The ellipsoidal cavities are approximately 12.5 by 9 by 8 Å and contain mobile charge balancing ions which are hydrated by water molecules. As sodium is a small alkali cation, and so highly polarising, there are a large number of water molecules in its immediate hydration sphere and subsequently hydrogen bonded, around 9 per formula unit. For larger alkali cations there are fewer less strongly bound water molecules.[173]

Extensive work by Reguera and coworkers have characterised a large number of rhombohedral transition metal hexacyanometallates, and specifically the effect of composition on structure and ionic mobility.[173,177,178] Alkali metal zinc hexacyanoferrate(II)

compounds undergo a structural transition on dehydration from the rhombohedral phase (R-3c) to a monoclinic phase (P2/c).[177] This is due to reduced shielding of the alkali metal charge which allows greater interaction with the negative charged N ends of the CN^- ligands, inducing a phase transformation. It was found previously that removal of water molecules significantly reduce the activation energy for sodium mobility and the lowest activation energy was found for the anhydrous monoclinic phase.

In this chapter sodium zinc hexacyanoferrate will be evaluated as a solid electrolyte material. Hydration level - stucture - property relationships will be investigated to study and optimise properties relevant for its application as a solid electrolyte.

6.3 Experimental methods

Sodium zinc hexacyanoferrate(II) (NaZnHCFe) was synthesised from a simple coprecipitation synthesis procedure. 60 mmol dm^{-3} $ZnCl_2$ solution was added in a dropwise manner to an equal volume of 40 mmol dm^{-3} $Na_4Fe(CN)_6$ under stirring at 60 °C. Both solutions contained 1 mol dm^{-3} NaCl. After a few drops was added the precipitate started to form and the solution quickly turned cloudy. The dropwise addition typically took 2 - 3 hours and the resultant mixture was stirred for an additional 4 hours and then aged for 48 hours. To recover the precipitate the solution was centrifuged and washed with deionised water three times. The powder was dried in air at 75 °C overnight.

NaZnHCFe samples were dehydrated in a Buchi glass oven under vacuum at the specified temperature overnight. Once dehydrated samples were stored, handled, and characterised in argon and nitrogen-filled glove boxes without exposure to air.

Samples were characterised using the same techniques that were described in Chapter 3.

The solid-state impedance cell (Figure 2.6) was prepared by pouring in a pre-weighed amount of NaZnHCFe powder into the cell. The powder was then densified under pressure using a press inside the glove box. To hold the O-rings closed the cell was placed inside the external cage and pressure applied from turning the screws. The cell was then taken outside the glove box for various measurements, both under pressure inside a different press or under the pressure applied by the screws alone. The typical frequency range used for EIS measurements was from 13 MHz to 1 Hz. DC polarisation and linear sweep voltammetry measurements on NaZnHCFe were also performed using the solid-state impedance cell.

6.4 Results and discussion

6.4.1 Physiochemical characterisation

As-synthesised NaZnHCFe particles were primarily between 500 nm and 1 µm in size and approximately cubic, Figures 6.2a - c. As in the synthesis of manganese hexacyanochromate there was no visible precipitation on the addition of the first few drops of $ZnCl_2$ solution. Nucleation of NaZnHCFe particles occurred once the concentration of precursors were sufficiently high. Following this nucleation event there was no secondary nucleation, and existing particles grew as additional precursor solution was added. EDX mapping shows a uniform distribution of sodium, zinc, and iron across a single particle, Figures 6.2d - g.

High-resolution synchrotron XRD of the as-synthesised material was measured and refined using the Rietveld method, Figure 6.3. The material was found to be phase pure and refined unit cell parameters were consistent with previous reports of this material.[174] Results from the Rietveld refinement can be found in Table 6.1 and shown schematically in Figure 6.1. The starting crystal structure model was taken from previously published data.[174] All refinement parameters were allowed to relax,

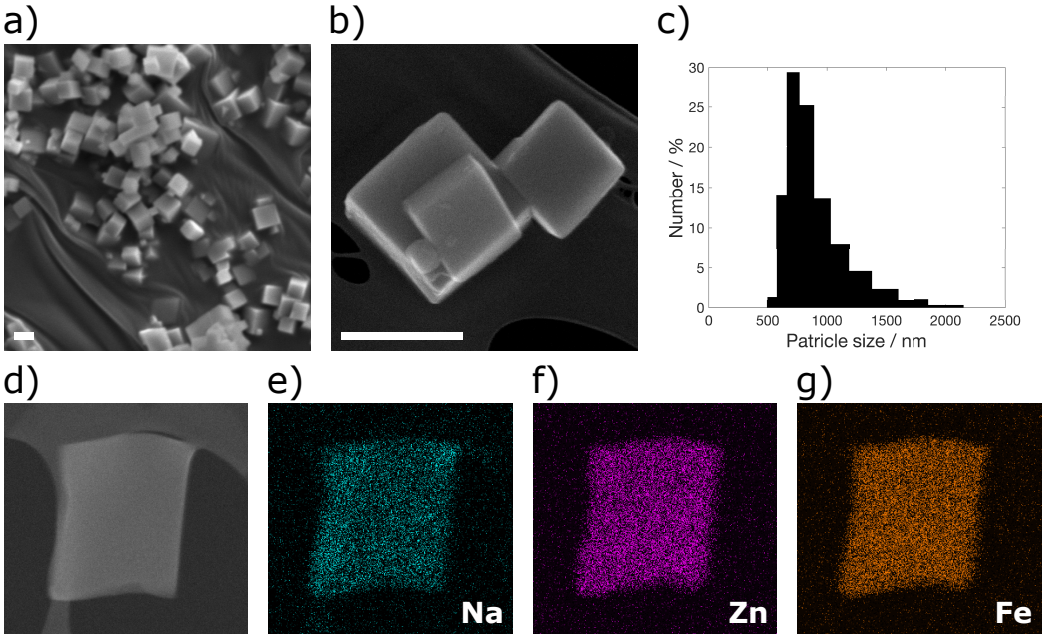


Figure 6.2: Characterisation of the morphology and particle size of as-synthesised NaZnHCFe. a) and b) scanning electron micrographs of NaZnHCFe with a scale bar of 500 nm. c) Particle size distribution from dynamic light scattering measurements. d) - g) EDX mapping of a single NaZnHCFe particle.

apart from the occupancy of Fe, C, and N sites. The occupancy of a fifth oxygen site decreased towards zero and even went negative, so was removed from the model. Final refinement parameters were in close agreement with previously reported values. Occupancies of oxygen sites differed the most and their displacement parameters were large. This is expected as sodium ions and hydrogen bonded water molecules are disordered within the cavities.

Fourier-transform infrared (FTIR) spectrum of the as-synthesised material contains peaks associated with v(Fe-C) at 492 cm^{-1}, δ(Fe-CN) at 604 cm^{-1}, $\delta(H_2O)$ at 1616 cm^{-1}, v(CN) at 2085 cm^{-1}, and v(OH) from 3350 to 3700 cm^{-1}, Figure 6.4a.[173]

Thermogravimetric analysis of the as-synthesised material shows an approximately linear decrease in mass between room temperature and 220 °C which can be associated with loss of water from the material, as seen in the mass spectrometry trace, Figure 6.4b. The wide temperature window in which water is lost from the material, rather than

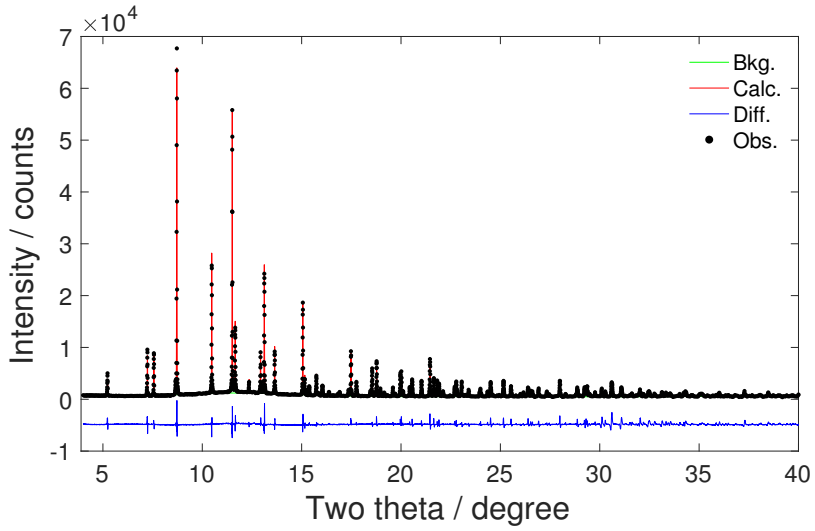


Figure 6.3: High-resolution synchrotron X-ray diffraction pattern of as-synthesised NaZnHCFe with Rietveld refinement fit and residual.

at a single temperature, is informative and consistent with water in different bonding environments. The most loosely bound water is lost first, and as the temperature is increased more and more water is released. From the mass loss it can be calculated that the number of water molecules per formula unit is approximately 6.5, giving the chemical formula as $Na_2Zn_3[Fe(CN)_6]_2 \cdot 6.5\,H_2O$. Above 220 °C HCN is evolved from the material and above 250 °C there is CO_2 observed. These gases are associated with thermal decomposition of the material.

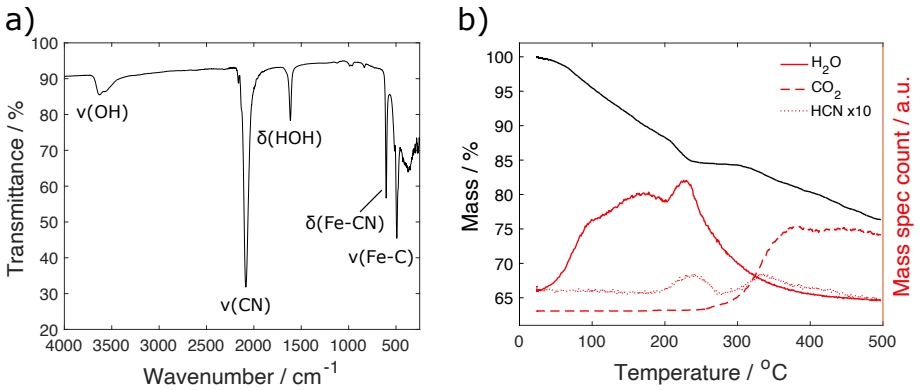


Figure 6.4: a) FTIR spectrum and b) TGA-MS data of as-synthesised NaZnHCFe.

Atom	Site	g	x	y	z	U_{iso} / Å^2
Fe	12c	1	0	0	0.14689(10)	0.0310(10)
Zn	18e	0.9810(29)	0.28932(18)	0	0.25	0.0397(7)
C(1)	36f	1	0.1152(9)	-0.0125(11)	0.18291(33)	0.056(5)
N(1)	36f	1	0.1790(7)	-0.0296(9)	0.20109(29)	0.076(5)
C(2)	36f	1	0.1426(11)	0.1215(11)	0.1147(4)	0.072(6)
N(2)	36f	1	0.2093(9)	0.1871(8)	0.09477(29)	0.078(5)
Na	36f	0.241(7)	0.4497(18)	0.3536(20)	0.3050(7)	0.053(10)
O(1)	36f	0.253(12)	0.3905(33)	0.292(4)	0.3347(13)	0.180(26)
O(2)	36f	0.871(12)	0.3524(14)	0.3341(13)	0.2838(4)	0.369(12)
O(3)	36f	0.256(7)	0.5816(20)	0.4279(21)	0.3280(9)	0.002(9)
O(4)	36f	0.551(8)	0.5644(13)	0.3374(20)	0.3017(5)	0.170(11)

Table 6.1: Structural parameters of as-synthesised NaZnHCFe from Rietveld refinement in the space group R-3c. Occupancy g, atomic positions (x, y, z), and isotropic atomic displacement U_{iso} are given. The X-ray wavelength was $\lambda = 0.826\,03$ Å. Lattice parameters a and b were $12.525\,22(8)$ Å, and c was $32.830\,71(28)$ Å. Oxygen takes many positions within the cavities. $R_P = 10.73\%$, $R_{WP} = 15.67\%$, reduced $\chi^2 = 37.55$, GOF = 6.13.

6.4.2 Measurement of ionic conductivity

As a candidate solid electrolyte material the ionic conductivity must be measured and maximised. Previous work on measuring the ionic conductivity of alkali metal zinc hexacyanoferrate(II) materials has given mixed and contradictory results.[178] This is most likely due to experimental inconsistency in two areas. Firstly, relative humidity can alter the water content of the NaZnHCFe for a given temperature, and after partial dehydration the material rapidly rehydrates when exposed to air. Secondly, due to the low thermal stability the material cannot be sintered to form a dense pellet, unlike metal oxides for example. Instead cold pressing alone was employed without optimisation of the densifying pressure or ensuring once the pressure is released interparticle contact is maintained.

In this study the water content is adjusted by dehydrating the material under vacuum, and temperature is employed as the independent variable. After dehydration the material is transferred and stored under inert atmosphere to avoid rehydration

and characterised the same day. In addition, an impedance cell was designed and built, detailed in Section 2.3.2. The function of this cell is to act as both the die set to densify the pellet and also the impedance cell. O-rings are used to seal the cell from atmosphere and an external cage is built to apply a small pressure to seal the O-rings and maintain good contact between electrodes and pellet, and within the pellet when the EIS measurements are being performed.

The basics of impedance measurements and fitting to equivalent circuits are detailed in Section 2.3.6. Literature provides further guidance on how to model sodium zinc hexacyanoferrate specifically. Jamnik et al., and others, have modelled the impedance spectra of a mixed conductor in which the electrodes are blocking to one of the charge carriers and nonblocking to the other.[179–182] Typically, electrodes are blocking to ions and nonblocking to electrons, as in the case of NaZnHCFe. These works explain under what conditions the impedance response at low frequencies of such systems give rise to Warburg diffusion, a vertical capacitive tail, or a semicircle. A transmission line equivalent circuit was found to provide a good approximation to the model. Simplifications to this equivalent circuit can be made in certain cases. Assuming the resistance of the nonblocked charge carrier (electrons) is much higher than the resistance of the blocked charge carrier (ions) the equivalent circuit can be simplified (see Figure 3b of ref[179] and Figure 4a of ref[182]). A modified version of this simplified equivalent circuit can be found in Figure 6.5b and is used in the analysis of NaZnHCFe impedance spectra.

Figure 6.5 shows a typical Nyquist plot of NaZnHCFe impedance data and fit to the equivalent circuit. The Nyquist plot for other measurements in which the low frequency limit was reduced to 0.005 Hz shows no deviation from linear behaviour at low frequencies. Resistance R1 was added to account for other resistances in series in the experimental set up and was typically around 10 Ω. R2 corresponds to the ionic conductivity of NaZnHCFe, assuming that electronic conductivity is negligible

in comparison. Q1 is from the geometric capacitance. Q2 and Q3 are constant phase elements representing interfacial capacitance of the ions and a non-ideal Warburg element corresponding to diffusion. In the version of the equivalent circuit found in literature an ideal Warburg element was used, however, in the analysis of NaZnHCFe impedance data a constant phase element better fit the data.[179,182] Attempts to remove equivalent circuit elements or reduce degrees of freedom resulted in much poorer fits and therefore this equivalent circuit is considered reasonable for the system. Fitting parameters for this data are in Table 6.2. The same data displayed as Bode plots is shown in Figure 6.6. The region above 10^5 Hz is where effects from the bulk ionic conductivity can be observed, whereas the region below 10^4 Hz is where diffusion effects can be seen.

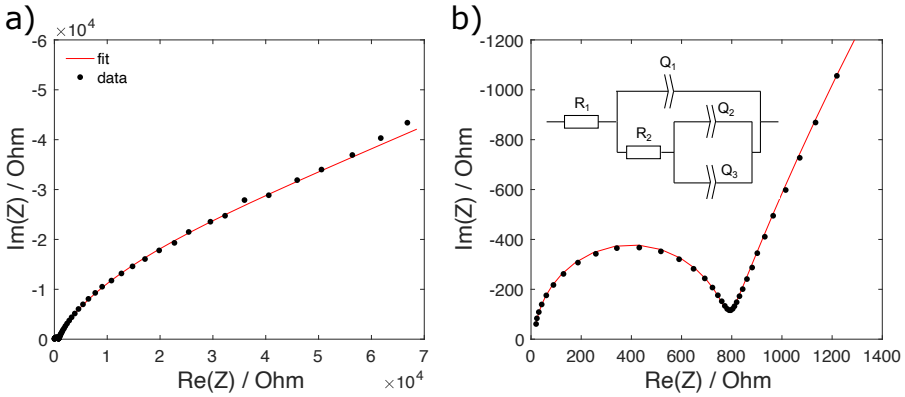


Figure 6.5: Typical Nyquist plot and equivalent circuit fit for a NaZnHCFe sample in the frequency range from 13 MHz to 1 Hz. Data is plotted a) for the whole data set and b) with restricted x and y axes. The equivalent circuit is shown inset.

Parameter	Value	Unit	Error
R1	14.24	Ohm	0.6622
Q1	2.203×10^{-10}	F $s^{\alpha-1}$	9.458×10^{-12}
α (Q1)	0.9898	no units	0.5666
R2	766.3	Ohm	0.2692
Q2	7.106×10^{-6}	F $s^{\alpha-1}$	6.816×10^{-10}
α (Q2)	0.2934	no units	0.5001
Q3	4.597×10^{-7}	F $s^{\alpha-1}$	1.649×10^{-10}
α (Q3)	0.8039	no units	0.5001

Table 6.2: Fitting parameters for data shown in Figure 6.5.

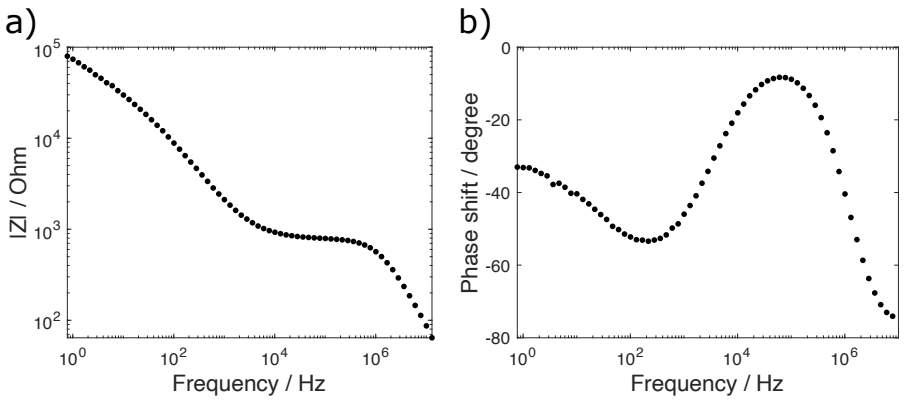


Figure 6.6: Typical Bode plots for a NaZnHCFe sample in the frequency range from 13 MHz to 1 Hz. Data is plotted a) with absolute magnitude of impedance on the y axis and b) with phase shift on the y axis.

The low frequency tail corresponds to a diffusion process that leads to stoichiometry polarisation as ions, the more mobile charge carrier, are block by the electrodes whereas electrons are not blocked.[182] Fitted values of Q1, Q2, and Q3 will not be used in further analysis, however, information relating to diffusion of charge carriers and partial conductivities could, in principle, be derived. More thorough consideration of the low frequency behaviour of NaZnHCFe is warranted and could reveal additional information about the material.

The high frequency semicircle corresponds to ionic conductivity and the fitted values of R2 are used, in combination with geometry of the pellet, to calculate the ionic conductivities of NaZnHCFe for the remainder of this work. This method has the inherent problem that the thickness of the pellet cannot be measured in situ as the EIS measurement is being performed. For measurements in this thesis the thickness of the pellet was measured after breaking the pellet out of the die set after EIS measurements were taken.

Errors in the values of R2 used to calculate ionic conductivities are non-trivial to evaluate. The fitting program provides an error on values of R2 but the real value is much larger. Goodness of fit values consider all parameters and all data points which include the diffusion tail which is fit less well in general. To ensure reasonable values

of R2 the fits of the high frequency semicircle were visually inspected to confirm a good match between experimental data and the model, as is seen in Figure 6.5.

6.4.3 Optimisation of ionic conductivity

Dehydration temperature and densifying pressure are two variables that must be optimised. They can broadly be considered independent to one another.

6.4.3.1 Effect of applied pressure

The densifying and operating pressure were optimised using NaZnHCFe dried under vacuum at 90 °C, termed NaZnHCFe-90. To study the effect of pressure on the ionic conductivity of NaZnHCFe-90 EIS measurements were taken at a series of applied pressures. The applied pressure was increased in steps from 50 to 600 MPa, with periodic measurements taken at 50 MPa. This series of pressures is most easily understood from Figure 6.7, plotted alongside corresponding ionic conductivity values. As the pressure is increased the ionic conductivity first increases a small amount, from 50 to 100 MPa, then consistently decreases with increasing applied pressure. The ionic conductivity value for 600 MPa is only 23% that of 100 MPa. Interestingly, the ionic conductivity consistently increased after the pressure was decreased, for example when the pressure was decreased from 200 to 50 MPa. In fact this was the densifying and operating pressure that gave the maximum ionic conductivity. Densifying at higher pressures than 200 MPa and keeping the same operating pressure resulted in lower conductivities.

The most appropriate interpretation of this data is that an applied pressure of at least 100 MPa is required to successfully densify the pellet, and pressures higher than 200 MPa alter the material in some manner that decreases the conductivity. Additionally, the conductivity of the material decreases when pressure is applied, most likely due to contraction of the unit cell lattice parameters and constriction

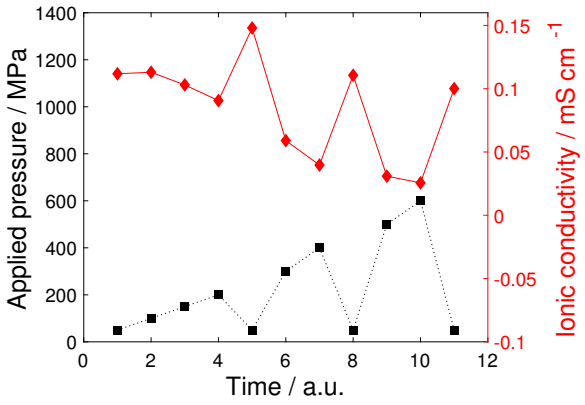


Figure 6.7: Plot of ionic conductivity of NaZnHCFe-90 for a series of applied pressures.

of sodium-ion diffusion channels. It was found that the specific value of operating pressure was unimportant, as long as it was non-zero and not very high. Subsequent measurements reported in this thesis used a densifying pressure of 200 MPa and a low operating pressure.

To study the impact on the crystal structure of applied pressure samples of NaZnHCFe were pressed into pellets are a series of pressures up to 600 MPa. They were then reground and mixed in a mass ratio of 5:1 (NaZnHCFe:Si) with Si powder which acted as an XRD internal standard. XRD patterns of these samples are reported in Figure 6.8, normalised by the height of the Si XRD reflection at 47°. It appears that the material undergoes pressure induced amorphisation, characterised by decreasing height and increasing full-width half-maximums of the XRD reflections. This can arise from either decreasing domain size or an increase in microstrain. It appears that this amorphisation is irreversible (with applied pressure) and reduces the ionic conductivity of the material. This behaviour is similar to other sodium-ion conducting zeolite materials.[183]

6.4.3.2 Effect of dehydration temperature

It is well known that partial or full dehydration of this class of materials can induce changes in both structure and ionic conductivity. On full dehydration the materials

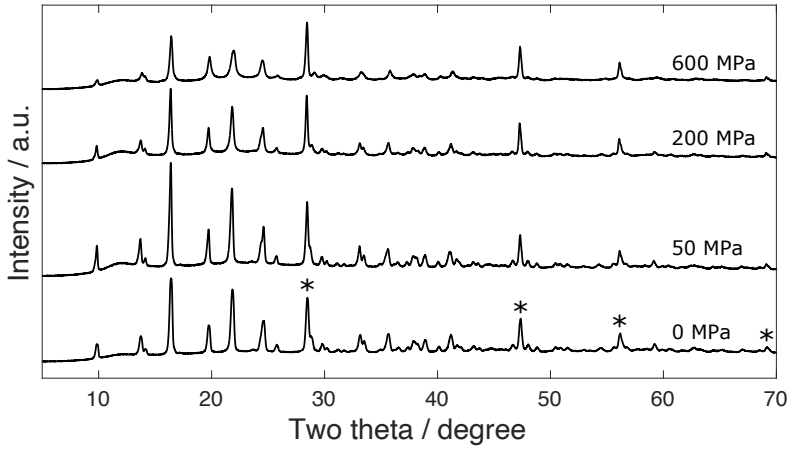


Figure 6.8: XRD patterns of NaZnHCFe samples after densification at a series of pressures. Samples are reground and mixed with Si powder to act as an internal XRD standard. * indicates Si XRD reflections.

undergoes a phase transition from rhombohedral (R-3c) to monoclinic (P2/c).[177] Previous impedance studies on NaZnHCFe reported that the anhydrous compound exhibited the highest ionic conductivity.[178]

A series of NaZnHCFe samples were prepared by heating under vacuum at a range of temperatures. Figure 6.9a shows the ionic conductivities as a function of drying temperature. With increasing drying temperature there is a moderate increase in conductivity until around 100 °C; at higher temperatures the conductivity decreases multiple orders of magnitude. The maximum ionic conductivity was for sample NaZnHCFe-90. The same NaZnHCFe samples were investigated using XRD and FTIR, Figures 6.9b and c. XRD patterns show this discontinuity in conductivity is concurrent with the phase change from rhombohedral to momoclinic. NaZnHCFe-110 is a mixture of the two phases and NaZnHCFe-140 is monoclinic single phase. FTIR patterns similarly show changes due to the phase transition. The absorption bands at around 500 cm^{-1} and 2100 cm^{-1}, corresponding to v(Fe-C) and v(CN) respectively, show many more distinguishable peaks from more distinct Fe-C-N bonding environments contained in the lower symmetry monoclinic phase. The water content is estimated from the ratio of absorption band areas between $\delta(H_2O)$ at around 1616 cm^{-1} and

v(CN) at around 2100 cm^{-1}. The calculated water contents, normalised by the water content of the as-synthesised material calculated from mass loss in TGA, is plotted in Figure 6.9d. Approximately half the water is removed by drying the material at 110 °C, before the phase change is induced, and results in the material with highest ionic conductivity.

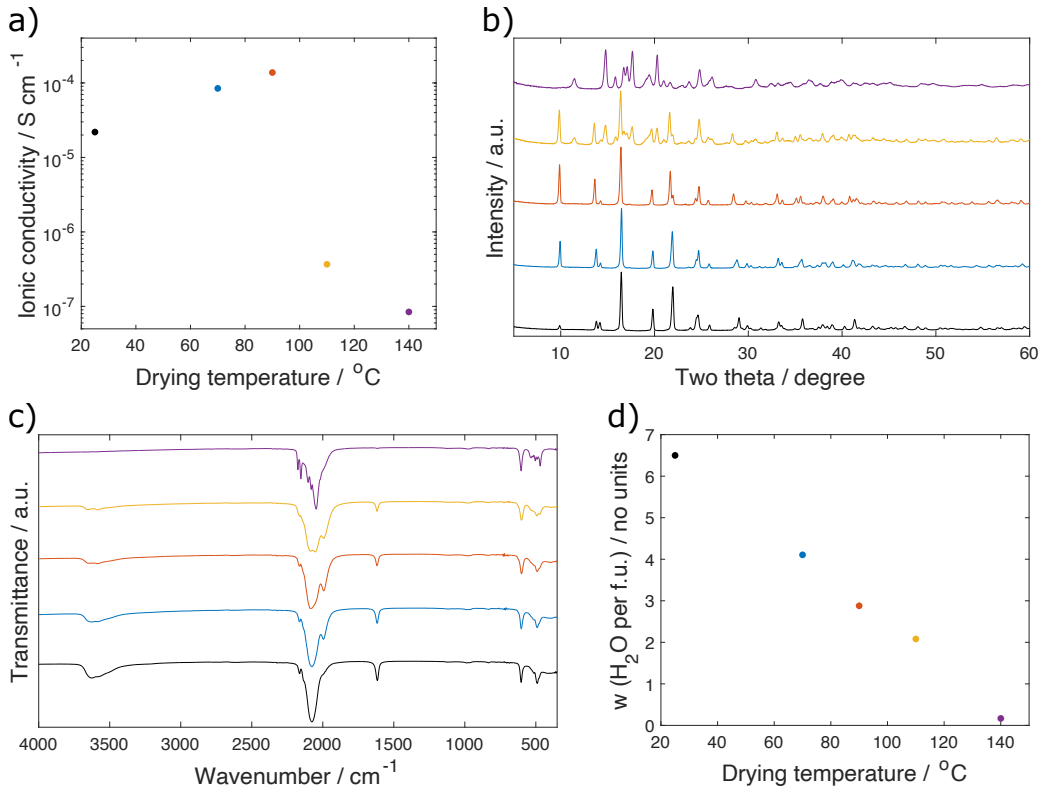


Figure 6.9: Impact of dehydration temperature on the a) ionic conductivity, b) XRD pattern, c) FTIR spectra, and d) water content per formula unit of NaZnHCFe. Colours indicate sample dehydration temperatures.

Synchrotron XRD was performed on a partially dehydrated NaZnHCFe material to study in more detail the changes in structure induced by partial dehydration. Although, the data is not of the optimised material it remains informative. Figure 6.10 presents the XRD pattern, Rietveld refinement fit and residual. Parameters from the Rietveld refinement can be found in Table 6.3. Compared to the as-synthesised material the lattice parameters are reduced, but only by 0.17% and 0.07% for lattice parameters a and c respectively. Although this is difficult to display graphically the

most significant difference is in the location of sodium ions. In the partially dehydrated material they are closer to the zinc and iron framework ions, and closer to sodium sites in neighbouring cavities. This is likely due to less shielding from the reduced number of water molecules per formula unit. Further reduction in water molecules induces the rhombohedral to monoclinic phase transition.[177]

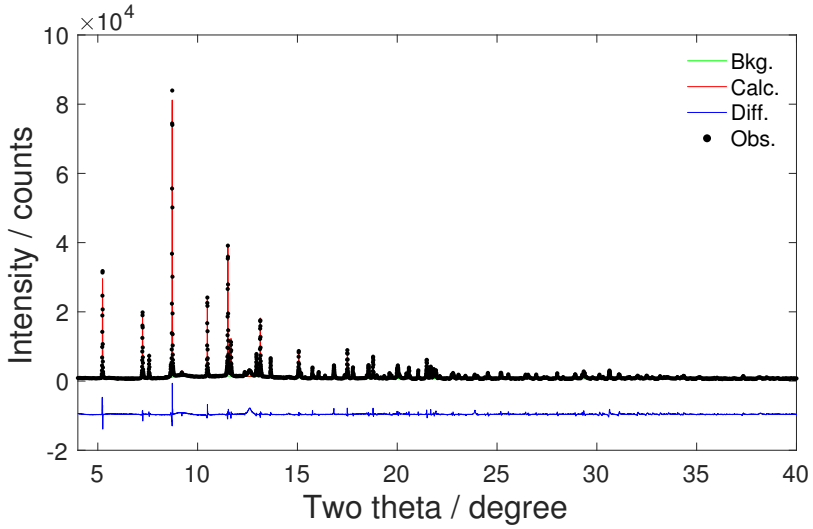


Figure 6.10: High-resolution synchrotron X-ray diffraction pattern of partially dehydrated NaZnHCFe with Rietveld refinement fit and residual.

6.4.3.3 Activation energy

To measure the temperature-dependent ionic conductivity, and to calculate the activation energy for sodium mobility, EIS measurements were performed at temperatures between 10 and 70 °C on NaZnHCFe-90. A Nyquist plot of this data is presented in Figure 6.11a. Figures 6.11b and c show the calculated ionic conductivity values plotted in its natural log form against inverse temperature and in its log form against temperature. The linear dependence with respect to inverse temperature indicates that the ionic conductivity is a thermally activated process that can be modelled using the Arrhenius equation. The Arrhenius relationship is as follows

Atom	Site	g	x	y	z	U_{iso} / Å^2
Fe	12c	1	0	0	0.14689(10)	0.0335(11)
Zn	18e	0.862(4)	0.28865(21)	0	0.25	0.0232(8)
C(1)	36f	1	0.1126(10)	-0.0240(11)	0.18477(34)	0.038(5)
N(1)	36f	1	0.1772(8)	-0.0321(10)	0.20617(32)	0.060(5)
C(2)	36f	1	0.1350(10)	0.1083(11)	0.1136(4)	0.052(5)
N(2)	36f	1	0.2259(9)	0.1953(10)	0.09667(29)	0.071(5)
Na	36f	0.454(11)	0.2375(17)	0.3009(16)	0.3147(6)	0.246(14)
O(1)	36f	0.440(21)	0.408(4)	0.297(4)	0.3519(13)	0.49(4)
O(2)	36f	0.362(11)	0.3645(26)	0.3885(26)	0.2658(9)	0.166(19)
O(3)	36f	0.283(9)	0.6004(27)	0.4100(27)	0.3302(12)	0.048(14)
O(4)	36f	0.331(17)	0.481(4)	0.281(5)	0.2852(16)	0.34(4)

Table 6.3: Structural parameters of partially dehydrated NaZnHCFe from Rietveld refinement in the space group R-3c. Occupancy g, atomic positions (x, y, z), and isotropic atomic displacement U_{iso} are given. The X-ray wavelength was $\lambda = 0.826\,03$ Å. Lattice parameters a and b were $12.503\,41(11)$ Å, and c was $32.8072(4)$ Å. Oxygen takes many positions within the cavities. $R_P = 9.21\%$, $R_{WP} = 13.05\%$, reduced $\chi^2 = 30.54$, GOF = 5.53.

$$ln(\sigma.T) = -\frac{E_a}{k}\frac{1}{T} + ln(\sigma_0) \tag{6.1}$$

where σ is conductivity, σ_0 is the pre-exponential factor, E_a is activation energy, and the other parameters take their usual meanings. The activation energy was calculated to be $30.9\,\mathrm{kJ\,mol^{-1}}$ or $0.321\,\mathrm{eV}$, from a line of best fit with an R^2 value of 0.998. This is low when compared to other sodium-ion conductors such as NASICON which has a room temperature activation energy of $\approx$0.25 eV.[184] The room temperature ionic conductivity of NaZnHCFe-90 is $\approx 10^{-4}\,\mathrm{S\,cm^{-1}}$ and reaches a conductivity of $10^{-3}\,\mathrm{S\,cm^{-1}}$ at 60 °C.

As discussed previously the errors on the conductivity values are difficult to evaluate given the fitting process. In addition, for high temperature measurements the number of data points which make up the high frequency semicircle decreases considerably and only part of the semicircle is mapped. All fits were visually inspected to ensure reliable R2 values.

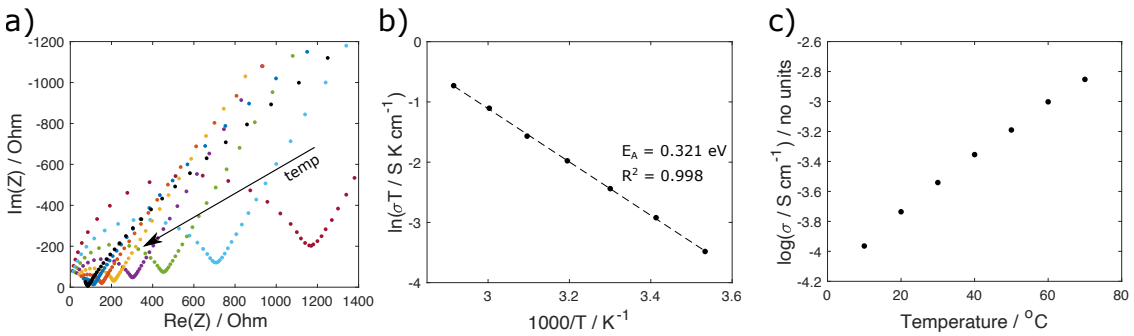


Figure 6.11: a) Nyquist plot of impedance data for NaZnHCFe-90 every 10 °C in the temperature range from 10 to 70 °C. Corresponding a) Arrhenius plot of the natural log of conductivity against inverse temperature and b) log of conductivity against temperature.

6.4.4 Electronic conductivity

For a solid electrolyte material it is also crucial that the electronic conductivity is minimal, and several orders of magnitude lower than its ionic conductivity. The electronic structure of the PBA composition was designed specifically to reduce electronic conductivity by using Zn^{2+} in the P site, an ion with filled d-orbitals. A DC polarisation technique was used to investigate the electronic conductivity. This method applies a constant voltage (in this case 1 V) to the sample whilst still in the impedance cell and under the operating pressure. The current starts very high but quickly falls and approaches the steady state value in a few minutes, Figure 6.12. The initial current is due to both ionic and electronic conductivity, but because the electrodes are blocking electrodes the contribution to total conductivity from ion mobility quickly reduces towards zero. The initial current is much higher than 20 µA cm^{-2} but the y axis is reduced for clarity in Figure 6.12a.

The steady state current can easily be converted to a conductivity using Ohm's law. It can be seen that the fully hydrated material has the highest electronic conductivity, with a significant reduction for NaZnHCFe-90 and further reduction for NaZnHCFe-110. The electronic conductivity for NaZnHCFe-90 was calculated to be 5.6×10^{-9} S cm^{-1} from a steady state current of 0.32 µA cm^{-1}. This is more than 10^4 times lower than

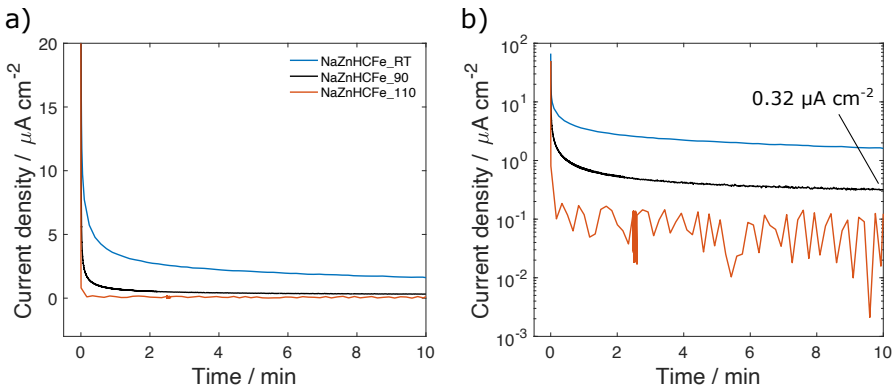


Figure 6.12: DC polarisation data of three NaZnHCFe samples prepared with different dehydration temperatures plotted with a) linear and b) log y axes. The steady state current for sample NaZnHCFe-90 is labelled.

its ionic conductivity.

6.4.5 Electrochemical stability

Another crucial characteristic of a solid electrolyte material is the electrochemical stability window, the voltage range in which the material is electrochemically stable against reduction and oxidation. In a functioning battery both the anode and cathode must be within this voltage window or passivating layers must form.

NaZnHCFe is unconventional as a candidate solid electrolyte material as both water in the material and the framework of the material can be oxidised and reduced. Due to the narrow thermodynamic window of stability of water this likely results in a narrow electrochemical stability window.

The electrochemically stability was first investigated using linear sweep voltammetry (LSV), see Figure 6.13. In the same impedance cell the voltage polarisation is increased, at a scan rate of $5\,\mathrm{mV\,s^{-1}}$, and the current measured. There is no consensus on what current density is defined as the 'limit' of stability, but for the purpose of this study using a current density limit of $2\,\mu\mathrm{A\,cm^{-2}}$ gives voltage limits of 1.00 V, 2.11 V, and 2.96 V for NaZnHCFe-RT, NaZnHCFe-90, and NaZnHCFe-110, respectively. Clearly, the weakly bound water is responsible the current at around 1.30 V for NaZnHCFe-RT.

Removal of this water raises the voltage limit to around 2.2 V, as seen for NaZnHCFe-90. Further dehydrating the material the voltage limit is raised further as seen for NaZnHCFe-110.

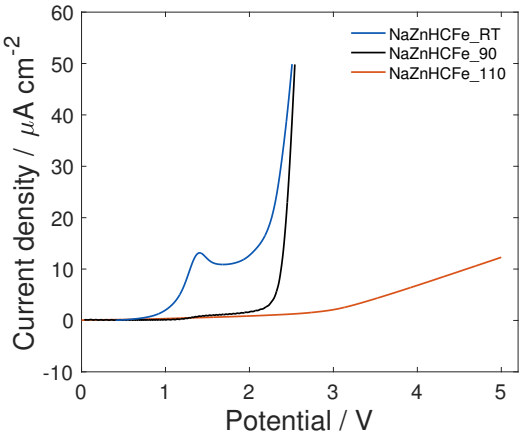


Figure 6.13: Linear sweep voltammetry scans of three NaZnHCFe samples prepared with different dehydration temperatures.

LSV is a good initial characterisation technique but does not give us all the information, for example in what voltage range, compared to a reference, the material is electrochemically stable. Although unlikely, the stability of NaZnHCFe-90 against metallic sodium was investigated. Most solid electrolyte materials are not thermodynamically stable against lithium or sodium but, instead, the interface is kinetically stabilised. The interface is studied using a Na|NaZnHCFe-90|Na symmetric cell. Figure 6.14 shows the Nyquist plot of EIS measurements taken when the cell is initially built and after a series of time intervals up to 800 minutes. The impedance from the high-frequency semi circle, attributed to bulk NaZnHCFe conductivity, does not increase significantly throughout the experiment. On the other hand, the second semicircle continues to grow throughout. This semicircle is attributed to interfacial impedance, indicating an inherently non-passivating interface is formed between NaZnHCFe and sodium metal.

NaZnHCFe can also be employed as a cathode material in sodium- and potassium-ion batteries with a redox potential within the stability window of water. Therefore,

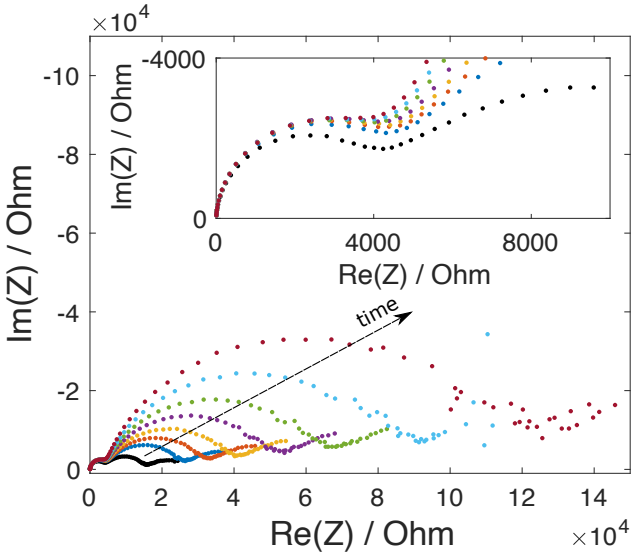


Figure 6.14: Nyquist plot of a Na|NaZnHCFe-90|Na symmetric cell after 0, 13, 25, 50, 100, 200, 400, and 800 minutes, in the frequency range from 13 MHz to 0.1 Hz. Inset shows the same data with restricted x and y axes.

it is appropriate to assume the current from oxidisation of the material observed in LSV measurements is from the $Fe(CN)_6^{4/3-}$ redox couple. Concurrent reduction of the material must be from reduction of water in the structure or reduction of the framework of the material itself. To study the limits of oxidation and reduction of NaZnHCFe, compared to a reference electrode, it was operated as a cathode in a three-electrode non-aqueous cell. The electrolyte was 1 M $NaClO_4$ in PC.

Figure 6.15 presents the galvanostatic profile and differential capacity plot of a full charge and discharge cycle. The discharge continues until a deflection in the discharge profile is observed, indicating a species in the cell is being reduced. The onset of oxidation and reduction are 3.25 and 1.1 V vs. Na^+/Na, respectively, giving a electrochemical stability window of approximately 2.15 V. This is above the expected onset of reduction of the electrolyte.

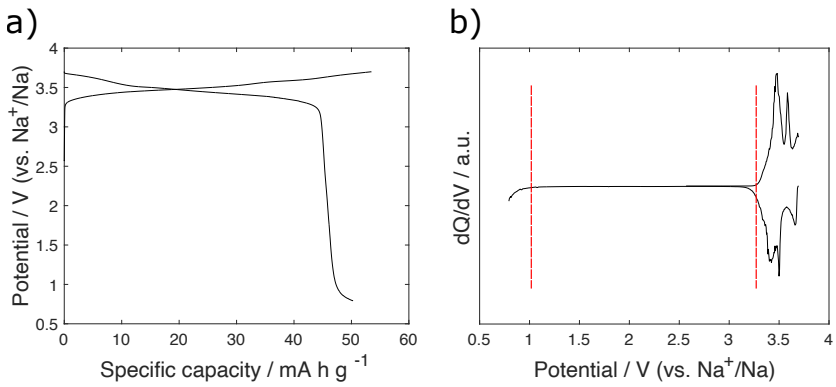


Figure 6.15: a) Galvanostatic cycling profile and b) corresponding dQ/dV plot of NaZnHCFe operated as a cathode in a nonaqueous electrolyte. Onset of oxidation and reduced are marked on the dQ/dV plot.

6.5 Conclusions

In conclusion, the suitability of sodium zinc hexacyanoferrate(II) (NaZnHCFe) as a solid electrolyte was investigated. For optimum ionic conductivity NaZnHCFe needed to be densified at around 200 MPa, to ensure high tap density but avoid significant amorphisation of the material, and operated at a low but non-zero pressure, to maintain interparticle contact. Partial dehydration, removal of approximately half the water molecules, resulted in an increase in ionic conductivity due to less shielding of the sodium ions enabling higher mobility. Further dehydration induced a phase transformation which significantly reduced the ionic conductivity. The partially dehydrated material had low electronic conductivity and a electrochemical stability window of around 2.2 V.

Further work should focus on fabricating a proof of concept solid-state cell using NaZnHCFe as the solid electrolyte material. Anode and cathode materials must be electrochemically active within the electrochemical stability window of NaZnHCFe, inevitably leading to full-cell voltages of 2 V or less. Dehydration temperatures and densification and operating pressures optimised here should be used to ensure high ionic conductivity, low electronic conductivity, and a wide electrochemical stability

window.

Chapter 7

Conclusions and future work

7.1 Conclusions 151
7.2 Suggested future work 153

7.1 Conclusions

Sodium- and potassium-ion batteries are promising complementary technologies to lithium-ion batteries. Utilising earth abundant elements, they provide a possible low-cost alternative with potential performance improvements in rate capability and cyclability. Prussian blue analogues (PBAs) have already been demonstrated as the best performing sodium and potassium-ion cathode materials in both aqueous and nonaqueous electrolytes. This thesis focuses on developing PBAs that can be employed as anode and solid electrolyte materials. This was completed by careful consideration of composition-performance relationships to design, synthesise and characterise candidate PBA materials. During this process new synthesis methodology, synthesis theory, and characterisation techniques were developed. Below is a short summary of key results and conclusions.

In Chapter 3, manganese hexacyanochromate was investigated as a model transition metal hexacyanochromate compound. Large cubic particles were synthesised and characterised. The two types of water in the structure, coordinated and zeolitic, were studied using a combination of XRD, TGA, and FTIR. In a high-voltage 'water-in-salt' electrolyte manganese hexacyanochromate exhibited a reversible redox couple at the low potential of $-0.86\,\mathrm{V}$ vs. SHE. Ex situ analysis confirmed the charge storage mechanism was reversible sodium insertion and chromium redox. Manganese

hexacyanochromate exhibited very small volume change on cycling and high sodium-ion diffusion coefficient.

In Chapter 4, a synthesis procedure of zero-vacancy chromium(III) hexacyanochromate(III) was developed. This composition was targeted as it is a possible high specific capacity PBA anode material and, also, a high magnetic ordering temperature antiferromagnetic material. The procedure consists of first synthesising zero-vacancy rubidium chromium(II) hexacyanochromate(II) in anhydrous NMF from $CrCl_2$, NaCN, and RbCl, which is then oxidised in water. The synthesis was successful as the inability of NMF molecules to bond to P site chromium in hexacyanochromate vacancies inhibits the formation of material containing vacancies. Rubidium is large enough to be stable in the open-framework structure without partial solvation, but small enough to migrate easily through the structure. Evidence that chromium(III) hexacyanochromate(III) was vacancy-free came from XRD patterns, of both chromium(III) hexacyanochromate(III) and intermediate rubidium chromium(II) hexacyanochromate(II), its magnetic properties, and its electrochemical behaviour.

In Chapter 5, a holistic model for determining the charge neutrality mechanism in PBA synthesis was proposed. Although rudimentary, it was the first attempt of its kind and proved successful in rationalising what is observed experimentally. From basic thermodynamic and kinetics principles is proposed that formation of vacancy-rich and vacancy-poor material are in competition, vacancy-rich syntheses inherently have faster kinetics, and formation of vacancy-poor material relies on a greater thermodynamic driving force. The success of empirically derived synthesis strategies to reduce the vacancy content, such as including larger alkali ions or a chelating agents, can be explained and lays the foundation for the rational design of new synthesis strategies.

In Chapter 6, sodium zinc hexacyanoferrate(II) was investigated as a solid electrolyte material. Densification and operating pressure were optimised for ionic con-

ductivity. It was found that partial dehydration resulted in an increase in ionic conductivity, lower electronic conductivity, and a wider electrochemical stability window. Further dehydration induced a phase change in the material. The optimised material had room temperature ionic conductivity of $\approx 10^{-4}\,\mathrm{S\,cm^{-1}}$, an activation energy of 0.321 eV, and a electrochemical stability window of around 2.2 V.

7.2 Suggested future work

Arising from work contained in this thesis are several promising research areas:

- Development of a high specific capacity PBA anode material is closer than ever. Chromium hexacyanochromate shows promise and efforts should be directed towards increasing the particle size and optimising electrode preparation. Additionally, investigating a wider range of electrolytes is needed as electrolyte formulation can have a significant effect on electrochemical behaviour due to PBA solubility and other surface reactions. Finally, other PBA compositions should be studied following the same rationale that led to the targeting of chromium hexacyanochromate.

- Investigation of the magnetic properties of PBAs could be revived due to the synthesis of zero-vacancy chromium(III) hexacyanochromate(III). Work in this area ceased around year 2000 due to the inability to prepare other PBA compositions with room temperature magnetisation following the development of vanadium hexacyanochromate. Chromium hexacyanochromate, clearly a targeted composition, was not comprehensively examined due to inadequate synthesis methods, even though it was predicted to have room temperature magnetisation and stability in air. Future work in this area should confidently measure the magnetic ordering temperature of zero-vacancy chromium(III) hexacyanochromate(III), modify the synthesis to increase the particle size, and

devise strategies to introduce nonstoichiometry into the material to induce ferrimagnetic behaviour.

- Test sodium zinc hexacyanoferrate as a solid electrolyte in a full cell. Select PBA anode and cathode materials that have suitable reduction potentials and construct a full all-PBA cell. Controlling water in the cell will be crucial and drying procedures for all components will have to be optimised. A proof of concept cell can be prepared simply by first densifying the solid electrolyte material, withdrawing the plungers, and then adding electrode composite mixtures and pressing again. Additionally, other PBA compositions should be studied. It is possible to fully dehydrate a PBA with the conventional open-framework structure which would remove issues associated with decomposition of water. Efforts should be focussed on finding conventional PBA compositions with low electronic conductivities and wide electrochemical stability windows.

- Re-examine synthesis strategies with the new lens provided by the PBA synthesis model. First, conclusions from the model should be tested to experimentally determine its validity and efficacy. Then, new synthesis methods should be developed based on the model. These may include finding other chelating agents, with higher or lower binding energies, or using NMF and DMF as solvents for vacancy-free synthesis of a number of PBA compositions.

References

[1] A. Kraft, "On the Discovery and History of Prussian Blue," *Bull. Hist. Chem.*, vol. 32, no. 2, pp. 61–67, 2008.

[2] C. Gervais, M.-A. Languille, S. Réguer, M. Gillet, S. Pelletier, C. Garnier, E. P. Vicenzi, and L. Bertrand, "Why does Prussian blue fade? Understanding the role(s) of the substrate," *Journal of Analytical Atomic Spectrometry*, vol. 28, no. 10, pp. 1533–1668, 2013.

[3] E. W. FitzHugh, *Artists' Pigments: A Handbook of Their History and Characteristics, volume 3*. Washington: National Gallery of Art, 1997.

[4] J. Brown, "Observations and Experiments upon the Foregoing Preparation," *Philosophical Transactions*, vol. 33, no. 1, pp. 17–24, 1724.

[5] J. F. Keggin and F. D. Miles, "Structures and formulæ of the prussian blues and related compounds," *Nature*, vol. 137, pp. 577–578, 1936.

[6] H. J. Buser, A. Ludi, D. Schwarzenbach, and W. Petter, "The Crystal Structure of Prussian Blue: Fe4[Fe(CN)6]3·xH2O," *Inorganic Chemistry*, vol. 16, no. 11, pp. 2704–2710, 1977.

[7] G. W. Beall, W. O. Milligan, J. Korp, and I. Bernal, "Crystal structure of Mn3[Co(CN)6]2·12H2O and Cd3[Co(CN)6]2·12H2O by Neutron and X-Ray Diffraction," *Inorganic Chemistry*, vol. 16, no. 11, pp. 2715–2718, 1977.

[8] F. Herren, A. Ludi, P. Fischer, and W. Halg, "Neutron Diffraction Study of Prussian Blue, Fe4[Fe(CN)6]3.xH2O. Location of Water Molecules and Long-Range Magnetic Order," *Inorganic Chemistry*, vol. 19, no. 4, pp. 956–959, 1980.

[9] D. F. Shriver and D. B. Brown, "The environment of interstitial ions in a prussian blue analog, Co3[Co(CN)6]2," *Inorganic Chemistry*, vol. 8, no. 1, pp. 42–46, 1969.

[10] D. B. Brown and D. F. Shriver, "Structures and solid-state reactions of prussian blue analogs containing chromium, manganese, iron, and cobalt," *Inorganic Chemistry*, vol. 8, no. 1, pp. 37–42, 1969.

[11] M. J. Piernas Muñoz and E. Castillo Martínez, *Prussian Blue Based Batteries*. Springer, 2018.

[12] P. Day, *Molecules into materials: case studies in materials chemistry, mixed valency, magnetism and superconductivity*. Singapore: World Scientific, 2007.

[13] K. Hurlbutt, S. Wheeler, I. Capone, and M. Pasta, "Prussian Blue Analogs as Battery Materials," *Joule*, vol. 2, no. 10, pp. 1950–1960, 2018.

[14] N. Imanishi, T. Morikawa, J. Kondo, Y. Takeda, O. Yamamoto, N. Kinugasa, and T. Yamagishi, "Lithium intercalation behavior into iron cyanide complex as positive electrode of lithium secondary battery," *Journal of Power Sources*, vol. 79, no. 2, pp. 215–219, 1999.

[15] Y. Lu, L. Wang, J. Cheng, and J. B. Goodenough, "Prussian blue: a new framework of electrode materials for sodium batteries," *Chemical Communications*, vol. 48, no. 52, p. 6544, 2012.

[16] X. Bie, K. Kubota, T. Hosaka, K. Chihara, and S. Komaba, "A novel K-ion battery: hexacyanoferrate(II)/graphite cell," *J. Mater. Chem. A*, vol. 5, no. 9, pp. 4325–4330, 2017.

[17] H.-W. Lee, M. Pasta, R. Y. Wang, R. Ruffo, and Y. Cui, "Effect of the al-

kali insertion ion on the electrochemical properties of nickel hexacyanoferrate electrodes," *Faraday Discuss.*, vol. 176, pp. 69–81, 2014.

[18] R. Chen, H. Tanaka, T. Kawamoto, M. Asai, C. Fukushima, H. Na, M. Kurihara, M. Watanabe, M. Arisaka, and T. Nankawa, "Selective removal of cesium ions from wastewater using copper hexacyanoferrate nanofilms in an electrochemical system," *Electrochimica Acta*, vol. 87, pp. 119–125, 2013.

[19] R. Y. Wang, C. D. Wessells, R. A. Huggins, and Y. Cui, "Highly reversible open framework nanoscale electrodes for divalent ion batteries," *Nano Letters*, vol. 13, no. 11, pp. 5748–5752, 2013.

[20] X. Wu, Y. Qi, J. J. Hong, Z. Li, A. S. Hernandez, and X. Ji, "Rocking-Chair Ammonium-Ion Battery: A Highly Reversible Aqueous Energy Storage System," *Angewandte Chemie - International Edition*, vol. 56, no. 42, pp. 13026–13030, 2017.

[21] X. Wu, Y. Xu, H. Jiang, Z. Wei, J. J. Hong, A. S. Hernandez, F. Du, and X. Ji, "NH4+ Topotactic Insertion in Berlin Green: An Exceptionally Long-Cycling Cathode in Aqueous Ammonium-Ion Batteries," *ACS Applied Energy Materials*, vol. 1, no. 7, pp. 3077–3083, 2018.

[22] A. G. Sharpe, *The Chemistry of Cyano Complexes of the Transition Metals*. Academic Press Inc., 1976.

[23] K. R. Dunbar and R. A. Heintz, *Chemistry of Transition Metal Cyanide Compounds: Modern Perspectives*, vol. 45. John Wiley & Sons, Inc., 1996.

[24] W. P. Griffith, "Cyanide complexes of the transition metals," *Quarterly Reviews, Chemical Society*, vol. 16, no. 2, pp. 188–207, 1962.

[25] M. Shatruk, C. Avendano, and K. R. Dunbar, "Cyanide-Bridged Complexes of Transition Metals: A Molecular Magnetism Perspective," in *Progress in Inorganic Chemistry* (K. D. Karlin, ed.), Progress in Inorganic Chemistry, pp. 155–334, John Wiley & Sons, Inc., 2009.

[26] "Bonding in Coordinate Compounds," *https://chem.libretexts.org/@go/page/47294 [accessed 10/06/2021].*

[27] M. A. Arrio, P. Sainctavit, C. Cartier Dit Moulin, T. Mallah, M. Verdaguer, E. Pellegrin, and C. T. Chen, "Characterization of chemical bonds in bimetallic cyanides using X-ray absorption spectroscopy at L2,3 edges," *Journal of the American Chemical Society*, vol. 118, no. 27, pp. 6422–6427, 1996.

[28] F. Scholz and A. Dostal, "The Formal Potentials of Solid Metal Hexacyanometalates," *Angewandte Chemie International Edition in English*, vol. 34, no. 23-24, pp. 2685–2687, 1995.

[29] J. Jørgensen, C.K., Shriver, D.F., Neilands, J.B., Buchanan, B.B., Feeney, R.E., Komatsu, S.K., Ahrland, S., Hudson, R.F., Williams, R.J.P., Hale, "Structure and bonding," 1967.

[30] Y. Moritomo, T. Matsuda, Y. Kurihara, and J. Kim, "Cubic-Rhombohedral Structural Phase Transition," *Journal of the Physical Society of Japan*, vol. 80, p. 074608, 2011.

[31] L. Wang, Y. Lu, J. Liu, M. Xu, J. Cheng, D. Zhang, and J. B. Goodenough, "A superior low-cost cathode for a Na-Ion battery," *Angewandte Chemie - International Edition*, vol. 52, no. 7, pp. 1964–1967, 2013.

[32] T. Matsuda, Y. Kurihara, and Y. Moritomo, "Lithium intercalation properties in manganese-iron Prussian blue analogues," *Journal of Physics: Conference Series*, vol. 428, p. 12019, 2013.

[33] H. L. Boström, I. E. Collings, A. B. Cairns, C. P. Romao, and A. L. Goodwin, "High-pressure behaviour of Prussian blue analogues: Interplay of hydration, Jahn-Teller distortions and vacancies," *Dalton Transactions*, vol. 48, no. 5, pp. 1647–1655, 2019.

[34] A. Eftekhari, Z. Jian, and X. Ji, "Potassium Secondary Batteries," *ACS Applied Materials and Interfaces*, vol. 9, no. 5, pp. 4404–4419, 2017.

[35] T. Sangvanich, V. Sukwarotwat, R. J. Wiacek, R. M. Grudzien, G. E. Fryxell, R. S. Addleman, C. Timchalk, and W. Yantasee, "Selective capture of cesium and thallium from natural waters and simulated wastes with copper ferrocyanide functionalized mesoporous silica," *Journal of Hazardous Materials*, vol. 182, no. 1-3, pp. 225–231, 2010.

[36] A. L. Goodwin and C. J. Kepert, "Negative thermal expansion and low-frequency modes in cyanide-bridged framework materials," *Physical Review B - Condensed Matter and Materials Physics*, vol. 71, no. 14, p. 140301(R), 2005.

[37] A. L. Goodwin, M. Calleja, M. J. Conterio, M. T. Dove, J. S. O. Evans, D. A. Keen, L. Peters, and M. G. Tucker, "Colossal Positive and Negative Thermal Expansion in the Framework Material Ag3[Co(CN)6]," *Science*, vol. 319, no. 5864, pp. 794–797, 2008.

[38] A. Fujishima, O. Sato, T. Lyoda, and K. Hashimoto, "Electrochemically Tunable Magnetic Phase Transition in a High-Ta Chromium Cyanide Thin Film," *Science*, vol. 271, no. 5245, pp. 49–51, 1996.

[39] S. I. Ohkoshi, K. I. Arai, Y. Sato, and K. Hashimoto, "Humidity-induced magnetization and magnetic pole inversion in a cyano-bridged metal assembly," *Nature Materials*, vol. 3, no. 12, pp. 857–861, 2004.

[40] O. Sato, T. Iyoda, A. Fujishima, and K. Hashimoto, "Photoinduced magnetization of a cobalt-iron cyanide," *Science*, vol. 272, no. 5262, pp. 704–705, 1996.

[41] L. J. Murray, M. Dinc, and J. R. Long, "Hydrogen storage in metal-organic frameworks," *Chemical Society Reviews*, vol. 38, no. 5, pp. 1294–1314, 2009.

[42] V. D. Neff, "Electrochemical Oxidation and Reduction of Thin Films of Prussian Blue," *Journal of The Electrochemical Society*, vol. 125, no. 6, p. 886, 1978.

[43] D. Ellis, M. Eckhoff, and V. D. Neff, "Electrochromism in the mixed-valence hexacyanides. 1. Voltammetric and spectral studies of the oxidation and reduction of thin films of Prussian blue," *Journal of Physical Chemistry*, vol. 85, no. 9, pp. 1225–1231, 1981.

[44] K. P. Rajan and V. D. Neff, "Electrochromism in the mixed-valence hexacyanides. 2. Kinetics of the reduction of ruthenium purple and Prussian blue," *Journal of Physical Chemistry*, vol. 86, no. 22, pp. 4361–4368, 1982.

[45] K. Itaya, K. Shibayama, H. Akahoshi, and S. Toshima, "Prussian-blue-modified electrodes: An application for a stable electrochromic display device," *Journal of Applied Physics*, vol. 53, no. 1, pp. 804–805, 1982.

[46] K. Itaya, I. Uchida, and V. D. Neff, "Electrochemistry of Polynuclear Transition Metal Cyanides: Prussian Blue and Its Analogues," *Accounts of Chemical Research*, vol. 19, no. 6, pp. 162–168, 1986.

[47] D. E. Stilwell, K. H. Park, and M. H. Miles, "Electrochemical studies of the factors influencing the cycle stability of Prussian Blue films," *Journal of Applied Electrochemistry*, vol. 22, no. 4, pp. 325–331, 1992.

[48] V. Y. Kotov, R. R. Nazmutdinov, G. N. Botukhova, G. A. Tsirlina, and O. A. Petrii, "Hard-to-detect CoIII/CoII reduction in a hexacyanocobaltate," *Mendeleev Communications*, vol. 14, no. 3, pp. 113–115, 2004.

[49] C. D. Wessells, S. V. Peddada, M. T. McDowell, R. a. Huggins, and Y. Cui, "The effect of insertion species on nanostructured open framework hexacyanoferrate battery electrodes," *Journal of The Electrochemical Society*, vol. 159, no. 2, pp. A98–A103, 2012.

[50] R. Y. Wang, B. Shyam, K. H. Stone, J. N. Weker, M. Pasta, H. W. Lee, M. F. Toney, and Y. Cui, "Reversible Multivalent (Monovalent, Divalent, Trivalent) Ion Insertion in Open Framework Materials," *Advanced Energy Materials*, vol. 5, no. 12, p. 1401869, 2015.

[51] R. A. Huggins, *Advanced Batteries: Materials Science Aspects*. New York: Springer, 2009.

[52] J. B. Goodenough and K. S. Park, "The Li-ion rechargeable battery: A perspective," *Journal of the American Chemical Society*, vol. 135, no. 4, pp. 1167–1176, 2013.

[53] P. A. Nelson, S. Ahmed, K. G. Gallagher, and D. W. Dees, "Modeling the Performance and Cost of Lithium-Ion Batteries for Electric-Drive Vehicles, Third Edition," Tech. Rep. ANL/CSE-19/2, Argonne National Laboratory (ANL), Argonne, IL (United States), 2019.

[54] B. Dunn, H. Kamath, and J.-M. Tarascon, "Electrical Energy storage for the Grid : A Battery of Choices," *Science*, vol. 334, no. 6058, pp. 928–935, 2011.

[55] Z. Yang, J. Zhang, M. C. W. Kintner-Meyer, X. Lu, D. Choi, J. P. Lemmon, and J. Liu, "Electrochemical energy storage for green grid," *Chemical Reviews*, vol. 111, no. 5, pp. 3577–3613, 2011.

[56] C. Vaalma, D. Buchholz, M. Weil, and S. Passerini, "A cost and resource analysis of sodium-ion batteries," *Nature Reviews Materials*, vol. 3, p. 18013, 2018.

[57] S. Dhir, S. Wheeler, I. Capone, and M. Pasta, "Outlook on K-ion Batteries," *Chem*, vol. 6, no. 10, pp. 2442–2460, 2020.

[58] N. Yabuuchi, K. Kubota, M. Dahbi, and S. Komaba, "Research development on sodium-ion batteries," *Chemical Reviews*, vol. 114, no. 23, pp. 11636–11682, 2014.

[59] N. Yabuuchi, K. Kubota, M. Dahbi, and S. Komaba, "Research development on potassium-ion batteries," *Chemical Reviews*, vol. 120, no. 14, pp. 6358–6466, 2020.

[60] A. Eftekhari, "Potassium secondary cell based on Prussian blue cathode," *Journal of Power Sources*, vol. 126, pp. 221–228, 2004.

[61] C. D. Wessells, R. a. Huggins, and Y. Cui, "Copper hexacyanoferrate battery electrodes with long cycle life and high power," *Nature Communications*, vol. 2, p. 550, 2011.

[62] C. D. Wessells, S. V. Peddada, R. A. Huggins, and Y. Cui, "Nickel Hexacyanoferrate Nanoparticle Electrodes For Aqueous Sodium and Potassium Ion Batteries," *Nano Letters*, vol. 11, pp. 5421–5425, 2011.

[63] K. Igarashi, F. Nakada, and Y. Moritomo, "Electronic structure of hole-doped Co-Fe cyanides: Na1.60-δCo[Fe(CN)6].90.2.9H2O(0.0<δ<0.85)," *Physical Review B - Condensed Matter and Materials Physics*, vol. 78, no. 23, p. 235106, 2008.

[64] F. Nakada, H. Kamioka, Y. Moritomo, J. E. Kim, and M. Takata, "Electronic phase diagram of valence-controlled cyanide: Na0.84-δCo[Fe(CN)6]0.71.3.8H2O," *Physical Review B*, vol. 77, no. 22, p. 224436, 2008.

[65] T. Shibata, F. Nakada, H. Kamioka, and Y. Moritomo, "Magnetic and electronic properties of valence-controlled Ni-Fe cyanide," *Journal of the Physical Society of Japan*, vol. 77, no. 10, 2008.

[66] Y. Moritomo, K. Igarashi, T. Matsuda, and J. Kim, "Doping-Induced Structural Phase Transition in Na1.6-xCo[Fe(CN)6]0.90.2.9H2O," *Journal of the Physical Society of Japan*, vol. 78, no. 7, p. 074602, 2009.

[67] Y. Moritomo, Y. Kurihara, T. Matsuda, and J. Kim, "Structural phase diagram of Mn-Fe cyanide against cation concentration," *Journal of the Physical Society of Japan*, vol. 80, p. 103601, 2011.

[68] T. Matsuda and Y. Moritomo, "Thin film electrode of Prussian blue analogue for Li-ion battery," *Applied Physics Express*, vol. 4, no. 4, p. 190, 2011.

[69] M. Takachi, T. Matsuda, and Y. Moritomo, "Cobalt hexacyanoferrate as cathode material for Na+ secondary battery," *Applied Physics Express*, vol. 6, no. 2, p. 025802, 2013.

[70] T. Matsuda, M. Takachi, and Y. Moritomo, "A sodium manganese ferrocyanide thin film for Na-ion batteries," *Chemical Communications*, vol. 49, no. 27, pp. 2750–2752, 2013.

[71] M. Pasta, C. D. Wessells, R. A. Huggins, and Y. Cui, "A high-rate and long cycle life aqueous electrolyte battery for grid-scale energy storage," *Nature Communications*, vol. 3, p. 1149, 2012.

[72] M. Pasta, C. D. Wessells, N. Liu, J. Nelson, M. T. McDowell, R. A. Huggins, M. F. Toney, and Y. Cui, "Full open-framework batteries for stationary energy storage," *Nature Communications*, vol. 5, p. 3007, 2014.

[73] A. Firouzi, R. Qiao, S. Motallebi, C. W. Valencia, H. S. Israel, M. Fujimoto, L. A. Wray, Y. D. Chuang, W. Yang, and C. D. Wessells, "Monovalent manganese based anodes and co-solvent electrolyte for stable low-cost high-rate sodium-ion batteries," *Nature Communications*, vol. 9, p. 861, 2018.

[74] J. Wang, C. Mi, P. Nie, S. Dong, S. Tang, and X. Zhang, "Sodium-rich iron hexacyanoferrate with nickel doping as a high performance cathode for aqueous sodium ion batteries," *Journal of Electroanalytical Chemistry*, vol. 818, pp. 10–18, 2018.

[75] L. Jiang, Y. Lu, C. Zhao, L. Liu, J. Zhang, Q. Zhang, X. Shen, J. Zhao, X. Yu, H. Li, X. Huang, L. Chen, and Y.-S. Hu, "Building aqueous K-ion batteries for energy storage," *Nature Energy*, vol. 4, pp. 495–503, 2019.

[76] W. Li, C. Han, W. Wang, Q. Xia, S. Chou, Q. Gu, B. Johannessen, H. K. Liu, and S. Dou, "Stress Distortion Restraint to Boost the Sodium Ion Storage Performance of a Novel Binary Hexacyanoferrate," *Advanced Energy Materials*, vol. 10, no. 4, p. 1903006, 2020.

[77] R. Chen, Y. Huang, M. Xie, Z. Wang, Y. Ye, L. Li, and F. Wu, "A chemical inhibition method to synthetize highly crystalline Prussian blue analogs for sodium-ion battery cathodes," *ACS Applied Materials & Interfaces*, vol. 8, no. 46, pp. 31669–31676, 2016.

[78] L. Suo, O. Borodin, T. Gao, M. Olguin, J. Ho, X. Fan, C. Luo, C. Wang, and K. Xu, ""Water-in-salt"; electrolyte enables high-voltage aqueous lithium-ion chemistries," *Science*, vol. 350, no. 6263, pp. 938–943, 2015.

[79] Y. Yamada, K. Usui, K. Sodeyama, S. Ko, Y. Tateyama, and A. Yamada, "Hydrate-melt electrolytes for high-energy-density aqueous batteries," *Nature Energy*, vol. 1, no. 10, p. 16129, 2016.

[80] R.-S. Kühnel, D. Reber, and C. Battaglia, "A High-Voltage Aqueous Electrolyte for Sodium-Ion Batteries," *ACS Energy Letters*, vol. 2, no. 9, pp. 2005–2006, 2017.

[81] R.-S. Kühnel, D. Reber, and C. Battaglia, "Electrochemical Stability of Water-in-Salt Electrolytes," *Journal of The Electrochemical Society*, vol. 167, no. 7, p. 070544, 2020.

[82] Y. You, X.-L. Wu, Y.-X. Yin, and Y.-G. Guo, "High-quality Prussian blue crystals as superior cathode materials for room-temperature sodium-ion batteries," *Energy & Environmental Science*, vol. 7, no. 5, pp. 1643–1647, 2014.

[83] Y. Moritomo, K. Wakaume, M. Takachi, X. Zhu, and H. Kamioka, "Li+ intercalation of manganese ferrocyanide as investigated by in situ valence-differential absorption spectroscopy," *Journal of the Physical Society of Japan*, vol. 82, p. 094710, 2013.

[84] X. Bie, K. Kubota, T. Hosaka, K. Chihara, and S. Komaba, "Synthesis and electrochemical properties of Na-rich Prussian blue analogues containing Mn, Fe, Co, and Fe for Na-ion batteries," *Journal of Power Sources*, vol. 378, pp. 322–330, 2018.

[85] M. Pasta, R. Y. Wang, R. Ruffo, R. Qiao, H.-W. Lee, B. Shyam, M. Guo, Y. Wang, L. A. Wray, W. Yang, M. F. Toney, and Y. Cui, "Manganese-cobalt hexacyanoferrate cathodes for sodium-ion batteries," *Journal of Materials Chemistry A*, vol. 4, no. 11, pp. 4211–4223, 2016.

[86] L. Wang, J. Song, R. Qiao, L. A. Wray, M. A. Hossain, Y. D. Chuang, W. Yang, Y. Lu, D. Evans, J. J. Lee, S. Vail, X. Zhao, M. Nishijima, S. Kakimoto, and J. B. Goodenough, "Rhombohedral Prussian white as cathode for rechargeable

sodium-ion batteries," *Journal of the American Chemical Society*, vol. 137, no. 7, pp. 2548–2554, 2015.

[87] X. Wu, C. Wu, C. Wei, L. Hu, J. Qian, Y. Cao, X. Ai, J. Wang, and H. Yang, "Highly Crystallized Na2CoFe(CN)6 with Suppressed Lattice Defects as Superior Cathode Material for Sodium-Ion Batteries," *ACS Applied Materials and Interfaces*, vol. 8, no. 8, pp. 5393–5399, 2016.

[88] Y. Moritomo, S. Urase, and T. Shibata, "Enhanced battery performance in manganese hexacyanoferrate by partial substitution," *Electrochimica Acta*, vol. 210, pp. 963–969, 2016.

[89] J. Song, L. Wang, Y. Lu, J. Liu, B. Guo, P. Xiao, J. J. Lee, X. Q. Yang, G. Henkelman, and J. B. Goodenough, "Removal of interstitial H2O in hexacyanometallates for a superior cathode of a sodium-ion battery," *Journal of the American Chemical Society*, vol. 137, no. 7, pp. 2658–2664, 2015.

[90] H. Gao, S. Xin, L. Xue, and J. B. Goodenough, "Stabilizing a High-Energy-Density Rechargeable Sodium Battery with a Solid Electrolyte," *Chem*, vol. 4, no. 4, pp. 833–844, 2018.

[91] O. Kahn, *Molecular Magnetism*. New York: Wiley-VCH Verlag, 1993.

[92] J. M. Manriquez, G. T. Yee, R. S. Mclean, A. J. Epstein, and J. S. Miller, "A Room-Temperature Molecular/Organic-Based Magnet," *Science*, vol. 252, no. 5011, pp. 1415–1417, 1991.

[93] V. Gadet, T. Mallah, I. Castro, M. Verdaguer, and P. Veillet, "High-Tc Molecular-Based Magnets: A Ferromagnetic Bimetallic Chromium(III)-Nickel(II) Cyanide with Tc = 90 K," *Journal of the American Chemical Society*, vol. 114, no. 23, pp. 9213–9214, 1992.

[94] T. Mallah, S. Thiébaut, M. Verdaguer, and P. Veillet, "High-Tc molecular-based magnets: ferrimagnetic mixed-valence chromium(III)-chromium(II) cyanides with Tc at 240 and 190 Kelvin," *Science*, vol. 262, no. 5139, pp. 1554–1557, 1993.

[95] S. Ferlay, T. Mallah, R. Ouahès, P. Veillet, and M. Verdaguer, "A room-temperature organometallic magnet based on prussian blue," *Nature*, vol. 378, no. 6558, pp. 701–703, 1995.

[96] S. Ferlay, T. Mallah, R. Ouahès, P. Veillet, and M. Verdaguer, "A Chromium-vanadyl ferrimagnetic molecule-based magnet: structure, magnetism, and orbital interpretation," *Inorganic Chemistry*, vol. 38, no. 2, pp. 229–234, 1999.

[97] A. Bleuzen, C. Lomenech, V. Escax, F. Villain, F. Varret, C. Cartier Dit Moulin, and M. Verdaguer, "Photoinduced ferrimagnetic systems in Prussian blue analogues C(i)(x)Co4[Fe(CN)6](y) (C(i) = alkali cation). 1. Conditions to observe the phenomenon," *Journal of the American Chemical Society*, vol. 122, no. 28, pp. 6648–6652, 2000.

[98] W. R. Entley and G. S. Girolami, "New Three-Dimensional Ferrimagnetic Materials: K2Mn[Mn(CN)6], Mn3[Mn(CN)6]2·12H2O, and CsMn[Mn(CN)6]·1/2H2O," *Inorganic Chemistry*, vol. 33, no. 23, pp. 5165–5166, 1994.

[99] W. R. Entley and G. S. Girolami, "High-temperature molecular magnets based on cyanovanadate building blocks: Spontaneous magnetization at 230 K," *Science*, vol. 268, no. 5209, pp. 397–400, 1995.

[100] S. M. Holmes and G. S. Girolami, "Sol-gel synthesis of KV(II)[Cr(III)(CN)6]·2H2O: A crystalline molecule-based magnet with a magnetic ordering temperature above 100oC," *Journal of the American Chemical Society*, vol. 121, no. 23, pp. 5593–5594, 1999.

[101] K. Hashimoto, "Electrochemical Synthesis of High-Tc, Colored, Magnetic Thin Films Composed of Vanadium (II/III)-Chromium(II) Hexacyanochromate(III)," *Advanced Materials*, vol. 8904, no. 24, pp. 1955–1958, 2000.

[102] W. R. Entley, C. R. Treadway, and G. S. Girolami, "Molecular magnets constructed from cyanometalate building blocks," *Molecular Crystals and Liquid Crystals Science and Technology Section A: Molecular Crystals and Liquid Crystals*, vol. 273, no. 1, pp. 153–166, 1995.

[103] M. Verdaguer, A. Bleuzen, V. Marvaud, J. Vaissermann, M. Seuleiman, C. Desplanches, A. Scuiller, C. Train, R. Garde, G. Gelly, C. Lomenech, I. Rosenman, P. Veillet, C. Cartier, and F. Villain, "Molecules to build solids: High Tc molecule-based magnets by design and recent revival of cyano complexes chemistry," *Coordination Chemistry Reviews*, vol. 190-192, pp. 1023–1047, 1999.

[104] S. I. Ohkoshi, H. Tokoro, and K. Hashimoto, "Temperature- and photo-induced phase transition in rubidium manganese hexacyanoferrate," *Coordination Chemistry Reviews*, vol. 249, no. 17-18, pp. 1830–1840, 2005.

[105] M. Verdaguer and A. N. Gleizes, "Magnetism: Molecules to Build Solids," *European Journal of Inorganic Chemistry*, pp. 723–731, 2020.

[106] M. Verdaguer and G. S. Girolami, "Magnetic Prussian Blue Analogs," in *Magnetism: Molecules to Materials V* (J. S. Miller and M. Drillon, eds.), Wiley Online Books, ch. 9, pp. 283–346, Wiley-VCH Verlag, 2004.

[107] H. Tokoro and S. I. Ohkoshi, "Novel magnetic functionalities of Prussian blue analogs," *Dalton Transactions*, vol. 40, no. 26, pp. 6825–6833, 2011.

[108] J. J. L. Morton, *Magnetic properties of materials [Lecture notes]*. UCL, 2012.

[109] M. L. Néel, "Propriétés magnétiques des ferrites ; ferrimagnétisme et antiferromagnétisme," *Ann. Phys.*, vol. 12, no. 3, pp. 137–198, 1948.

[110] M. Atanasov, P. Comba, and C. A. Daul, "DFT studies on the magnetic exchange across the cyanide bridge," *Journal of Physical Chemistry A*, vol. 110, no. 49, pp. 13332–13340, 2006.

[111] Ø. Hatlevik, W. E. Buschmann, J. Zhang, J. L. Manson, and J. S. Miller, "Enhancement of the magnetic ordering temperature and air stability of a mixed valent vanadium hexacyanochromate(III) magnet to 99oC (372 K)," *Advanced Materials*, vol. 11, no. 11, pp. 914–918, 1999.

[112] E. Ruiz, A. Rodríguez-Fortea, S. Alvarez, and M. Verdaguer, "Is it possible to get high Tc magnets with Prussian blue analogues? A theoretical prospect," *Chemistry - A European Journal*, vol. 11, no. 7, pp. 2135–2144, 2005.

[113] M. Nishino, Y. Yoshioka, and K. Yamaguchi, "Effective exchange interactions and magnetic phase transition temperatures in Prussian blue analogs: a study by density functional theory," *Chemical Physics Letters*, vol. 297, no. 1-2, pp. 51–59, 1998.

[114] N. T. Thanh, N. Maclean, and S. Mahiddine, "Mechanisms of nucleation and growth of nanoparticles in solution," *Chemical Reviews*, vol. 114, no. 15, pp. 7610–7630, 2014.

[115] A. Dostal, U. Schröder, and F. Scholz, "Electrochemistry of chromium(II) hexacyanochromate(III) and electrochemically induced isomerization of solid iron(II) hexacyanochromate(III) mechanically immobilized on the surface of a graphite electrode," *Inorganic Chemistry*, vol. 34, no. 7, pp. 1711–1717, 1995.

[116] M. Cao, X. Wu, X. He, and C. Hu, "Shape-controlled synthesis of Prussian

blue analogue Co3[Co(CN) 6]2 nanocrystals," *Chemical Communications*, vol. 2, no. 17, pp. 2241–2243, 2005.

[117] H. L. Sun, H. Shi, F. Zhao, L. Qi, and S. Gao, "Shape-dependent magnetic properties of low-dimensional nanoscale Prussian blue (PB) analogue SmFe(CN)6·4H2O," *Chemical Communications*, no. 34, pp. 4339–4341, 2005.

[118] M. Yamada, T. Sato, M. Miyake, and Y. Kobayashi, "Temporal evolution of composition and crystal structure of cobalt hexacyanoferrate nano-polymers synthesized in reversed micelles," *Journal of Colloid and Interface Science*, vol. 315, no. 1, pp. 369–375, 2007.

[119] M. Arai, M. Miyake, and M. Yamada, "Metal(II) hexacyanochromate(III) MCr (M = Co, Cu, Fe) coordination nanoparticles stabilized by alkyl surface coordination ligand: Downsizing effect on their crystal structure and magnetic properties," *Journal of Physical Chemistry C*, vol. 112, no. 6, pp. 1953–1962, 2008.

[120] C. Suryanarayana and M. G. Norton, *X-Ray diffraction: A Practical Approach*. New York: Springer US, 1st ed., 1998.

[121] E. Zolotoyabko, *Basic concepts of X-ray diffraction*. Weinheim: Wiley-VCH, 2014.

[122] K. Momma and F. Izumi, "VESTA 3 for three-dimensional visualization of crystal, volumetric and morphology data," *Journal of Applied Crystallography*, vol. 44, no. 6, pp. 1272–1276, 2011.

[123] S. Wheeler, I. Capone, S. Day, C. Tang, and M. Pasta, "Low-Potential Prussian Blue Analogues for Sodium-Ion Batteries: Manganese Hexacyanochromate," *Chemistry of Materials*, vol. 31, no. 7, pp. 2619–2626, 2019.

[124] H. M. Rietveld, "A profile refinement method for nuclear and magnetic structures," *Journal of Applied Crystallography*, vol. 2, pp. 65–71, 1969.

[125] B. H. Toby, "R factors in Rietveld analysis: How good is good enough?," *Powder Diffraction*, vol. 21, no. 1, pp. 67–70, 2006.

[126] B. H. Toby, "EXPGUI a graphical user interface for GSAS," *J. Appl. Cryst*, vol. 34, pp. 210–213, 2001.

[127] A. C. Larson and R. B. Von Dreele, "General Structure Analysis System (GSAS)," tech. rep., 2004.

[128] B. H. Toby and R. B. Von Dreele, "GSAS-II: The genesis of a modern open-source all purpose crystallography software package," *Journal of Applied Crystallography*, vol. 46, no. 2, pp. 544–549, 2013.

[129] K. D. Parry V, "Scanning Electron Microscopy: An introduction," *III-Vs Review*, vol. 13, no. 4, pp. 40–44, 2000.

[130] M. Fiore, S. Wheeler, K. Hurlbutt, I. Capone, J. Fawdon, R. Ruffo, and M. Pasta, "Paving the way toward highly efficient, high-energy potassium-ion batteries with ionic-liquid electrolytes," *Chemistry of Materials*, vol. 32, no. 18, pp. 7653–7661, 2020.

[131] B. Smith, *Fundamentals of Fourier Transform Infrared Spectroscopy*. Boca Raton: CRC Press, 2nd ed., 2011.

[132] S. F. Kettle, E. Diana, E. M. Marchese, E. Boccaleri, and P. L. Stanghellini, "The vibrational spectra of the cyanide ligand revisited: The ν(CN) infrared and Raman spectroscopy of Prussian blue and its analogues," *Journal of Raman Spectroscopy*, vol. 42, no. 11, pp. 2006–2014, 2011.

[133] S. J. Gerber and E. Erasmus, "Electronic effects of metal hexacyanoferrates: An XPS and FTIR study," *Materials Chemistry and Physics*, vol. 203, pp. 73–81, 2018.

[134] D. O. Ojwang, J. Grins, D. Wardecki, M. Valvo, V. Renman, L. Häggström, T. Ericsson, T. Gustafsson, A. Mahmoud, R. P. Hermann, and G. Svensson, "Structure Characterization and Properties of K-Containing Copper Hexacyanoferrate," *Inorganic Chemistry*, vol. 55, no. 12, pp. 5924–5934, 2016.

[135] M. Avila, L. Reguera, J. Rodríguez-Hernández, J. Balmaseda, and E. Reguera, "Porous framework of T2[Fe(CN)6]·xH2O with T=Co, Ni, Cu, Zn, and H2 storage," *Journal of Solid State Chemistry*, vol. 181, no. 11, pp. 2899–2907, 2008.

[136] R. H. Scott, V. A. Fassel, R. N. Kniseley, and D. E. Nixon, "Inductively Coupled Plasma-Optical Emission Analytical Spectrometry: A Compact Facility for Trace Analysis of Solutions," *Analytical Chemistry*, vol. 46, no. 1, pp. 75–80, 1974.

[137] C. B. Boss and K. J. Fredeen, "Concepts, Instrumentation and techniques in Inductively Coupled Plasma Optical Emission Spectrometry," tech. rep., PerkinElmer, 2004.

[138] E. H. M. Sakho, E. Allahyari, O. S. Oluwafemi, S. Thomas, and N. Kalarikkal, "Dynamic Light Scattering (DLS)," in *Micro and Nano Technologies* (S. Thomas, R. Thomas, A. K. Zachariah, R. K. B. T. T. Mishra, and R. M. T. for Nanomaterials Characterization, eds.), ch. 2, pp. 37–49, Elsevier, 2017.

[139] A. J. Bard and L. R. Faulkner, *Electrochemical methods: fundamentals and applications*. New York: John Wiley & Sons, Inc., 2nd ed., 1980.

[140] J. Newman and K. E. Thomas-Alyea, *Electrochemical Systems*. Hoboken, New Jersey: John Wiley & Sons, Inc., 3rd ed., 2004.

[141] E. Barsoukov and J. R. Macdonald, eds., *Impedance Spectroscopy Theory, Experiment, and Applications*. John Wiley & Sons, Inc., 2nd ed., 2005.

[142] J. Clarke and A. Braginshi, *The SQUID Handbook: Fundamentals and Technology of SQUIDs and SQUID Systems*. Weinheim: WILEY-VCH Verlag, 2006.

[143] M. Pasta, R. Y. Wang, R. Ruffo, R. Qiao, H. W. Lee, B. Shyam, M. Guo, Y. Wang, L. A. Wray, W. Yang, M. F. Toney, and Y. Cui, "Manganese-cobalt hexacyanoferrate cathodes for sodium-ion batteries," *Journal of Materials Chemistry A*, vol. 4, no. 11, pp. 4211–4223, 2016.

[144] L. Deng, Z. Yang, L. Tan, L. Zeng, Y. Zhu, and L. Guo, "Investigation of the Prussian Blue Analog Co3[Co(CN)6]2 as an Anode Material for Nonaqueous Potassium-Ion Batteries," *Advanced Materials*, vol. 30, no. 31, p. 1802510, 2018.

[145] P. Nie, L. Shen, H. Luo, B. Ding, G. Xu, J. Wang, and X. Zhang, "Prussian blue analogues: a new class of anode materials for lithium ion batteries," *J. Mater. Chem. A*, vol. 2, no. 16, pp. 5852–5857, 2014.

[146] T. Shibata, M. Takachi, and Y. Moritomo, "Low Voltage Charge/Discharge Behavior of Manganese Hexacyanoferrate," *Batteries*, vol. 3, no. 1, 2017.

[147] J. Polte, "Fundamental growth principles of colloidal metal nanoparticles - a new perspective," *CrystEngComm*, vol. 17, no. 36, pp. 6809–6830, 2015.

[148] H. U. Güdel, H. Stucki, and A. Ludi, "The crystal structure of manganese(II) hexacyanochromate(III), Mn3[Cr(CN)6]2·xH2O," *Inorganica Chimica Acta*, vol. 7, pp. 121–124, 1973.

[149] W. Dong, L. N. Zhu, H. B. Song, D. Z. Liao, Z. H. Jiang, S. P. Yan, P. Cheng, and S. Gao, "A Prussian-Blue Type Ferrimagnet Na[MnCr(CN)6]: Single Crystal Structure and Magnetic Properties," *Inorganic Chemistry*, vol. 43, no. 8, pp. 2465–2467, 2004.

[150] A. Ferrari, M. E. Tani, and E. Morisi, "The crystal structure of hexacyanochromate(III) of divalent cations," *Acta Crystallographica*, vol. 15, no. 1, pp. 90–90, 1962.

[151] I. E. Åkerblom, D. O. Ojwang, J. Grins, and G. Svensson, "A thermogravimetric study of thermal dehydration of copper hexacyanoferrate by means of model-free kinetic analysis," *Journal of Thermal Analysis and Calorimetry*, vol. 129, no. 2, pp. 721–731, 2017.

[152] Y. Mizuno, M. Okubo, E. Hosono, T. Kudo, H. Zhou, and K. Oh-Ishi, "Suppressed activation energy for interfacial charge transfer of a Prussian blue analog thin film electrode with hydrated ions (Li+, Na+, and Mg2+)," *Journal of Physical Chemistry C*, vol. 117, no. 21, pp. 10877–10882, 2013.

[153] P. Xiao, J. Song, L. Wang, J. B. Goodenough, and G. Henkelman, "Theoretical study of the structural evolution of a Na2FeMn(CN)6 cathode upon Na intercalation," *Chemistry of Materials*, vol. 27, no. 10, pp. 3763–3768, 2015.

[154] L. Suo, O. Borodin, Y. Wang, X. Rong, W. Sun, X. Fan, S. Xu, M. A. Schroeder, A. V. Cresce, F. Wang, C. Yang, Y. S. Hu, K. Xu, and C. Wang, "Water-in-Salt Electrolyte Makes Aqueous Sodium-Ion Battery Safe, Green, and Long-Lasting," *Advanced Energy Materials*, vol. 7, no. 21, p. 1701189, 2017.

[155] R. J. Deeth, "A theoretical rationale for the formation, structure and spin state of pentacyanochromate(II)," *European Journal of Inorganic Chemistry*, vol. 2006, no. 13, pp. 2551–2555, 2006.

[156] Y. Yang, C. Brownell, N. Sadrieh, J. May, A. D. Grosso, D. Place, E. Leutzinger, E. Duffy, R. He, F. Houn, R. Lyon, and P. Faustino, "Quantitative measurement of cyanide released from Prussian Blue," *Clinical Toxicology*, vol. 45, no. 7, pp. 776–781, 2007.

[157] K. J. Nelson, M. C. Daniels, W. M. Reiff, S. A. Troff, and J. S. Miller, "[CrIII(NCMe)6]3+ - A labile Cr III source enabling formation of Cr[M(CN)6] (M = V, Cr, Mn, Fe) Prussian blue-type magnetic materials," *Inorganic Chemistry*, vol. 46, no. 24, pp. 10093–10107, 2007.

[158] W. E. Buschmann, S. C. Paulson, C. M. Wynn, M. A. Girtu, A. J. Epstein, H. S. White, and J. S. Miller, "Reversed (Negative) Magnetization for Electrochemically Deposited High-Tc Thin Films of Chromium Hexacyanide Magnets," *Chemistry of Materials*, vol. 10, no. 5, pp. 1386–1395, 1998.

[159] K. J. Nelson, I. D. Giles, W. W. Shum, A. M. Arif, and J. S. Miller, "The myth of cyanide always being a strong-field ligand: Synthesis and structural characterization of homoleptic S = 2 pentacyanochromate(II), [Cr(II)(CN)5]3-, and nonacyanodichromate(II), [Cr(II)2(CN)9]5-," *Angewandte Chemie - International Edition*, vol. 44, no. 20, pp. 3129–3132, 2005.

[160] J. P. Eaton and D. Nicholls, "The complex cyanides of chromium(II) and chromium(0)," *Transition Metal Chemistry*, vol. 6, no. 4, pp. 203–206, 1981.

[161] F. Hernández-Luis, R. Rodríguez-Raposo, H. R. Galleguillos, and J. W. Morales, "Solubility of Sodium Halides in Aqueous Mixtures with ϵ-Increasing Cosolvents: Formamide, N-Methylformamide, and N-Methylacetamide at 298.15 K," *Industrial and Engineering Chemistry Research*, vol. 55, no. 3, pp. 812–819, 2016.

[162] S. A. Makhlouf, F. T. Parker, F. E. Spada, and A. E. Berkowitz, "Magnetic

anomalies in NiO nanoparticles," *Journal of Applied Physics*, vol. 81, no. 8, pp. 5561–5563, 1997.

[163] M. Bañobre-López, C. Vázquez-Vázquez, J. Rivas, and M. A. López-Quintela, "Magnetic properties of chromium (III) oxide nanoparticles," *Nanotechnology*, vol. 14, no. 2, pp. 318–322, 2003.

[164] A. Eftekhari, "A high-voltage solid-state secondary cell based on chromium hexacyanometallates," *Journal of Power Sources*, vol. 117, no. 1-2, pp. 249–254, 2003.

[165] Y. Moritomo, K. Igarashi, J. Kim, and H. Tanaka, "Size dependent cation channel in nanoporous prussian blue lattice," *Applied Physics Express*, vol. 2, no. 8, p. 085001, 2009.

[166] N. Shimamoto, S. I. Ohkoshi, O. Sato, and K. Hashimoto, "Control of charge-transfer-induced spin transition temperature on cobalt-iron Prussian blue analogues," *Inorganic Chemistry*, vol. 41, no. 4, pp. 678–684, 2002.

[167] J. Burgess, *Metal ions in solution*. Ellis Horwood series in chemical science, Chichester: Ellis Horwood, 1978.

[168] M. Bárcena Soto and F. Scholz, "The thermodynamics of the insertion electrochemistry of solid metal hexacyanometallates," *Journal of Electroanalytical Chemistry*, vol. 521, no. 1-2, pp. 183–189, 2002.

[169] L. Huang, M. Ou, Y. Qiu, C. Fan, Y. Huang, J. Han, X. Sun, Y. Liu, Y. Zhao, Q. Li, J. Wan, J. A. Alonso, C. Fang, P. Wei, Y. Xu, and J. Peng, "Structure Distortion Induced Monoclinic Nickel Hexacyanoferrate as High-Performance Cathode for Na-Ion Batteries," *Advanced Energy Materials*, vol. 9, no. 4, p. 1803158, 2018.

[170] M. Kim, J.-H. Park, J.-M. Lim, H. Kim, and S. Kim, "Conventional and Photoinduced Radioactive 137Cs Removal by Adsorption on FeFe, CoFe, and NiFe Prussian Blue Analogues," *Chemical Engineering Journal*, vol. 405, p. 126568, 2020.

[171] J. Janek and W. G. Zeier, "A solid future for battery development," *Nature Energy*, vol. 1, no. 9, p. 16141, 2016.

[172] M. Pasta, D. Armstrong, Z. L. Brown, J. Bu, M. R. Castell, P. Chen, A. Cocks, S. A. Corr, E. J. Cussen, E. Darnbrough, V. Deshpande, C. Doerrer, M. S. Dyer, H. El-Shinawi, N. Fleck, P. Grant, G. L. Gregory, C. Grovenor, L. J. Hardwick, J. T. S. Irvine, H. J. Lee, G. Li, E. Liberti, I. McClelland, C. Monroe, P. D. Nellist, P. R. Shearing, E. Shoko, W. Song, D. S. Jolly, C. I. Thomas, S. J. Turrell, M. Vestli, C. K. Williams, Y. Zhou, and P. G. Bruce, "2020 roadmap on solid-state batteries," *Journal of Physics: Energy*, vol. 2, no. 3, p. 32008, 2020.

[173] J. Rodríguez-Hernández, E. Reguera, E. Lima, J. Balmaseda, R. Martínez-García, and H. Yee-Madeira, "An atypical coordination in hexacyanometallates: Structure and properties of hexagonal zinc phases," *Journal of Physics and Chemistry of Solids*, vol. 68, no. 9, pp. 1630–1642, 2007.

[174] E. Garnier, P. Gravereau, and A. Hardy, "Zeolitic Iron Cyanides: The Structure of Na2Zn3[Fe(CN)6]2.xH20," *Acta Crystallographica*, vol. B38, pp. 1401–1405, 1982.

[175] J. B. Goodenough, H. Y.-p. Hong, and J. A. Kafalas, "Fast Na+-ion transport in skeleton structures," *Materials Research Bulletin*, vol. 11, no. 2, pp. 203–220, 1976.

[176] H. Y. P. Hong, "Crystal structures and crystal chemistry in the system

Na1+xZr2SixP3-xO12," *Materials Research Bulletin*, vol. 11, no. 2, pp. 173–182, 1976.

[177] M. Avila, J. Rodríguez-Hernández, A. A. Lemus-Santana, and E. Reguera, "Cation mobility and structural changes on the water removal in zeolite-like zinc hexacyanometallates (II)," *Journal of Physics and Chemistry of Solids*, vol. 72, no. 8, pp. 988–993, 2011.

[178] E. Perez-Cappe, M. Aguilar-Frutis, N. Chavez, J. Ribalta, and E. Reguera, "Cation mobility in a series of zeolite-like coordination polymers," *Microporous and Mesoporous Materials*, vol. 163, pp. 326–333, 2012.

[179] J. Jamnik, J. Maier, and S. Pejovnik, "Powerful electrical network model for the impedance of mixed conductors," *Electrochimica Acta*, vol. 44, no. 24, pp. 4139–4145, 1999.

[180] J. Jamnik and J. Maier, "Treatment of the Impedance of Mixed Conductors Equivalent Circuit Model and Explicit Approximate Solutions," *Journal of The Electrochemical Society*, vol. 146, no. 11, pp. 4183–4188, 1999.

[181] J. Jamnik, "Impedance spectroscopy of mixed conductors with semi-blocking boundaries," *Solid State Ionics*, vol. 157, no. 1-4, pp. 19–28, 2003.

[182] J. S. Lee, J. Jamnik, and J. Maier, "Generalized equivalent circuits for mixed conductors: Silver sulfide as a model system," *Monatshefte fur Chemie*, vol. 140, no. 9, pp. 1113–1119, 2009.

[183] R. A. Secco and Y. Huang, "Pressure-induced disorder in hydrated Na-A zeolite," *Journal of Physics and Chemistry of Solids*, vol. 60, no. 7, pp. 999–1002, 1999.

[184] S. Song, H. M. Duong, A. M. Korsunsky, N. Hu, and L. Lu, "A Na+ Superionic

Conductor for Room-Temperature Sodium Batteries," *Scientific Reports*, vol. 6, p. 32330, 2016.